Dissertation

submitted to the

Combined Faculties of the Natural Sciences and Mathematics

of the Ruperto-Carola-University of Heidelberg, Germany

for the degree of

Doctor of Natural Sciences

Put forward by

Dipl.-Phys. Philipp Chung-On Ranitzsch

born in: Karlsruhe

Oral examination: July 22nd 2014

Development and characterization of metallic magnetic calorimeters for the calorimetric measurement of the electron capture spectrum of ^{163}Ho for the purpose of neutrino mass determination

Referees: Prof. Dr. Christian Enss
Prof. Dr. Heinz Horner

The electron capture process of ^{163}Ho offers a unique tool for the determination of the neutrino mass due to its low end-point energy Q_{EC}.

In this work a metallic magnetic calorimeter with an embedded ^{163}Ho source was characterized and used to measure the calorimetric spectrum of the ^{163}Ho decay.

The characterization revealed that neither the thermodynamic properties nor the detector performance were impaired by the presence or the ion-implantation process of the ^{163}Ho source. Furthermore an energy resolution of $\Delta E_{\mathrm{FWHM}} = 7.3\,\mathrm{eV}$ and rise times as low as $\tau_0 = 80\,\mathrm{ns}$ were measured.

The discussed detector achieved the presently best energy resolution for the measurement of the ^{163}Ho electron capture spectrum. For the first time the de-excitation of an electron capture from the ^{163}Ho O_1-level at $E_{O_1} = 48\,\mathrm{eV}$ has been observed. The parameters describing the spectrum could be extracted from the measured spectra. One of the most important parameters, namely the end-point energy has been determined to $Q_{\mathrm{EC}} = (2.877 \pm 0.022\ (\mathrm{stat.})\ ^{+0}_{-0.06}\,(\mathrm{syst.}))\,\mathrm{keV}$.

This implies that the achieved detector performance is suited for a neutrino mass experiment based on ^{163}Ho.

Entwicklung und Charakterisierung von metallisch magnetischen Kalorimetern zur kalorimetrischen Messung des Spektrums des Elektroneneinfangprozesses von ^{163}Ho zum Zweck der Neutrinomassenbestimmung

Der Elektroneneinfangprozess von ^{163}Ho bietet eine einzigartige Möglichkeit zur Bestimmung der Neutrinomasse wegen seiner geringen Endpunktsenergie Q_{EC}.

Im Rahmen dieser Arbeit wurde ein metallisch magnetisches Kalorimeter mit einer eingeschlossenen ^{163}Ho Quelle charakterisiert und benutzt um das kalorimetrische Spektrum des ^{163}Ho Zerfalls zu vermessen.

Die Charakterisierung ergab, dass weder die thermodynamischen Eigenschaften, noch die Detektorleistung von der Präsenz oder dem Ionenimplantationsprozess der ^{163}Ho Quelle negativ beeinflusst wurden. Eine Energieauflösung von $\Delta E = 7.3\,\mathrm{eV}$ und Anstiegszeiten von $\tau_0 = 80\,\mathrm{ns}$ konnten erreicht werden.

Der benutzte Detektor hat die zur Zeit beste Energieauflösung bei der Messung des Eletroneneinfangprozesses von ^{163}Ho gezeigt. Zum ersten Mal wurde die Abregung eines Elektroneneinfangprozesses von der ^{163}Ho O_1-Schale bei einer Energie von $E_{O_1} = 48\,\mathrm{eV}$ beobachtet. Die Parameter zur Beschreibung des Spektrums konnten aus den gemessenen Spektren gewonnen werden. Einer der wichtigsten Parameter, nämlich die Endpunktsenergie wurde mit dem Wert $Q_{\mathrm{EC}} = (2.877 \pm 0.022\ (\mathrm{stat.})\ ^{+0}_{-0.06}\,(\mathrm{syst.}))\,\mathrm{keV}$ gemessen.

Dies ist gleichbedeutend damit, dass die Detektorleistung den Anforderungen eines Neutrinomassenexperiments basierend auf ^{163}Ho entspricht.

Contents

1. Introduction

"Neutrino physics is largely an art of learning
a great deal by observing nothing."

Haim Harari, 1990 [Har90]

This quote can most certainly be applied to other fields of physics research, but in neutrino physics this fact has been established for decades.

Nonetheless has there been a great deal of progress, especially in the last twenty years. With a constant experimental effort is was possible to make the best out of the small signals that neutrinos provide. For example the observation of neutrino oscillations [Fuk98] with the consequence, that neutrinos are in fact massive particles, was a first hint on a wide range of questions that remain to be answered. By now the neutrino oscillations are embedded in an established and well characterized framework [GG12, Pas13], but other areas still observe a lot of "nothing" and need to be satisfied with upper limits.

This includes for example neutrinoless double β-decay experiments, as well as direct neutrino mass searches, which probe fundamental neutrino properties. It in the end comes down to the more exotic idea of sterile neutrinos or the practically unobservable cosmic neutrino background.

In this constant effort to push the boundaries of the experimental possibilities lies the fascination for experimental neutrino physics. It is not only necessary to understand the underlying physics in the best possible way, but also to understand the detectors in all detail. All the intermediate steps between the event itself to the acquired data need to be investigated to extract the real signal and to not be fooled by background or some technical issue, that mimics a signal. To improve the sensitivity of an experimental approach, often scaling to a bigger experiment can be the solution. In contrast, a new experimental approach might just be as successful.

A new experimental approach was for example to use the ^{163}Ho electron capture to probe the neutrino mass [DR81, DR82]. After a few attempts after the initial proposal it took until recently in the mind of the experimentalists to seriously reconsider the idea.

This reconsideration was fueled by the recent progress in the development of cryogenic detectors. With the capability to reach energy resolutions better than $\Delta E_{\mathrm{FWHM}} < 2\,\mathrm{eV}$ in the region of interest below $E < 10\,\mathrm{keV}$, cryogenic detectors offer the perfect tool to measure the ^{163}Ho electron capture.

The focus of this work is the characterization of low temperature metallic magnetic calorimeters for the measurement of the calorimetric electron capture spectrum of ^{163}Ho. This was done as a proof of principe, if it is generally possible to measure the calorimetric spectrum of the ^{163}Ho electron capture with metallic magnetic calorimeters. The achieved results confirm this hypothesis. Further did this work aim to test the influence of an embedded ^{163}Ho source on the performance of metallic magnetic calorimeters and to show, that the achievable detector performance is sufficient for neutrino mass determination. The analysis of the measured spectrum allows to test the parametrization of the ^{163}Ho electron capture spectrum.

In chapter 2 an introduction to the physics related to massive neutrinos is given, with the focus on the different ways of the experimental determination. Especially the bases for the neutrino mass determination utilizing the ^{163}Ho electron capture are described in detail, including the past and current research efforts.

The experimental aspects related to the calorimetric measurement of the ^{163}Ho electron capture spectrum are described in chapter 3. The detectors used for the calorimetric measurements are low temperature metallic magnetic calorimeters. The detection principle as well as the read-out scheme are introduced. In particular a precise description of the design for the used detector prototype as well as for the micro-fabrication steps, with an emphasis to the embedding of the Ho-163 source, will be given.

Chapter 4 contains the experimental results of this work and is divided into two parts. The first part discusses the first characterization of the detector prototype. The investigation of the effect of the embedding of the source was obtained by comparing results of two detectors, one with and one without embedded ^{163}Ho source. This allows to determine the effect of the embedded ^{163}Ho source on the detector characteristics. In the second part two high statistics ^{163}Ho electron capture spectra are analyzed. The achieved detector performance allows the parametrization of the ^{163}Ho electron capture spectrum.

In chapter 5 the international Electron Capture ^{163}Ho experiment (ECHo) is described. Based on the approach of this work the challenges of a large scale ^{163}Ho neutrino mass experiment are discussed as well as possible solutions.

A summary of the presented work is given in chapter 6.

2. Massive Neutrinos

2.1 Neutrinos – The Beginning

The history of neutrinos begins with the often quoted and famous letter of Wolfgang Pauli in 1930 [Pau77], in which he postulates an electrically neutral and very weakly interacting particle in a "desperate resort" to retain energy conservation after a continuous β-spectrum had been measured earlier on "Radium B+C" (^{214}Pb and ^{214}Bi) by James Chadwick in 1914 [Cha14]. At that time the β-decay was imagined as a two-body decay $n \rightarrow p + e^-$ and therefore a distinct energy was expected for the total energy release. Pauli named the newly postulated particle "neutron" and just later on Enrico Fermi gave this particle its final name "neutrino" (little neutron), when he published his "Versuch einer Theorie der β-Strahlen"[1] [Fer34], which provided a theory for the β-decay, including a particle as postulated by Pauli, that still holds today.

It took until 1956 for the definitive direct observation of neutrinos [Cow56]. Clyde L. Cowan and Frederick Reines used the inverse beta decay $\overline{\nu}_e + p \rightarrow n + e^+$ as detection channel for neutrinos created in the fission processes in a nuclear power plant. The idea was to detect the e^+ via e^+e^--annihilation with the measurement of the two 511 keV γ-rays and to detect the neutron via the de-excitation after the n-capture from a suitable nucleus. They ran three liquid scintillator detectors with two target tanks layered in between. The target tanks were filled with Cd loaded water, that allowed the moderated neutron to be captured on ^{113}Cd producing an excited ^{114}Cd atom, that is de-excited by characteristic γ-ray emission.

They used the e^+e^--annihilation signal in coincidence with the delayed by about 10 µs de-excitation γ-ray from the ^{113}Cd(n,γ)^{114}Cd-reaction. The measurement resulted in a cross section of $\sigma = 12^{+7}_{-4} \times 10^{-44}\,\mathrm{cm}^2$ after a refined analysis [Rei60], that agreed well with theoretical expectations from Fermi's theory. At this point the neutrinos were identified as weakly interacting fermions with vanishing mass.

[1] "Attempt at a Theory of β-rays", originally published in German, a translation to English can e.g. be found in [Wil68]

2.2 Neutrino Oscillations

The next important step towards neutrino masses was the "solar neutrino problem" that puzzled neutrino physicists for several decades. In the fusion process

$$4p \longrightarrow {}^4\mathrm{He} + 2e^+ + 2\nu_e \tag{2.1}$$

that is the main energy creation process in the sun also two electron neutrinos are created. Including the annihilation of the two positrons with two electrons a total energy of $E = 26.73\,\mathrm{MeV}$ is produced in one process. Using the total radiative energy arriving at the earth, also known as solar constant, of $S = 8.5 \times 10^{11}\,\mathrm{MeV/cm^2\,s}$, a solar neutrino flux of

$$\Phi_\nu \approx \frac{S}{13\,\mathrm{MeV}} = 6.5 \times 10^{10}\,\mathrm{cm^{-2}s^{-1}} \tag{2.2}$$

can be calculated in this very naive way. Depending on the exact underlying creation process the neutrinos can have energies up to $E_{\max} \approx 20\,\mathrm{MeV}$, even though the major fraction is created in the intermediate *pp*-process[2] with energies lower than $E_\nu \leq 0.42\,\mathrm{MeV}$.

It was the goal of the Homestake experiment, that started in 1968, to detect this large solar neutrino flux and that started the controversy around the "solar neutrino problem". The experiment was performed by Raymond Davis Jr. [Cle98], that used the radiochemical process $\nu_e + {}^{37}\mathrm{Cl} \rightarrow e^- + {}^{37}\mathrm{Ar}$ as proposed by Bruno Pontecorvo [Pon46] and Luis Walter Alvarez [Alv49]. That process offers a rather low threshold energy of 0.814 MeV, a cheap and safe target material in form of Tetrachloroethylene (C_2Cl_4, a common dry-cleaning solvent), and a decaying daughter atom with a half-life of 34.8 d. Davis constructed the target tank to contain 615 t of C_2Cl_4 (containing $\sim 2.2 \times 10^{30}$ ^{37}Cl atoms) and the laboratories for the extraction and measurement of the ^{37}Ar in the Homestake gold mine at Lead, South Dakota, USA. The ^{37}Ar was extracted about every two months and measured in extremely sensitive proportional counters. The experiment ran until 1994 continuously for 26 years with a final neutrino flux of $2.56 \pm 0.16\,(\mathrm{stat.}) \pm 0.16\,(\mathrm{syst.})\,\mathrm{SNU}$[3], while the expectation from solar models was $7.5 \pm 0.1\,\mathrm{SNU}$ [Bah04, TC11].

This deviation was confirmed by several other experiments, such as GALLEX [Ham99], GNO [Alt05], SAGE [Abd09] and Super-Kamiokande [Abe11]. Finally SNO [Aha13] was able to prove that the discrepancy was due to neutrino oscillations in 2001 [Ahm01, Ahm02]. The possibility of neutrino oscillations had

[2] $p + p \longrightarrow {}^2H + e^+ + \nu_e$

[3] SNU = Solar Neutrino Unit = 1×10^{-36} interactions per target atom per second

been suggested by Bruno Pontecorvo [Pon57, Pon58] and their existence had already been verified for atmospheric neutrinos in the Super-Kamiokande detector [Fuk98]

SNO was the first detector that was able to measure all three neutrino flavors with significant sensitivity. The experiment used 10^6 kg of heavy water (^2H_2O) as a target material and utilized the following three detection channels:

1. $\nu_e + d \rightarrow p + p + e^-$: The so-called charged current (CC) reaction, that is only sensitive to electron neutrinos.

2. $\nu_x + e^- \rightarrow \nu_x + e^-$: The elastic scattering (ES) reaction, that is sensitive to all neutrino flavors, but with about 6 times larger cross-section for ν_e compared to ν_μ and ν_τ.

3. $\nu_x + d \rightarrow p + n + \nu_x$: The neutral current (NC) reaction, that is equally sensitive to all neutrino flavors.

By comparing the solar neutrino flux detected in the CC channel with the ES and NC channel a strong 5.3σ evidence was found for a non-electron neutrino component in the solar neutrino flux while the total flux in the NC (flavor independent) channel was consistent with solar models [Ahm02]. This was the first hard evidence, that neutrinos created with electron flavor were detected with a different flavor after they had travelled a certain distance. Since this flavor change was found to be periodic in the traveling distance divided by the neutrino energy L/E (see eq. (2.7)) this effect was called "neutrino oscillations".

The quantum mechanical formalism[4] for neutrino oscillations will be explained in the following, to argue how the existence of finite neutrino masses is necessary to explain the experimental observation of the oscillations. The formalism is based on the idea that n orthogonal weakly interacting eigenstates ν_α (usually $n = 3$; $\alpha = e, \mu, \tau$), or flavor eigenstates of the neutrinos are not identical to the orthogonal set of n mass eigenstates ν_i (usually $i = 1, 2, 3$), but are connected through a unitary $n \times n$ mixing matrix U:

$$|\nu_\alpha\rangle = \sum_i U_{\alpha i} |\nu_i\rangle \ . \tag{2.3}$$

Due to mathematical and physical reasons the number of free parameters of U is limited to $(n-1)^2$, conveniently parametrized into $\frac{1}{2}n(n-1)$ weak mixing angles and $\frac{1}{2}(n-1)(n-2)$ CP-violating phases.

[4]Natural units: $\hbar = c = 1$ are used

The time evolution of the state is given by the Schrödinger equation and results in:

$$|\nu_\alpha(x,t)\rangle = \sum_i U_{\alpha i} e^{\mathrm{i}p_i x} e^{-\mathrm{i}E_i t} |\nu_i\rangle \ , \tag{2.4}$$

assuming a neutrino with energy E_i, momentum p_i, being emitted at $x = 0$.

Using the inverse of eq. (2.3)

$$|\nu_i\rangle = \sum_\beta U^*_{\beta i} |\nu_\beta\rangle \tag{2.5}$$

and assuming relativistic neutrinos

$$E_i = \sqrt{m_i^2 + p_i^2} \simeq p_i + \frac{m_i^2}{2p_i} \simeq E + \frac{m_i^2}{2E} \ , \tag{2.6}$$

for $p_i \gg m_i$ hence $E \approx p_i$ as neutrino energy, and with $L = x = t$ for the distance between source and detector, eq. (2.4) becomes:

$$\begin{aligned} |\nu_\alpha(x,t)\rangle &= \sum_{i,\beta} U_{\alpha i} U^*_{\beta i} e^{\mathrm{i}(p_i x - E_i t)} |\nu_\beta\rangle \\ &= \sum_{i,\beta} U_{\alpha i} U^*_{\beta i} \exp\left(-\mathrm{i}\frac{m_i^2}{2}\frac{L}{E}\right) |\nu_\beta\rangle \ . \end{aligned} \tag{2.7}$$

Therefore the transition probability from the initial state ν_α to the final state ν_β is:

$$\begin{aligned} P(\alpha \to \beta) &= |\langle \nu_\beta | \nu_\alpha(x,t)\rangle|^2 \\ &= \sum_i \sum_j U_{\alpha i} U^*_{\alpha j} U^*_{\beta i} U_{\beta j} \exp\left(-\mathrm{i}\frac{\Delta m_{ij}^2}{2}\frac{L}{E}\right) \ , \end{aligned} \tag{2.8}$$

with the squared mass difference $\Delta m_{ij}^2 = m_i^2 - m_j^2$.

As can be seen in eq. (2.8) the transition probability depends on the source-detector distance L, the neutrino energy E and the mass difference between two mass eigenstates Δm_{ij}^2 and to allow neutrino oscillations $\Delta m_{ij}^2 \neq 0$ needs to be true for at least one mass difference.

The currently preferred number of eigenstates is $n = 3$ that can explain all experimental evidence. Presently the extension to $n > 3$ is considered, because so-called sterile neutrinos, that do not take part in the weak interaction, are proposed to explain experimental phenomena that are tough to explain within the "classical" framework with $n = 3$, as e.g. the "Reactor antineutrino anomaly" [Giu10, Men11].

Experimental status

To find the parameters to describe neutrino oscillations experimentally, a wide range of L/E needs to be covered, which is only achieved with several different experiments. For the detection of solar neutrinos and neutrinos created by meson or muon decay after interaction of primary cosmic rays with the atmosphere, so-called atmospheric neutrinos, already reveal a lot of information. They allow the determination of two mixing angles θ_{12} and θ_{23}, as well as the corresponding mass differences Δm_{12} and Δm_{23}, even though both the energy spectrum and the distance are fixed. A remaining parameter space can be covered with reactor neutrino experiments or with neutrino beams, that are created from the decay of meson beams created at accelerator facilities.

The experiments all detect neutrinos directly and compare the expected rate from the neutrino source with the detected one. Depending on the experiment either the neutrino flavor created at the source is detected with a lowered rate (disappearance mode), a flavor that is not produced in the source is detected (appearance mode) or both modes can be used in combination with discrimination capabilities between detected neutrino flavors. The detectors range from smaller ones like Double Chooz [Abe12] with an active volume of $10\,\mathrm{m}^3$ of Gd-loaded liquid scintillator to larger detectors like the Water-Cherenkov detector Super Kamiokande [Abe11, Wen10] with an active volume of $32\,000\,\mathrm{m}^3$ and incredibly huge Ice-Cherenkov detector IceCube [Aar13] with $1\,\mathrm{km}^3$ of active volume.

Every single experiment can deliver results with different accuracies, but the best conclusions can be drawn by combining the data of all experiments to get a global picture of the neutrino oscillations. The results of such a global fit are quoted in table 2.1 and are taken from [GG12], where also all the contributing experiments are given. An independent second analysis can be found in [Cap14].

Another question that becomes apparent is the ordering of the arbitrarily named mass eigenstates m_1, m_2 and m_3. Only mass differences are known from oscillation results and therefore the question for ordering from lightest to the heaviest eigenstate cannot be answered. In fact from neutrino oscillations in matter it can be determined that $m_2 > m_1$. While traveling through matter neutrinos of all flavors can interact with the surrounding electrons via neutral weak currents and

NuFIT 1.2 (2013)

	Free Fluxes + RSBL		Huber Fluxes, no RSBL	
	bfp $\pm 1\sigma$	3σ range	bfp $\pm 1\sigma$	3σ range
$\sin^2\theta_{12}$	$0.306^{+0.012}_{-0.012}$	$0.271 \to 0.346$	$0.313^{+0.013}_{-0.012}$	$0.277 \to 0.355$
$\theta_{12}/^\circ$	$33.57^{+0.77}_{-0.75}$	$31.37 \to 36.01$	$34.02^{+0.79}_{-0.76}$	$31.78 \to 36.55$
$\sin^2\theta_{23}$	$0.446^{+0.008}_{-0.008} \oplus 0.593^{+0.027}_{-0.043}$	$0.366 \to 0.663$	$0.444^{+0.037}_{-0.031} \oplus 0.592^{+0.028}_{-0.042}$	$0.361 \to 0.665$
$\theta_{23}/^\circ$	$41.9^{+0.5}_{-0.4} \oplus 50.3^{+1.6}_{-2.5}$	$37.2 \to 54.5$	$41.8^{+2.1}_{-1.8} \oplus 50.3^{+1.6}_{-2.5}$	$36.9 \to 54.6$
$\sin^2\theta_{13}$	$0.0231^{+0.0019}_{-0.0019}$	$0.0173 \to 0.0288$	$0.0244^{+0.0019}_{-0.0019}$	$0.0187 \to 0.0303$
$\theta_{13}/^\circ$	$8.73^{+0.35}_{-0.36}$	$7.56 \to 9.77$	$9.00^{+0.35}_{-0.36}$	$7.85 \to 10.02$
$\delta_{\mathrm{CP}}/^\circ$	266^{+55}_{-63}	$0 \to 360$	270^{+77}_{-67}	$0 \to 360$
$\frac{\Delta m^2_{21}}{10^{-5}\ \mathrm{eV}^2}$	$7.45^{+0.19}_{-0.16}$	$6.98 \to 8.05$	$7.50^{+0.18}_{-0.17}$	$7.03 \to 8.08$
$\frac{\Delta m^2_{31}}{10^{-3}\ \mathrm{eV}^2}$ (N)	$+2.417^{+0.014}_{-0.014}$	$+2.247 \to +2.623$	$+2.429^{+0.055}_{-0.054}$	$+2.249 \to +2.639$
$\frac{\Delta m^2_{32}}{10^{-3}\ \mathrm{eV}^2}$ (I)	$-2.411^{+0.062}_{-0.062}$	$-2.602 \to -2.226$	$-2.422^{+0.063}_{-0.061}$	$-2.614 \to -2.235$

Table 2.1 The global fit parameters of a three flavor oscillation analysis [GG12] updated after the "TAUP 2013" conference. The two data sets are created by either leaving the neutrino fluxes from nuclear reactor as a free parameter only using short baseline reactor data ("Free Fluxes + RSBL") or using flux predictions from [Hub11, Hub12] and disregarding short baseline reactor data ('Huber Fluxes, no RSBL").

electron neutrinos can additionally interact via charged weak currents. This singles out electron neutrinos in matter and it can lead to a resonant enhancement of their flavor oscillations for the correct combination of neutrino energy and electron density. These conditions are fulfilled for solar neutrinos and this effect, known as the Mikheyev-Smirnov-Wolfenstein (MSW) effect [Wol78, Mik86], was experimentally proven by the measurement of the composition of solar neutrinos arriving at earth by the SNO experiment [Ahm01, Ahm02].

In principle the MSW effect will also affect neutrinos traveling through earth, which would allow to determine a similar relation for m_3, but up to now the sensitivity of the experiments has not been sufficient. This leaves two possibilities for the ordering, namely the normal hierarchy $m_1 < m_2 \ll m_3$ or the inverted hierarchy $m_3 \ll m_1 < m_2$. The neutrino mass hierarchy is being addressed in the next generation of experiments, currently in the planning phase. A summary of these efforts can for example be found in [Pas13].

This still leaves the question of the absolute scale of neutrino masses, that can not be answered by neutrino oscillations and is addressed in different approaches.

2.3 Neutrino mass determination

The observation of neutrino oscillations demonstrated that neutrinos are massive particles, but nothing can be said about the absolute mass scale of the neutrinos. Different approaches can be used to measure the neutrino mass. These will be discussed in the following including selected experiments following the described approach.

2.3.1 Neutrinoless Double Beta-Decay

Double β-decay is only observable if the single β-decay is energetically forbidden and two neutrons in the nucleus need to decay simultaneously in order to gain energy from the decay. Therefore the observed process is given by:

$$ {}^{A}_{Z}X_N \longrightarrow {}^{A}_{Z+2}X_{N-2} + 2e^- + 2\bar{\nu}_e \ . \tag{2.9} $$

The added energy spectrum of the two emitted electrons is a continuous spectrum up to the end-point energy $Q_{\beta\beta}$ with a maximum at about $Q_{\beta\beta}/3$, similar to single β-decay. Even double β-decay with neutrino emission is one of the rarest observed processes with half-lifes in the range of $t_{1/2} = 10^{18} \ldots 10^{22}$ y.

Based on the theory of Ettore Majorana [Maj37], introducing the idea that neutrinos are their own anti-particles, Wendell H. Furry modified the process [Fur39] so that not two anti-neutrinos are emitted, but that a virtual neutrino is exchanged in the process, leaving the following observable process:

$$ {}^{A}_{Z}X_N \longrightarrow {}^{A}_{Z+2}X_{N-2} + 2e^- \ . \tag{2.10} $$

Adding the observable energy from this process would result in a single line at the end-point energy $Q_{\beta\beta}$.

The observation of the $0\nu\beta\beta$-decay would demonstrate that neutrinos are in fact Majorana fermions, therefore their own anti-particles, and not Dirac particles with distinct anti-particles. Additionally by the measurement of the half-life $T^{0\nu\beta\beta}_{1/2}$, respectively the decay rate $\Gamma^{0\nu\beta\beta}$, of the process it is possible to derive the effective Majorana mass $\langle m_{\beta\beta} \rangle = |\sum_i U^2_{ei} m_i|$. In fact:

$$\begin{aligned}\Gamma^{0\nu\beta\beta} = \left(T_{1/2}^{0\nu\beta\beta}\right)^{-1} &= G^{0\nu\beta\beta}(Q_{\beta\beta}, Z)|M^{0\nu\beta\beta}|^2 \frac{\left|\sum_i U_{ei}^2 m_i\right|}{m_e^2} \\ &= G^{0\nu\beta\beta}(Q_{\beta\beta}, Z)|M^{0\nu\beta\beta}|^2 \frac{\left|\sum_i |U_{ei}|^2 m_i e^{\mathrm{i}\beta_i}\right|}{m_e^2} \\ &=: G^{0\nu\beta\beta}(Q_{\beta\beta}, Z)|M^{0\nu\beta\beta}|^2 \frac{\langle m_{\beta\beta}\rangle}{m_e^2} \quad . \end{aligned} \tag{2.11}$$

Here, m_i are the three neutrino mass eigenstates, $U_{\alpha i}$ the mixing matrix elements (both introduced in chapter 2.2), m_e is the electron mass and β_i the Majorana phases, introduced in the Majorana formalism. $G^{0\nu\beta\beta}(Q_{\beta\beta}, Z)$ is the integral over the phase space of the two electrons, that mainly depends on the end-point energy $Q_{\beta\beta}$, and $M^{0\nu\beta\beta}$ are the nuclear matrix elements (NMEs) that heavily rely on theoretical calculations and currently present the largest uncertainty in the calculation of $\langle m_{\beta\beta}\rangle$. On the other hand the decay rates of different $0\nu\beta\beta$ candidate nuclides can be normalized with their NMEs and phase space factors and therefore allow the results from different measurements to be compared.

Because of the Majorana phases also cancellation in the coherent sum over the mass eigenstates can occur and the mass eigenvalues of the neutrinos are therefore not directly accessible. Nonetheless the determination of $\langle m_{\beta\beta}\rangle$ helps in finding the mass scale and to solve the mass hierarchy in combination with the oscillation results.

There has been one report of an observation of $0\nu\beta\beta$-decay of ^{76}Ge [KK04, KK06] from a subsection of the Heidelberg-Moscow collaboration, that stated a 4.2σ significance with $\langle m_{\beta\beta}\rangle = 440\ (240 \ldots 580)\,\mathrm{meV}$ (3σ range) and $T_{1/2}^{0\nu\beta\beta} = 1.19\ (0.69 \ldots 4.18) \times 10^{25}\,\mathrm{y}$ (3σ range). This result is highly debated and often claimed as being wrong.

Presently there is a lot of interest to demonstrate the existence of the $0\nu\beta\beta$-decay and more than 10 experiments are investigating several $0\nu\beta\beta$ candidates using different experimental techniques (see e.g.[Sch13]). Recent results of three experiments strongly challenge the previously mentioned positive report and will be briefly outlined in the following.

When choosing a nuclide for $0\nu\beta\beta$ search there are basically three factors to be considered: The $Q_{\beta\beta}$-value of the nuclide, interrelated with the achievable background level in the region of interest, the natural abundance of the isotope, interrelated with the enrichment technique and cost, and lastly the compatibility with detection techniques.

^{76}Ge - GERDA

In case of ^{76}Ge the decision for the investigated nuclide is dominated by the well established detection technique. Germanium is regularly used in commercially available and widely used semiconductor detectors, that can be adapted for $0\nu\beta\beta$-search. The $Q_{\beta\beta} = 2039.1\,\text{keV}$ of ^{76}Ge is the lowest of the 11 nuclides for which the $2\nu\beta\beta$-decay has been observed, that have been collected e.g. in [Bar10]. The region of interest is therefore within the natural γ background, that can occur up to $E = 2615\,\text{keV}$, and below the highest energetic β-decay in the ^{222}Rn decay chain, of ^{214}Bi with an end point of $Q_\beta = 3270\,\text{keV}$. The isotopic enrichment of ^{76}Ge can be done in gas centrifuges, similar to the enrichment of ^{235}Ur for nuclear fuel, and is therefore not too expensive[5] and available on an industrial scale.

The GERmanium Detector Array (GERDA), as the successor of the Heidelberg-Moscow Experiment (HDM) and the International Germanium Experiment (IGEX), in its first physics run uses eight reprocessed semicoaxial detectors from the previous experiments as well as five newly developed broad energy germanium (BEGe) detectors both made of high-purity germanium enriched to $\sim 86\,\%$ in ^{76}Ge operated in liquid Ar at 87 K. The first run (11/2011–03/2013) [Ago13] with a total detector mass of 21.3 kg resulted in an exposure of 21.6 kg yr of ^{76}Ge with a background index of $1 \times 10^{-2}\,\text{counts}/(\text{keV kg yr})$. No evidence for $0\nu\beta\beta$ has been observed. Combined with the previous $0\nu\beta\beta$-experiments with ^{76}Ge the run yields a lower limit on the half-life of $T_{1/2}^{0\nu\beta\beta} > 3.0 \times 10^{25}\,\text{yr}$ (90% C.L.). This result strongly disfavors the previously published positive result, but can not exclude it entirely.

Depending on the theoretical input in eq. (2.11) this results in an upper limit for $\langle m_{\beta\beta} \rangle$ of:

$$\langle m_{\beta\beta} \rangle < (200 \ldots 400)\,\text{meV} \ (90\,\%\ \text{C.L.}) \ . \tag{2.12}$$

GERDA phase II is currently being set up, including new detectors, approximately doubling the detector mass, and new active shielding techniques, effectively increasing the expected sensitivity by one order of magnitude.

^{136}Xe - KamLAND-Zen and EXO

Two experiments currently running try to find the $0\nu\beta\beta$ in ^{136}Xe. $Q_{\beta\beta} = 2.458\,\text{keV}$ is slightly higher than in ^{76}Ge but still suffers from the same background sources as ^{76}Ge. The big advantage is that Xe is a gas and therefore chemical processing is not necessary for the isotopic enrichment in centrifuges. This lowers the cost of the

[5] Very rough estimate: $< 100\,€/\text{g}$

enrichment by approximately an order of magnitude. There is no obvious choice for the detection technique and that is where the two experiments go different ways.

KamLAND-Zen uses the modified KamLAND detector, that was originally build for direct anti-neutrino detection in a neutrino oscillation experiment. It uses a 18 m diameter stainless steel vessel instrumented with photomultiplier tubes collecting the light, emitted in a 13 m diameter transparent balloon filled with liquid scintillator, after an event took place. For KamLAND-Zen a second inner balloon with a diameter of about 3 m was added filled with 13 t of Xe-loaded liquid scintillator, the Xe enriched to about 91 % in ^{136}Xe, resulting in a total ^{136}Xe mass of about $m = 287\,\mathrm{kg}$. The latest results [Gan13] use a total of 213 days of data taking between 10/2011 and 06/2012. After necessary cuts, this results in a total exposure of 89.5 kg yr in ^{136}Xe. Although KamLAND-Zen suffered from additional background that was probably introduced during the fabrication of the inner balloon and is possibly connected to the Fukushima Daiichi nuclear disaster, they can provide a strong limit on the $0\nu\beta\beta$ half-life of ^{136}Xe with $T_{1/2}^{0\nu\beta\beta} > 1.9 \times 10^{25}\,\mathrm{yr}$ (90% C.L.).

EXO-200 on the other hand uses a cylindrical time projection chamber (TPC) filled with 110 kg liquified Xe enriched to about 80 % in ^{136}Xe. The scintillation light of the Xe itself is detected by Large Area Avalanche Photodiodes and a drift field of 376 V/cm is applied to the TPC for the created ions to drift and be detected by wire electrodes. This combines good spacial, temporal and energy resolution, strongly enhancing the active background rejection capabilities. The first fully operational run from 09/2011 to 04/2012 with 120 days of data taking resulted in a total exposure of 32.5 kg yr [Aug12]. Very recently a second data set including data from 04/2012 to 01/2013 combined with the previous results has been published [Alb14] increasing the exposure to 99.8 kg yr. With this larger exposure the sensitivity is comparable to the KamLAND-Zen result with $T_{1/2}^{0\nu\beta\beta} > 1.9 \times 10^{25}\,\mathrm{yr}$ (90% C.L.).

But the strength of these two experiments lies in the compatibility of them since they use the same nuclide and no theoretical input is necessary to combine their results. The combination of the full reported KamLAND-Zen data with the reduced EXO data set from the first publication [Aug12] yields $T_{1/2}^{0\nu\beta\beta} > 3.4 \times 10^{25}\,\mathrm{yr}$ (90% C.L.) [Gan13] and once again depending on the nuclear matrix elements in eq. (2.11) leads to:

$$\langle m_{\beta\beta} \rangle < (120 \ldots 250)\,\mathrm{meV}\ (90\,\%\ \mathrm{C.L.})\ . \tag{2.13}$$

This result is the lowest limit on $\langle m_{\beta\beta} \rangle$ to date and it can exclude the previous claim [KK04, KK06] by the subgroup of the Heidelberg-Moscow experiment at 97.5 % C.L., but still suffers from the difficulty in comparing the two results, since theoretical input on the involved nuclei in form of the nuclear matrix elements

(NMEs) is necessary and the uncertainty on the NMEs is the limiting factor in the comparison.

Therefore the best way to exclude the previous claim will in fact be an experiment with the same nuclide as GERDA.

2.3.2 Cosmology

Neutrinos, as fundamental particles in the standard model of particle physics, influence the formation and the development of the universe. This can be seen in several different cosmological effects. Starting with the not yet directly observed, cosmic neutrino background, which consists of the neutrinos created in the big bang and decoupled from other particles only after a few seconds. It is expected to have a temperature of $T = 1.95\,\mathrm{K}$, respectively an average energy of $E \approx 0.17\,\mathrm{meV}$ and a total number density of $336\,\mathrm{cm}^{-3}$ combined for the three flavors and including both neutrinos and anti-neutrinos.

Observable effects include the anisotropy spectrum of the cosmic microwave background (CMB) and the distribution of matter in the universe, the so called large scale structure (LSS).

The influence on the CMB anisotropies originates from the epoch of photon decoupling (at an average energy of $\sim 0.26\,\mathrm{eV}$ or $\sim 400000\,\mathrm{yr}$ after the big bang), when the photon energy is locally influenced by gravitational potentials. While the universe is expanding, the gravitational wells evolve and photons can loose (gain) more energy while leaving the potential, than they gained (lost) by entering it. This effect, known as integrated Sachs-Wolfe (ISW) effect, is the main reason for anisotropies on large angular scales in the range of 10° in the CMB. If neutrinos become non-relativistic in this period, meaning that their absolute mass is on the same scale as the average energy (on the order of $m_\nu \approx 1\,\mathrm{eV}$), neutrinos can also influence the gravitational potentials and smear out large scale fluctuations.

The CMB was accidentally observed by Penzias and Wilson in 1965, who observed an isotropic excess noise in their measurement with a microwave antenna [Pen65]. Their observation was immediately interpreted as "Cosmic Black-Body Radiation" [Dic65]. All precision observations of the CMB anisotropies on large angular scale have been made on spacecrafts. Measurements of the COBE (Cosmic Background Explorer) [Bog92] mission, running from 1989 to 1993 established the anisotropies. The WMAP (Wilkinson Microwave Anisotropy Probe) [Ben03] satellite running from 2001 to 2010 strongly improved the accuracy on the measurement of the CMB anisotropy structure. The most elaborate measurements have been performed by the Planck mission [Tau10], that ran from 2009 to 2013. From Planck data, includ-

ing WMAP polarization data[6], the following limit on the sum of neutrino masses was deduced [Ade13]:

$$\sum m_i \leq 0.933\,\text{eV}\ (95\,\%\ \text{C.L.})\ . \tag{2.14}$$

The large scale structure (LSS) is influenced by two different effects. On the one hand the matter distribution is also affected by the ISW effect during photon decoupling in the transition to a matter dominated universe and on the other hand there is neutrino free streaming. Because of their low mass neutrinos have very large thermal velocity, therefore it is very difficult to trap them in gravitational potential wells up to a characteristic free streaming length l_{fs}. On scales smaller than the free streaming length, $l < l_{\text{fs}}$, the trapped neutrinos can also suppress the formation of anisotropies due to their gravitational influence.

The LSS can be probed in several ways since the matter density can be found from different tracers [Aba11, Won11]. The most powerful tool to date has been galaxy red-shift surveys that provide three dimensional galaxy catalogs. The galaxy number density can be assumed to be directly proportional to the underlying matter density [Ham08], even though non-linearities are assumed in some analyses (e.g. [Ham10]) and will play a more important role in future analyses of more accurate measurements.

Using the available analyses of data from the Sloan Digital Sky Survey (SDSS) [Per10, Pad12], the WiggleZ Dark Energy Survey [Bla11], the Baryon Oscillation Spectroscopic Survey (BOSS) [And12] and the 6-degree Field Galaxy Survey (6dFGS) [Beu11], the Planck collaboration created a combined analysis giving a much stronger limit on the sum of neutrino masses [Ade13]:

$$\sum m_i \leq 0.247\,\text{eV}\ (95\,\%\ \text{C.L.})\ . \tag{2.15}$$

Even though cosmological observations are only sensitive to the sum of neutrino mass eigenstates this is presently one of the most stringent limits. But as well as the results on neutrinoless double beta decay it is based on a quite elaborate model and assumptions made in the analysis. Therefore it is desirable to find a way to compare these results with a different kind of measurement that is not as heavily model based, which can be found in the measurements solely based on neutrino kinematics.

[6]Polarization data is in principle also available from Planck directly, but has not been published up to this point. Publication is planned for October 2014.

2.4 Direct neutrino mass measurements

To find a model independent way to measure the neutrino mass it is necessary to directly access the kinematics of neutrinos. In principle there are two ways of doing so, one being a time-of-flight measurement and the other being weak nuclear decays.

2.4.1 Time-of-flight measurements

The fact that neutrinos are massive particles lead to the expectation, that the time-of-flight of neutrinos over the distance d will differ from d/c, the time-of-flight of a photon. Since the neutrino masses are very small, also the observable difference will be extremely small. Therefore a combination of a long baseline, a very strong source and suitable detectors is necessary.

The long baseline directly implies to go to astronomical scales and in core-collapse supernovae very intense neutrino sources can be found. The general interest in supernovae for astronomy led to the formation of the "Supernova Early Warning System" (SNEWS) [Ant04] collaboration, that combines and synchronizes several neutrino detectors to provide an accurate signal of supernova neutrinos. Since the light signal is expected hours up to days after the neutrino signal this will help to prepare the telescopes for the light signal of the supernova. Additionally the neutrino signal can be used for a time-of-flight analysis.

The only successful time-of-flight analyses have been done on data from neutrinos observed after the supernova SN1987A in the Large Magellanic Cloud and it resulted in an upper limit of $m_\nu < 5.7\,\mathrm{eV}$ (95 % C.L.) [Lor02]. Long baseline experiments with neutrino beams produced at accelerators, like MINOS and OPERA [Acq09] also offer the possibility for a time-of-flight measurement. But the sensitivity is orders of magnitude worse than for SN1987A because of the much shorter baseline. While the result for a deviation from the speed of light c is $(v/c-1) = (1.0 \pm 1.1) \times 10^{-6}$ for MINOS [Ada12b] and $(v/c-1) = \left(2.7 \pm 3.1\,(\mathrm{stat.})^{+3.4}_{-3.3}\,(\mathrm{sys.})\right) \times 10^{-6}$ for OPERA [Ada12a] a simple analysis for SN1987A results in the much lower limit of $|v/c-1| \leq 2 \times 10^{-9}$ [Lon87].

With today's experimental possibilities neutrinos from close-by supernovae seem the only way to make use of time-of-flight measurements in neutrino mass determination. Apart from the rarity of these events, the underlying supernova models are not precise enough to allow a sensitivity comparable to cosmological limits or direct neutrino mass measurements on weak nuclear decays [Raf10].

2.4.2 Neutrino mass and weak decays

The second way to investigate neutrino masses using kinematics can be found in weak nuclear decays. Both single β-decay and electron capture (EC) are used for neutrino mass determination. The sensitivity of these measurements scales with the observed number of counts N in the energy interval ΔE, typically on the order of $\Delta E \approx 10\,\mathrm{eV}$, just below the end-point energy Q, that follows the proportionality $N \propto (\Delta E/Q)^3$ in the case of β-decay. That already implies that a low end-point energy Q and an intense source, resulting in a large statistics in the end-point region, will be advantageous to achieve a good sensitivity.

Most of the investigations have been done on single β-decay:

$$ {}^{A}_{Z}X_N \longrightarrow {}^{A}_{Z+1}X_{N-1} + e^- + \bar{\nu}_e \ , \tag{2.16} $$

where a neutron in the nucleus decays to a proton by emitting an electron e and an electron-anti-neutrino $\bar{\nu}_e$. Because of its much larger mass the nucleus takes close to none of the energy from the decay and the energy is divided between the electron and the anti-neutrino. By measuring the electron energy it is possible to deduce informations on the emitted neutrino, including its mass.

The other weak decay that can be used for neutrino mass determination is the electron capture:

$$ \begin{aligned} {}^{A}_{Z}X_N &\longrightarrow {}^{A}_{Z-1}X^*_{N+1} + \nu_e \\ &\hookrightarrow {}^{A}_{Z-1}X_{N+1} + E_{\mathrm{EC}} \ , \end{aligned} \tag{2.17} $$

where an electron from the atomic shell is captured by a proton in the nucleus and a neutron is formed. In this process an electron neutrino is emitted and the atom is left in an excited state, with a hole in the shell the original electron was captured from. The total energy is mainly divided between the neutrino and the excited state. By measuring the de-excitation spectrum of the excited atom also information on the neutrino can be deduced, including its mass.

2.4.3 β-decay

In β-decay, according to Fermi's Golden rule the shape of the emitted β-electron spectrum is given by[7]:

[7] A thorough derivation can e.g. be found in [Dre13].

$$\frac{\mathrm{d}N^2}{\mathrm{d}t\,\mathrm{d}E_e} = \frac{G_\mathrm{F}^2\cos^2\Theta_\mathrm{C}}{2\pi^3\hbar^7}|M_\mathrm{had}^2|\,F(E_e,Z+1)\,p_e\,(E_e+m_ec^2) \times(Q_\beta-E_e)\sum_i|U_{ei}|^2\sqrt{(Q_\beta-E_e)^2-m_{\nu_i}^2c^4}\ , \tag{2.18}$$

with G_F being the Fermi coupling constant, Θ_C the Cabibbo angle accounting for the decay on quark level and $|M_\mathrm{had}^2|$ being the nuclear matrix element. Q_β is the total energy available in the decay, equivalent to the mass difference between mother and daughter atom. E_e, p_e and m_e are the energy, the momentum and the mass of the electron, respectively. m_{ν_i} is the ith neutrino mass eigenstates corresponding to the elements of the neutrino mixing matrix U_{ei}, while

$$F(E_e,Z+1)=\frac{2\pi\eta}{1-\exp(-2\pi\eta)} \tag{2.19}$$

is the Fermi function, accounting for the Coulomb interaction between emitted electron and the remaining daughter nucleus, with the Sommerfeld parameter $\eta = \alpha(Z+1)/\beta$ with the fine structure constant α and the relativistic velocity $\beta = v_e/c$.

In case of $(Q_\beta - E_e) \gg m_{\nu_i}c^2$ the following approximation is valid:

$$\begin{aligned}&(Q_\beta-E_e)\sum_i|U_{ei}^2|\sqrt{(Q_\beta-E_e)^2-m_{\nu_i}^2c^4}\\ &\quad\approx(Q_\beta-E_e)^2-m^2(\bar{\nu}_e)c^4\ ,\end{aligned} \tag{2.20}$$

by using the unitarity of the neutrino mixing matrix ($\sum_i|U_{ei}^2|=1$) and by defining the averaged electron anti-neutrino mass as the incoherent mixing of the three mass eigenstates $m^2(\bar{\nu}_e) := \sum_i|U_{ei}^2|\,m_{\nu_i}^2$. Treating the incoherent sum as a single averaged one is very reasonable since the experimental resolution of last and also next generation neutrino mass searches will very likely not be good enough to resolve the tiny differences between the single mass eigenstates. If the term "electron neutrino mass" or similar terms are used in the following, this incoherent sum of the mass eigenstates is meant.

The effect of a non-zero neutrino mass is strongest at high energies in the spectrum, if $(Q_\beta - E_e)^2 \approx m^2(\bar{\nu}_e)c^4$, while at lower energies a constant offset is created. Therefore all experimental efforts aim to resolve this last part of the spectrum, typically between 10 eV and 100 eV below the end-point Q_β, their region of interest, with highest accuracy.

The choice of the β-decaying nuclide also has a huge impact on the experiment. The half-life $T_{1/2}$ of the nuclide determines the necessary amount of source material, which is also closely connected to the decay mode. Depending on the angular momentum and the parity of the mother and daughter nucleus the transition can range from "super-allowed" to "third order forbidden", which has a large impact on the half-life and can distort the otherwise simple spectral shape given in eq. (2.18).

Another major impact is created by the end-point energy Q_β of the decay. If only Q_β is changed in the decay (following equation (2.18)) the relative number of events in the region of interest scales with $\propto Q_\beta^{-3}$. Additionally the preference for low Q_β is promoted by experimental considerations. Firstly, the detector needs to be able to handle absolute count rate, which increases with larger Q_β, or will run into problems with unresolved pile-up. Secondly, for most detector-techniques the achievable energy resolution scales with the absolute energy scale and a low end-point Q_β is also desirable to ensure the best results.

Mainly two nuclides have been investigated, namely ^{3}H and ^{187}Re. The first investigations with ^{3}H date back to the late forties of the last century [Cur49] and ^{3}H has been under investigation since then by employing different styles of electric or magnetic spectrometers. The last and current generation of experiments are based on electrostatic spectrometers named MAC-E-filter.

The experimental investigations with ^{187}Re only date back to the nineties of the last century and have been heavily pushed with the development of cryogenic calorimeters, that are operated at very low temperatures $T < 1\,\mathrm{K}$ and measure the heat input following the impact of an energetic particle.

^{3}H – KATRIN

Most of neutrino mass searches have been performed on tritium. The tritium β-decay

$$^3\mathrm{H} \longrightarrow {}^3\mathrm{He} + e^- + \bar{\nu}_e \tag{2.21}$$

is a super-allowed transition, which means that the spectral shape will basically be as given in equation (2.18) with an energy independent nuclear matrix element of [Rob88]:

$$|M^2_{\mathrm{had}}(^3\mathrm{H})| = 5.55\hbar^6 \ , \tag{2.22}$$

a short half-life of only $T_{1/2} = 12.3\,\mathrm{y}$ and a low end-point at $Q_\beta = 18.6\,\mathrm{keV}$. Tritium is available in the desired amounts, e.g. from heavy water moderated fission reactors

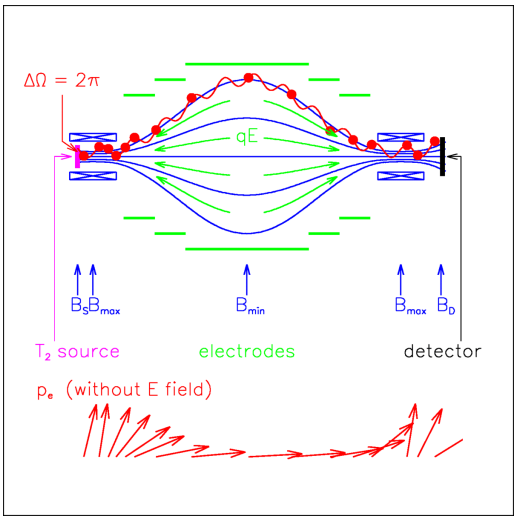

Figure 2.1 Schematic of a MAC-E-Filter spectrometer [Kru83, Pic92]:
Top: Experimental setup.
Bottom: Electron momentum across the spectrometer.
Depiction provided by Karlsruhe Institute of Technology URL `http://www.katrin.kit.edu`

like CANDU-type reactors or through breeding in nuclear reactors through the reaction $^6\mathrm{Li}(n,\alpha)^3\mathrm{H}$ [Whi96, Fie92], and will likely be easily available in future due to the demand in fusion research and development. Techniques for handling the radioactive substance have also been in development for decades due to interest in applications such as self-powered lighting, fusion reactors and nuclear weapons [Fie92].

The latest results on neutrino masses from the β-decay of ^{3}H have been achieved with the "Magnetic Adiabatic Collimation with an Electrostatic Filter" (MAC-E-Filter) technique. Based on the electron spectrometer developed by Kruit and Read [Kru83], the technique was adapted for the larger energies necessary for neutrino mass search [Pic92]. The schematic of a MAC-E-filter spectrometer is shown in figure 2.1. It is based on two solenoids, one on the source and one on the detector side creating a continuous B-field in the spectrometer with its maximum value B_{max} in the solenoids, while in between the magnetic field is weakened by several orders of magnitude to B_{min}. The electrons emitted from the source are guided along the magnetic field lines and their momentum p_e is adiabatically turned and aligned with the magnetic field lines. Additionally the electrons are exposed to an electric potential created by a set of electrodes surrounding the spectrometer. If the kinetic energy E is smaller than the charge q multiplied with the retarding potential U:

$$E \leq q\,U \quad , \tag{2.23}$$

the electron will be reflected in the spectrometer and extracted, while in case $E \geq q\,U$ the electron is transmitted and detected. Therefore the spectrometer effectively acts as an energy high-pass filter with an energy resolution given by the extremes of the

magnetic field:

$$\frac{\Delta E}{E} = \frac{B_{\min}}{B_{\max}} \ . \tag{2.24}$$

With this experimental configuration an integral spectrum is measured and to get an energy dependence of the spectrum the retarding potential U is varied and the transmitted electrons are counted.

Two concluded experiments, named after their locations, the Mainz and the Troisk experiment have successfully used this technique for neutrino mass determination and found similar upper limits on the electron anti-neutrino mass. The major difference between the experiments was in the tritium source setup. The Troisk experiment used molecular tritium $^3H_2$ in its gaseous form in a "windowless gaseous tritium source" and found an upper limit of $m(\bar{\nu}_e) \leq 2.05\,\text{eV}$ (95 % C.L.) [Ase11]. The Mainz experiment used a thin film of molecular tritium on a cold graphite substrate as source and with this setup was able to reach an upper limit of $m(\bar{\nu}_e) \leq 2.3\,\text{eV}$ (95 % C.L.) as a final result [Kra05]. Combining these two results gives [Ber12]:

$$m(\bar{\nu}_e) \leq 2.0\,\text{eV} \ (95\,\%\ \text{C.L.}) \ . \tag{2.25}$$

For the next generation search the Mainz and the Troisk collaborations joined forces and formed an international collaboration, the "KArlsruhe TRItium Neutrino experiment" (KATRIN). KATRIN currently is finishing the setup and the commissioning of the experiment at the Karlsruhe Institute of Technology (KIT) and is planned to start taking data in 2016 presumably for a three year period. The main spectrometer is a 9.8 m diameter, 23.3 m long vessel for the MAC-E-filter. This is connected to an about 50 m long source and transport section, which includes the pre-spectrometer also based on the MAC-E-filter technique. KATRIN is capable to discover a non-zero neutrino mass down to $m(\bar{\nu}_e) = 0.35\,\text{eV}$ (5σ) and will be able to set a new upper limit one order of magnitude lower than previous experiments at [Ang05]:

$$m(\bar{\nu}_e) \leq 0.2\,\text{eV} \ (90\,\%\ \text{C.L.}) \ . \tag{2.26}$$

On the set timescale and with this sensitivity KATRIN will likely be unrivaled. Another larger experiment with a significant improvement in sensitivity based same principles is not to be expected, simply because of the necessary size of the spectrometer and the associated cost. But other improvements on the current setup, for example by employing a method for a differential measurement of the spectrum, either by using a time-of-flight method or a differential detector can still significantly improve the sensitivity.

But there are other projects based on different experimental techniques in development that aim for a similar sensitivity as KATRIN and do not have such a fundamental problem with their scalability, which will be outlined in the following.

^{3}H – Project 8

The recently proposed "Project 8" [Mon09] wants to make use of the cyclotron motion of electrons in an external magnetic field B. The cyclotron frequency is given by:

$$\omega = \frac{\omega_0}{\gamma} = \frac{qB}{m_e c^2 + E} \ , \tag{2.27}$$

where ω_0 is the unshifted cyclotron frequency, γ is the Lorentz factor and with the electron's charge q, mass m_e and kinetic energy E. While executing the motion also cyclotron radiation will be emitted at the same frequency ω. This radiation can be detected with suitable detectors surrounding the source.

Project 8 aims to have a vacuum vessel filled with $10^{-7} - 10^{-6}$ mbar of $^3H_2$ gas in a homogeneous magnetic field of 1 T in a magnetic bottle setup, trapping the electrons and allowing much longer observation times. The source is then surrounded with microwave antenna to detect the cyclotron radiation. For β-electrons around the tritium end-point with energies of $E \approx 18.6$keV the cyclotron frequency is in the range of $f_0 = \omega_0/2\pi \approx 27\,\mathrm{GHz}$.

The cyclotron frequency of all emitted β-electrons is monitored simultaneously, which allows to measure the differential spectrum of the ^{3}H β-decay. By analyzing the end-point region around $Q_\beta \approx 18.6$keV the effect and the magnitude of the electron neutrino mass $m(\nu_e)$ can be deduced.

A prototype has been set up at the University of Washington incorporating all key components of a large scale experiment. This includes a gaseous electron source, the magnetic bottle setup and the microwave detection and read-out scheme. First preliminary tests of the system without electron source have been successful [For13] and will be followed up with tests using a ^{83m}Kr electron source, that emits monoenergetic electrons at $E = 17.8\,\mathrm{keV}$ and $E = 32\,\mathrm{keV}$.

^{187}Re – MARE

The β-decay of ^{3}H has not the lowest Q_β-value, since two other isotopes show a lower Q_β, namely ^{115}In and ^{187}Re. ^{115}In is quite difficult to realize in an experiment for various reasons. The decay in question is from ^{115}In to the excited nuclear $(3/2^+)$-state of ^{115}Sn and shows an end-point energy of $Q_\beta = (155 \pm 24)\,\mathrm{eV}$ [Mou09].

The very low Q_β is advantageous, but the decay to the excited state only shows a branching ratio of BR $= (1.07 \pm 0.17) \times 10^{-6}$ [Wie09] to the β-decay to the ground state of ^{115}Sn and has an ultra-long half-life of the partial decay of $T_{1/2} = (4.1 \pm 0.6) \times 10^{20}$ y [Wie09]. In principle the β-electrons from the decay to the excited state can be identified by the coincident de-excitation γ-ray of the ^{115}Sn nucleus, but the experimental precision to identify and accurately measure the energy of the one electron in about one million electrons from the decay to the ground state in combination with the required statistics is currently hard to imagine.

The other candidate with a very low end-point is

$$^{187}\mathrm{Re} \longrightarrow {}^{187}\mathrm{Os} + e^- + \bar{\nu}_e \tag{2.28}$$

with an end-point energy of $Q_\beta = 2.47\,\mathrm{keV}$ and a half-life of $T_{1/2} = 4.3 \times 10^{10}\,\mathrm{y}$, which corresponds to an activity of approximately $A = 1\,\mathrm{Bq}$ per $m = 1\,\mathrm{mg}$ of source mass. The spin-parity configuration ($J^\pi(^{187}\mathrm{Re}) = 5/2^+ \rightarrow J^\pi(^{187}\mathrm{Os}) = 1/2^-$) of the decay causes the transition to be first unique forbidden, which leads to a more complex spectral shape as the one described by eq. (2.18), which has been calculated in [Dvo11] and causes the long half-life.

Due to the long half-life and the required statistics [Nuc10], large amounts of the material are necessary for an experiment based on ^{187}Re. This is compensated by the fact that naturally occurring Re is 62.8 % ^{187}Re and therefore it is sufficient to use $^{\mathrm{nat}}$Re. Because of the low Q_β it is impossible to extract the β-electrons out of a solid ^{187}Re source, while keeping the energy information of the electron. Therefore a detection technique that incorporates the source into the detector, in a so-called calorimetric measurement, is necessary and can be found in cryogenic micro-calorimeters.

These detectors use a thermal sensor to detect the rise in temperature after the absorption of an energetic particle and a crystal containing suitable amounts of ^{187}Re can be attached to the sensor to measure the ^{187}Re β-spectrum. In contrast to an external spectrometer, where the measured electrons can be analyzed and discarded before they are detected, the detector in a calorimetric measurement needs to be able to resolve all decays individually. Therefore not a single large detector, which incorporates the whole source mass, but a large number of small detectors with their individual small sources are used.

The use of ^{187}Re read-out by thermal micro-calorimeters has been proposes in the early 1980s [McC84, Bla85] and has been investigated by two independent experiments, MANU and MIBETA.

The MANU experiment investigated metallic Re absorbers, read-out with Neu-

tron Transmutation Doped (NTD) Ge thermistors, and has found to an upper limit of $m(\bar{\nu}_e) \leq 26\,\mathrm{eV}$ (95 % C.L.) [Gat01].

Within the framework of the MIBETA experiment, measurements with $AgReO_4$ crystals coupled to Si thermistors on the other hand have led to a lower limit of [Sis04]

$$m(\bar{\nu}_e) \leq 15\,\mathrm{eV}\ (90\,\%\ \mathrm{C.L.})\ , \tag{2.29}$$

which is the lowest limit from direct neutrino mass measurements not obtained with ^{3}H. This result was obtained with 8 detectors with an average energy resolution of $\Delta E_{\mathrm{FWHM}} = 28.5\,\mathrm{eV}$ at the end-point $E_0 = 2.47\,\mathrm{keV}$. The total Re mass was 2.174 mg, corresponding to a total ^{187}Re activity of 1.17 Bq, which was measured for a period of 210 d.

These encouraging results have led to a combined effort of the former two experiments and the formation of the "Micro-calorimeter Arrays for a Rhenium Experiment" (MARE) collaboration [Nuc08]. Within MARE the use of large arrays of micro-calorimeters is planned, operated at mK temperatures and each equipped with a ^{187}Re source with an individual activity of $\sim 1\,\mathrm{Bq}$, containing $\sim 1\,\mathrm{mg}$ of $^{\mathrm{nat}}$Re.

Several detection techniques have been under investigation to reach the desired detector performance of an energy resolution of $\Delta E_{\mathrm{FWHM}} \approx 1\,\mathrm{eV}$ combined with a rise time of $\tau_0 \approx 1\,\mu\mathrm{s}$ [Nuc08]. This includes semiconductor thermistors [McC05a] transition-edge sensors [Irw05] and metallic magnetic calorimeters [Fle05], either coupled to dielectric $AgReO_4$ crystals or superconducting metallic Re crystals.

Further improvements with metallic rhenium over the MANU results with any detection technique have been hindered by the difficult and lengthy thermalization of energy in superconducting materials [Cos93, Wel08, Ran09, Hen12], that prohibited detectors with metallic Re absorbers to reach the desired performance [Por11, Fer12, Ran12].

The efforts surrounding $AgReO_4$ crystals are ongoing and the recent commissioning of one 6×6 Si:P thermistor array equipped with $AgReO_4$ crystals has been reported, with a second identical array being setup in the near future [Fer14]. With the larger detector number the statistics can be drastically improved and a lower limit of $m(\bar{\nu}_e) \leq 4.5\,\mathrm{eV}$ (90 % C.L.) can be reached in a 3 y period [Fer14].

The investigations of the ^{187}Re β-decay are ongoing, but presently the detector performance and the array size are not suitable to reach a sub-eV sensitivity on the neutrino mass in the near future.

2.4.4 Electron capture

After the electron is captured by the nucleus (see eq. (2.17)), an electron neutrino is emitted and the atom is left in an excited state. The de-excitation can happen through radiative or non-radiative transitions. In the radiative transition, the hole in the atomic shell, at the energy $E_\circ$ compared to the continuum, is filled by an outer shell electron at energy E_1 and the transition energy $E_\gamma = E_\circ - E_1$ is emitted in form of an X-ray.

In case of the non-radiative transition, when the hole is filled by an electron of energy E_1, the available energy is used to emit a weaker bound electron, at the energy $E_2 < E_1$, with a kinetic energy of $E_e = E_\circ - E_1 - E_2$. This non-radiative transition is generally called "Auger effect", but in the particular case, when the hole and the filling electron belong the same electronic shell it is renamed to "Coster-Kronig transition". If all three electrons are from the same shell it is called a "Super Coster-Kronig transition".

Each electron capture is followed up by a cascade of transitions, until the daughter atom is at its ground state, whose summed up energy corresponds to the de-excitation energy E_{EC}. Due to the multitude of de-excitation channels, electron capture spectra can be measured in different ways. In the case the source is external from the detector, both X-rays spectroscopy, as well as Auger electron spectroscopy are possible and information on the neutrino's influence on the spectrum can be extracted.

The drawback of this method is that it will only be possible to measure a part of E_{EC} with an external detector and the branching ratios into the different decay channels need to be very well known. Additionally the source must be very well characterized and ideally set up in a way that self-absorption within the source is avoided.

A method to overcome the need to correct the measured spectrum for effects leading to changes in the shape is to include the source in the detector. This way it is possible to measure the whole E_{EC} in a calorimetric measurement as already described for the ^{187}Re β-decay in chapter 2.4.3. This approach was first described in [DR82] in case of the ^{163}Ho electron capture, where the authors provide the differential decay rate

$$\begin{aligned}\frac{\mathrm{d}\Gamma}{\mathrm{d}E_{\mathrm{EC}}} &= \mathcal{C}\,(Q_{\mathrm{EC}} - E_{\mathrm{EC}})\sqrt{(Q_{\mathrm{EC}} - E_{\mathrm{EC}})^2 - m^2(\nu_e)} \\ &\quad \times \sum_{\mathrm{H}} \varphi^2_{\mathrm{H}}(0) B_{\mathrm{H}} \frac{\Gamma_{\mathrm{H}}}{2\pi} \frac{1}{(E_{\mathrm{EC}} - E_{\mathrm{H}})^2 + \Gamma^2_{\mathrm{H}}/4}\ . \end{aligned} \tag{2.30}$$

Here, the constant $\mathcal{C}$ represents the squares of the nuclear matrix element and the Fermi coupling followed by the phase space term with the end-point energy Q_{EC}, the decay energy E_{EC} and the average electron neutrino mass $m(\nu_e)$. The electronic levels H of the decaying atom are characterized by their relative amplitudes given by the electron's wave function at the origin $\varphi^2_{\mathrm{H}}(0)$, the exchange and overlap corrections B_{H}, and their Lorentzian line shape, described by the line's central energy position E_{H} and its width Γ_{H}.

The impact of the neutrino mass on the spectrum is once again largest close to the end-point Q_{EC} and for similar reasoning as for β-decay (see chapter 2.4.3) a low Q_{EC}-value is desired for a successful experiment.

The discrete nature of the electron shells enhances the decay rate largely close to the central energies E_{H}, and in case $Q_{\mathrm{EC}} \approx E_{\mathrm{H}}$ this enhancement will cause a large number of counts in the region of interest below the Q_{EC}-value. Presently no nuclide, where $Q_{\mathrm{EC}} \approx E_{\mathrm{H}}$ is fulfilled has been found.

The best candidate for neutrino mass determination by means of electron capture spectroscopy remains the already mentioned ^{163}Ho with its very low end-point of $Q_{\mathrm{EC}} = (2.555 \pm 0.016)\,\mathrm{keV}$ [Wan12].

^{163}Ho

The decay scheme of ^{163}Ho can be written as:

$$\begin{aligned} {}^{163}_{67}\mathrm{Ho}_{96} &\longrightarrow {}^{163}_{66}\mathrm{Dy}^{*}_{97} + \nu_e \\ &\hookrightarrow {}^{163}_{66}\mathrm{Dy}_{97} + E_{\mathrm{EC}} \ , \end{aligned} \tag{2.31}$$

with a half-life of 4570 y [Bai83] and the nuclear spin changing in the allowed transition from $^{163}\mathrm{Ho}(7/2)^-$ to $^{163}\mathrm{Dy}(5/2)^-$. The recommended value is $Q_{\mathrm{EC}} = (2.555 \pm 0.016)\,\mathrm{keV}$ [Wan12], but values as low as $Q_{\mathrm{EC}} = (2.3 \pm 1.0)\,\mathrm{keV}$ [And82] and as high as $Q_{\mathrm{EC}} = (2.80 \pm 0.05)\,\mathrm{keV}$ [Gat97] have been reported.

Due to the low Q_{EC}-value only electrons from the M_1-level (the $^3\mathrm{S}_{1/2}$-level in spectroscopic notation) or lower can be captured[8]. Due to angular momentum selection rules electrons with total angular momentum $j \geq 3/2$ are also forbidden to be captured, which leads to the list of levels shown in table 2.2.

Figure 2.2 shows the expected spectral shape after eq. (2.30) with a zoom on the region around Q_{EC}, where the expected effect due to a finite neutrino mass

[8]The X-ray notation (K, M, L, etc.) for atomic levels will be used in the following and throughout this thesis.

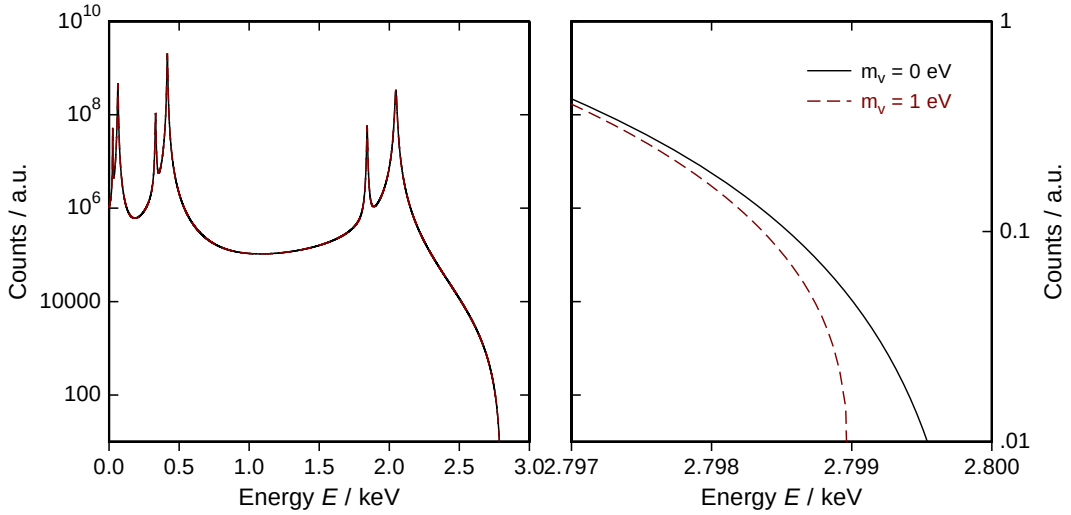

Figure 2.2 Calculated electron capture spectrum from ^{163}Ho after equation (2.30), with the line properties given in table 2.2 and assuming an end-point of $Q_{\mathrm{EC}} = 2.8\,\mathrm{keV}$. In the right figure the difference between a vanishing and an assumed neutrino mass of $m(\nu_e) = 1\,\mathrm{eV}$ is shown close to Q_{EC}.

of $m(\nu_e) = 1\,\mathrm{eV}$ is shown. While the description in eq. (2.30) is very straight forward, there are several known effects e.g. described in [DR13] that can distort the spectral shape below the end-point. These effects might be very small and therefore negligible. On the other hand it is very important to investigate and characterize them to quantify the systematic uncertainties.

No ^{163}Ho is found in nature and it needs to be artificially produced. There are several ways of doing so in accelerator and research reactor facilities. And not only the production but also the purification needs to be addressed, to avoid radioactive contaminants, that can create background. This is a major concern within the research efforts around ^{163}Ho. The approach of the ECHo collaboration on this topic is described in chapter 5.1.

Over the course of the last 30 years there have been several measurements of the ^{163}Ho electron capture spectrum, both calorimetric and non-calorimetric, which will be summarized in the following in chronological order.

Calorimetric measurement with ion-implanted Si detector The first calorimetric measurement of the ^{163}Ho electron capture spectrum was reported in 1984 [Lae84], only two years after the technique was proposed. A sample of enriched ^{162}Er was neutron irradiated to form ^{163}Ho via the process $^{162}\mathrm{Er}(n,\gamma)^{163}\mathrm{Er}(EC,\beta^+)^{163}\mathrm{Ho}$, followed up by a chemical purification of repeated ion-exchange chromatography steps. The source material was then isotope-separated

Spectral line H	$\frac{\varphi^2_{\mathrm{H}}(0)}{\varphi^2_{\mathrm{M1}}(0)}$	B_{H}	E_{H} [eV]	Γ_{H} [eV]
M_1	1	1.083	2046.9	13.2
M_2	0.0526	1.031	1844.6	6.0
N_1	0.233	1.151	420.4	5.4
N_2	0.0119	1.108	340.6	5.3
O_1	0.0345	1.248	49.9	3.7 [Coh72]
O_2	0.0115	1.224	26.3 [Tho09]	
P_1	0.0021			

Table 2.2 ^{163}Dy spectral lines present in the electron capture spectrum of ^{163}Ho and their general properties. The energy E_{H} [Des03] and the width Γ_{H} [Cam01]. The electron's wave function at the origin $\varphi^2_{\mathrm{H}}(0)$ [Ban86], the given values are normalized to the amplitude of the M_1-line, and the exchange and overlap corrections B_{H} [Muk87].

and ion-implanted into intrinsic Si crystals at different configurations. The crystals were than n and p doped and electrically contacted to enable the read-out.

These detectors are usually operated at liquid nitrogen temperature $T = 77\,\mathrm{K}$ and a bias voltage is applied between n- and p-contacts. The absorption of electrons or X-rays creates electron-hole pairs, and their amount is proportional to the incident energy. The created charge is separated by the bias voltage and detected as a current signal at the p-type contact.

There were problems with the detector, firstly it showed an energy resolution of $\Delta E_{\mathrm{FWHM}} \approx 380\,\mathrm{eV}$ for the $M_{1,2}$ line around $E = 2\,\mathrm{keV}$ compared to an intrinsic resolution of $\Delta E_{\mathrm{FWHM}} = 75\,\mathrm{eV}$, that was determined in calibration data from a ^{137}Cs X-ray source and a precision pulser. The lower intrinsic resolution was roughly reproduced in the $N_{1,2}$ line around $E = 420\,\mathrm{eV}$. Secondly the detector showed signs of incomplete charge collection, causing the central peaks of the measured lines to be at lower energies compared to their literature values, which was most likely caused by defects created by the ion implantation. And lastly the detector's performance was only stable for about one day before it started deteriorating and a reproducible "regeneration procedure" by several minutes of forward bias at liquid nitrogen temperatures needed to be applied to restore the performance. Nonetheless the ^{163}Ho electron capture spectrum was successfully measured, reproduced in figure 2.3 (bottom) from a 15 h measurement with an ^{163}Ho electron capture activity of $A \approx 0.03\,\mathrm{Bq}$. From the relative N to M capture rates the end-point of the electron capture was determined to be $Q_{\mathrm{EC}} = (2.82^{+0.08}_{-0.06})\,\mathrm{keV}$.

IBEC spectrum with Si(Li) detector P.T. Springer et al. [Spr87] measured only the radiative transition spectrum, also called IBEC (for internal bremsstrahlung

electron capture) spectrum, as first suggested for neutrino mass determination by A. De Rújula [DR81]. They used a $30\,\mathrm{mm}^2$ Si(Li) detector with an energy resolution of $\Delta E_{\mathrm{FWHM}} = 137\,\mathrm{eV}$ at the region of interest around 2 keV. The source consisted of $(89.7 \pm 9)\,\mu\mathrm{g}$ corresponding to $(3.3 \pm 0.3) \times 10^{17}$ atoms or a total electron capture activity of $A \approx 1\mathrm{MBq}$ of ^{163}Ho, that were produced and purified in a similar fashion as for the measurements in [Lae84] summarized in the previous paragraphs. The source was chemically prepared to the form of $^{163}HoF_3$ and vacuum-evaporated on a stainless steel substrate positioned in front of the detector.

In the analysis the detection efficiency, the detector response and the background level were determined and the interference from lower energetic X-rays were subtracted and only the contributions from M_1O_2- and M_1N_2-transition X-rays to the spectrum were fitted for the effect of the neutrino mass. An upper limit on the electron neutrino mass of

$$m(\nu_e) \leq 225\,\mathrm{eV}\ (95\,\%\ \mathrm{C.L.}) \tag{2.32}$$

was found, which is also the strongest limit on $m(\nu_e)$ to date. In the analysis the end-point was limited to $Q_{\mathrm{EC}} \leq 2.64\,\mathrm{keV}$, based on an upper limit on the Q_{EC} from an independent determination of N to M capture rates reported in [Har85].

Calorimetric measurement with proportional counter Hartmann et al. [Har92] developed a gas proportional counter detector that can be operated at elevated temperatures around 200 °C and can be loaded with gaseous compounds containing the investigated nuclide. For the ^{163}Ho measurement a β-diketonate, namely Ho_3(fod) (fluoro-octanedione), was chosen and prepared from the source material already used for the previous measurements by Springer et al. [Spr87]. The Ho_3(fod) is a stable, easily soluble and volatile compound that reaches partial pressures of a few mbar at elevated temperatures between 150 ... 200 °C and therefore meets the requirements for the use in a gas proportional counter.

After thoroughly considering systematic effects, calibrating the detector and measuring the background, the Ho spectrum was successfully measured and is reproduced in figure 2.3 (middle). Using the binding energies reported in [Spr87] and the their measured relative N to M capture rates the end-point of the spectrum is determined to be $Q_{\mathrm{EC}} = (2.561 \pm 0.02)\,\mathrm{keV}$.

Partial decay rates with Si(Li) detector The fourth approach discussed here once again takes a different route towards the neutrino mass. The idea is based on measuring several different partial decay rates of the ^{163}Ho electron capture and for each determined decay rate a different parameter entering the theoretical decay

description can be constrained as first discussed in [Ben81]. Yasumi et al. [Yas94] chose to measure the partial decay rates λ_{M_i} $(i = 1, 2)$ of the radiative transitions from the M_1 and M_2 levels as well as the total decay rate λ_t.

The total decay rate can be determined from the half-life, that was redetermined to be $T_{1/2} = (4569 \pm 27)\,\mathrm{y}$ (68 % C.L.) [Kaw88] confirming the previous result of $T_{1/2} = (4570 \pm 50)\,\mathrm{y}$ (95 % C.L.) [Bai83] giving a total decay rate of $\lambda_\mathrm{t} = (4.807 \pm 0.028) \times 10^{-12}\,\mathrm{s}^{-1}$.

To experimentally determine the partial radiative decay rates from the M_1- and M_2-levels several steps were necessary. First the total radiative electron capture spectrum was measured in a setup similar to the one of Springer et al. described earlier. The second step was to measure the X-ray fluorescence from the single levels to later determine their relative contributions to the total spectrum. This was achieved by creating holes in the daughter atom ^{163}Dy specifically in the M_1- and M_2-shells separately with monochromatic X-rays from a synchrotron light source and measuring the resulting radiative de-excitation. These two separate partial X-ray spectra were scaled in order to reproduce the total X-ray spectrum measured earlier. From the relative amplitudes of the partial spectra the partial decay rates $\lambda_{M_1} = (0.9846 \pm 0.0492) \times 10^{-12}\,\mathrm{s}^{-1}$ and $\lambda_{M_2} = (0.0850 \pm 0.0026) \times 10^{-12}\,\mathrm{s}^{-1}$ were found.

Using these three partial decay rates and the atomic parameters from [Muk87], the end-point energy, the electron neutrino mass and the comparative half-life or $\log(ft)$-value are determined to:

$$\begin{aligned} Q_\mathrm{EC} &= \left(2.710^{+0.100}_{-0.005}\right)\,\mathrm{keV} \\ m(\nu_e) &= \left(110^{+350}_{-110}\right)\,\mathrm{eV} \\ \log(ft) &= 4.993^{+0.030}_{-0.001}\ , \end{aligned}$$

which gives an upper limit for the electron neutrino mass of:

$$m(\nu_e) \leq 460\,\mathrm{eV}\ (68\,\%\ \mathrm{C.L.})\ . \tag{2.33}$$

Calorimetric measurement with NTD Ge detector Gatti et al. [Gat97] used a ^{163}Ho source in liquid solution that was dried onto the surface of a $300\,\mu\mathrm{m} \times 800\,\mu\mathrm{m} \times 50\,\mu\mathrm{m}$ tin foil, was bonded with epoxy and subsequently folded to enclose the source material in the tin absorber. This geometry allowed a calorimetric measurement with negligible energy losses. This absorber was attached to a $100 \times 200 \times 200\,\mu\mathrm{m}^3$ NTD Ge thermistor, that is used to measure the temperature

rise in the tin absorber following an electron capture event at the cryogenic operating temperature of $T = 50 \ldots 60\,\mathrm{mK}$.

The use of cryogenic micro-calorimeters for the calorimetric measurement showed a much better accuracy, being for the first time able to resolve the sub-shells M_1, M_2 and N_1, N_2 from one another as shown in the reproduced spectrum in figure 2.3 (top). The achieved intrinsic energy resolution of $\Delta E_{\mathrm{FWHM}} = 40\,\mathrm{eV}$ was found in calibration data from an ^{55}Fe X-ray source and an Al X-ray fluorescence line. The resolution achieved in the ^{163}Ho electron capture spectrum was deteriorated compared to the intrinsic one, namely to $\Delta E_{\mathrm{FWHM}} = 50\,\mathrm{eV}$ and $\Delta E_{\mathrm{FWHM}} = 100\,\mathrm{eV}$ for the N- and the M-lines, respectively. The observed line energies were about 8 % smaller than the literature values, if compared to calibration data. This was attributed to the composite absorber and metastable states created in the amorphous salt and epoxy mixture during the thermalization of the energy emitted in the electron capture. The energy scale was nonetheless found to be linearly dependent on the literature values, showing the self-calibrating properties of electron capture spectra.

Despite the low statistics with approximately 4000 events in the whole spectrum, allowing no analysis of the neutrino mass, the end-point was determined to be $Q_{\mathrm{EC}} = (2.800 \pm 0.050)\,\mathrm{keV}$.

Current research As can be seen from this collection of experiments from the eighties and nineties of the last century, there was a lot of interest in the ^{163}Ho electron capture as a means of neutrino mass determination. These for the most part very thought out attempts show the huge potential behind the approach, unfortunately the used detector techniques and performances were mostly not sufficient to be able to compete against ^{3}H experiments, not even including the source material availability. This led to a strong decrease in interest and close to no progress on the ^{163}Ho electron capture in the first decade of the 21st century.

The development and the improvement of cryogenic detectors in the last decade, leading to energy resolutions on the order of $\Delta E_{\mathrm{FWHM}} = 1.5 \ldots 3\,\mathrm{eV}$ at $E = 6\,\mathrm{keV}$, has started the interest up again and led to the formation of two major collaborations, the "Electron Capture ^{163}Ho experiment" (ECHo) and "The Electron Capture Decay of ^{163}Ho to Measure the Electron Neutrino Mass with sub-eV sensitivity" (HOLMES), and some independent research towards the investigation of the neutrino mass using the electron capture of ^{163}Ho. Most of these efforts are collected in [Nuc13] and will be outlined in the following.

The ECHo experiment [Gas14] aims to determine the electron neutrino mass with sub-eV sensitivity by means of a high resolution, high statistics measurement of the ^{163}Ho electron capture spectrum. The detectors for the main task will be

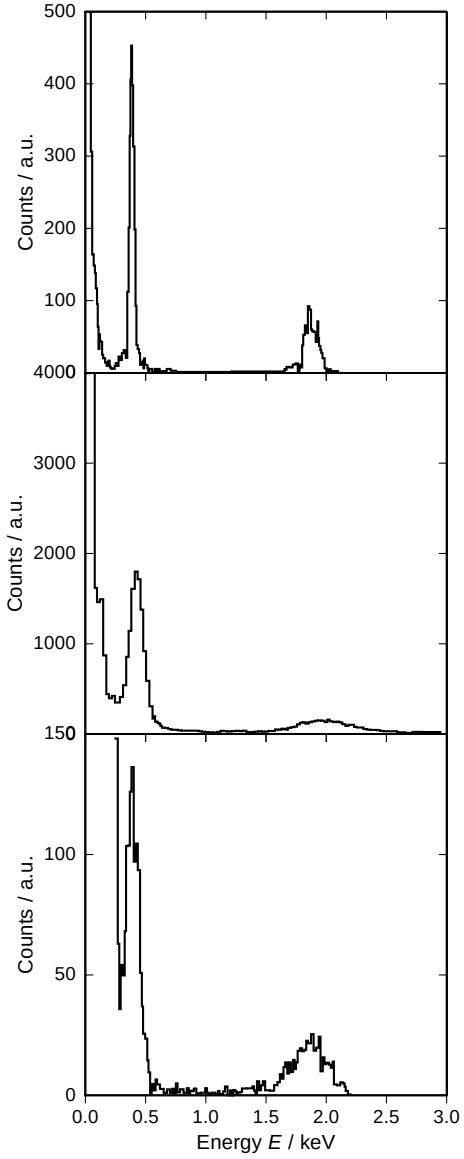

Figure 2.3 Previous calorimetric measurements of the ^{163}Ho electron capture spectrum.
Top: Spectrum taken with a cryogenic NTD Ge detector [Gat97], the ^{163}Ho in organic salt form layered in between a two layered Sn absorber bonded with epoxy.
Middle: Spectrum taken with a proportional counter [Har92], the ^{163}Ho in form of gaseous Ho_3(fod) added to the counter gas.
Bottom: Spectrum taken with a Si(Li) detector [Lae84] ion-implanted with ^{163}Ho.

large arrays of cryogenic metallic magnetic calorimeters [Fle05]. The development and customization of the detectors will be accompanied by detailed background studies, investigations concerning the production and purification of ^{163}Ho and a precise theoretical and experimental parametrization of the ^{163}Ho electron capture spectrum, including an independent measurement of the end-point energy Q_{EC}. A detailed description of the approach of this collaboration will be summarized in detail in a separate chapter 5.

The HOLMES project started in February 2014 with the goal of achieving a statistical sensitivity on the electron neutrino mass of order of $m(\nu_e) \leq 1\,\mathrm{eV}$ (90 % C.L.) within a 5 year period by investigating the ^{163}Ho electron capture decay. Within the project also the feasibility of a larger scale experiment with an ultimate sensitivity

of $m(\nu_e) \leq 0.1\,\mathrm{eV}$ (90 % C.L.) will be determined. The structure of the experiment is based on preparatory work within the MARE collaboration on the feasibility and statistical sensitivity of a medium to large scale ^{163}Ho electron capture experiment [Gal12] and the ^{163}Ho production and preliminary measurements [Gom13].

The central idea is to set up a 1000 pixel array of transition edge sensors (TES) with an energy resolution of $\Delta E_{\mathrm{FWHM}} = 1\,\mathrm{eV}$ and a rise time of $\tau = 1\,\mu\mathrm{s}$. The detectors will be equipped with Au absorbers, that are implanted with approximately 6.5×10^{13} ^{163}Ho atoms each, giving an activity of 300 Bq per pixel. Within a measurement period of 3 years a total of 3×10^{13} events will be acquired in the whole spectrum allowing the quoted statistical sensitivity.

The areas of research include the nuclide production and purification, detector optimization, read-out and data processing as well as cryogenics. The detector work can be divided into the single pixel optimization for best performance and for the ^{163}Ho embedding and into array development, production and testing. The read-out and data processing concerns the low-temperature SQUID read-out and the room temperature electronics as well as the digitization, online signal processing algorithms, data storage and final physics analysis software. The cryogenics part is concerned with the setup, the testing and the operation of the dilution refrigerator for the final measurement campaign.

The HOLMES collaboration clearly is the largest effort towards ^{163}Ho electron capture spectroscopy outside of the ECHo collaboration, but the interest from other institutions has noticeably increased in the last few years. A group from LANL[9] investigated the production of ^{163}Ho by proton, neutron and α-particle irradiation [Eng13], being especially concerned about the isotopic purity of the produced source. In a collaboration between groups from LANL and from NIST[10], TES detectors for total Q-spectroscopy are being developed, with possible applications being isotopic analysis of radioactive materials at MeV energies and neutrino mass determination at keV energies [Cro13]. Another interesting aspect under investigation e.g. at NIST is the single event analysis at very high count rates [Fow13] in the $100 \ldots 1000\,\mathrm{Bq}$ range, that is of concern for most cryogenic detector applications, but especially for neutrino mass determinations with strong requirements on statistics.

Statistical sensitivity of ^{163}Ho electron capture experiments

The statistical sensitivity for the electron neutrino mass depends strongly on the detector performance. At a given detector performance, the number of events in the

[9] Los Alamos National Laboratory, Los Alamos, NM, USA
[10] National Institute for Standards and Technology, Boulder, CO, USA

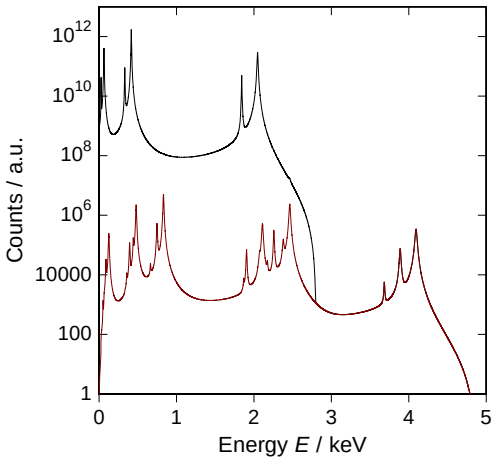

Figure 2.4 The unresolved pile-up spectrum (red) and the sum of normal and pile-up spectrum (black) are shown. An end-point energy of $Q_{\mathrm{EC}} = 2.8\,\mathrm{keV}$ and a pile-up fraction of $f_{\mathrm{pp}} = 10^{-5}$ are assumed.

full spectrum needed to reach sub-eV sensitivity is then scaling with the fraction of counts in the last few eV below the end-point Q_{EC}. Unfortunately very diverging values for the Q_{EC} have been reported and the larger Q_{EC}, the more counts in the total spectrum are needed.

Another effect that needs to be considered for the determination of the sensitivity is the intrinsic background, namely the unresolved pile-up spectrum. This is created if two events happen in one detector in a time interval Δt that is smaller than the finite time resolution of the detector. In this case the two events, with energies E_1 and E_2, are evaluated by the detector as a single event with an energy $E \approx E_1 + E_2$. The relative contribution of the pile-up spectrum is given by the activity of the single detector A multiplied with the minimum time difference, for which two events can be distinguished from one another. This time interval can be identified with the rise time of the detector signal τ_0. Based on that the pile-up fraction:

$$f_{\mathrm{pp}} := A\,\tau_0 \tag{2.34}$$

can be defined. The pile-up spectrum is described by the convolution of the main spectrum with itself. Figure 2.4 shows the pile-up spectrum together with the sum of pile-up and main spectrum of the ^{163}Ho electron capture, assuming an end-point of $Q_{\mathrm{EC}} = 2.8\,\mathrm{keV}$ and a pile-up fraction of $f_{\mathrm{pp}} = 10^{-5}$. With these parameters the fraction of events in the last 10 eV below the end-point is nearly equal with 6×10^{-10} of the events in the main spectrum and 5×10^{-10} of the events in the pile-up spectrum.

Fortunately the influence of the pile-up spectrum can be estimated from knowing the single detector activity A and the detector rise time τ_0. Secondly an independent way is provided by the pile-up spectrum itself. By measuring and fitting the pile-up spectrum above the end-point, especially the peaks in the pile-up spectrum around

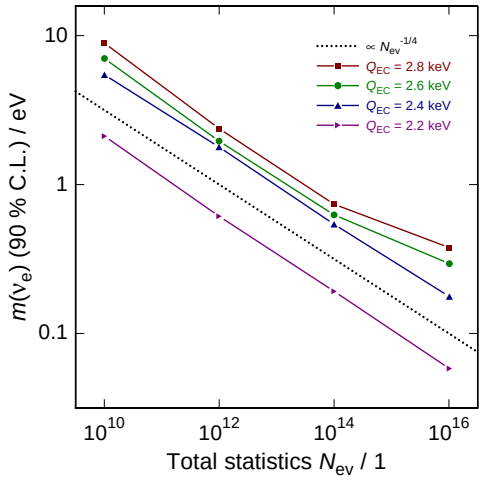

Figure 2.5 The statistical sensitivity of a ^{163}Ho neutrino mass experiment with detectors with an energy resolution $\Delta E_{\mathrm{FWHM}} = 1\,\mathrm{eV}$ and a pile-up fraction of $f_{\mathrm{pp}} = 10^{-5}$ for various end-point energies Q_{EC}. The statistical sensitivity roughly scales with $N_{\mathrm{ev}}^{-1/4}$. Data reproduced from [Nuc14].

$E \approx 4\,\mathrm{keV}$, also the influence around the Q_{EC} value can be estimated.

Apart from the intrinsic background also the external background needs to be considered. This can be created from radioactive contaminants in the detector materials, especially in the embedded source. Secondly also sources outside of the detector can cause background, either from contaminants in surrounding materials or induced by cosmic rays. As long as the external background level is much lower than the intrinsic pile-up spectrum this will have no immediate effect. In case the two background source have comparable levels in the end-point region, the background will also degrade the statistical sensitivity.

In [Gal12] and [Nuc14] a set of dedicated Monte-Carlo simulations is conducted to assess the statistical sensitivity on the electron neutrino mass with ^{163}Ho. Their results will be outlined in the following. The presented simulations are assumed to be free of background.

The overall sensitivity roughly scales with $N_{\mathrm{ev}}^{-1/4}$ in the shown range. Apart from the difference between $Q_{\mathrm{EC}} = 2.2\,\mathrm{keV}$ and $Q_{\mathrm{EC}} = 2.4\,\mathrm{keV}$, the statistical sensitivity is quite similar for the end-point energies $Q_{\mathrm{EC}} \geq 2.4\,\mathrm{keV}$. Nonetheless the necessary number of events to reach the same statistical sensitivity is always at least a factor of 2 larger for $Q_{\mathrm{EC}} \geq 2.8\,\mathrm{keV}$ compared to $Q_{\mathrm{EC}} \geq 2.6\,\mathrm{keV}$.

It can be concluded that in order to reach a statistical sensitivity of $m(\nu_e) < 10\,\mathrm{eV}$ (90 % C.L.) a maximum of $N_{\mathrm{ev}} = 10^{10}$ events are necessary and to reach $m(\nu_e) < 1\,\mathrm{eV}$ (90 % C.L.) a maximum of $N_{\mathrm{ev}} = 10^{14}$ will be needed.

For a next generation neutrino mass experiment based on ^{163}Ho the aim is to reach a statistical sensitivity of at least $m(\nu_e) < 1\,\mathrm{eV}$ (90 % C.L.). Therefore the impact of the parameters influencing the statistical sensitivity will be analyzed for a total statistics of $N_{\mathrm{ev}} = 10^{14}$.

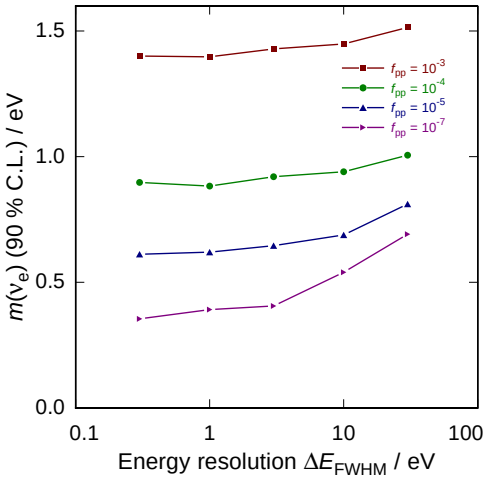

Figure 2.6 The impact of the energy resolution ΔE_{FWHM} on the statistical sensitivity on the neutrino mass $m(\nu_e)$ is shown for different pile-up fractions f_{pp}. An end-point energy $Q_{\mathrm{EC}} = 2.6\,\mathrm{keV}$ and a total statistics of $N_{\mathrm{ev}} = 10^{14}$ are assumed. Data reproduced from [Nuc14].

The influence of both the energy resolution ΔE_{FWHM} and the pile-up fraction f_{pp} is shown in figure 2.6 for a fixed value of $Q_{\mathrm{EC}} = 2.6\,\mathrm{keV}$. The following conclusions can be drawn, which can be applied for all Q_{EC}-values: The impact of the energy resolution is small for $\Delta E_{\mathrm{FWHM}} < 10\,\mathrm{eV}$ and the pile-up fraction f_{pp} should be as low as possible. The total acquisition time will make a tradeoff on the pile-up fraction necessary.

Considering a reasonable acquisition time of $T = 3\,\mathrm{y} \approx 10^8\,\mathrm{s}$ and a total of 10000 detectors, an activity per detector of $A = 100\,\mathrm{Bq}$ is necessary to reach $N_{\mathrm{ev}} = 10^{14}$. With a rise time of $\tau_0 = 100\,\mathrm{ns}$ a pile-up fraction of $f_{\mathrm{pp}} = 10^{-5}$ is reached and with an energy resolution of $\Delta E_{\mathrm{FWHM}} \leq 10\,\mathrm{eV}$, a statistical sensitivity of approximately $m(\nu_e) < 0.7\,\mathrm{eV}$ (90 % C.L.) can be achieved.

Assuming an end-point of $Q_{\mathrm{EC}} = 2.8\,\mathrm{keV}$ for this hypothetical experiment the number of counts in the intrinsic pile-up spectrum in the last $\Delta E = 10\,\mathrm{eV}$ below the end-point is $N_{\mathrm{ev,pp}} \approx 50\,000$. To reach the same number of background events in a flat, energy independent background spectrum a background of $b \approx 0.5\,\mathrm{counts/keV/day/detector}$ needs to be reached. For example in the MIBETA experiment (see chapter 2.4.3) a constant background of $b \approx 0.15\,\mathrm{counts/keV/day/detector}$ below $E < 20\,\mathrm{keV}$ has been observed [Sis04]. While the MIBETA background can not directly be applied to a ^{163}Ho experiment, because of the different detector geometries and the different sources, it shows that the required background level is actually achievable.

3. Experimental preparation and implementation

3.1 Cryogenic detectors for ^{163}Ho electron capture spectrometry

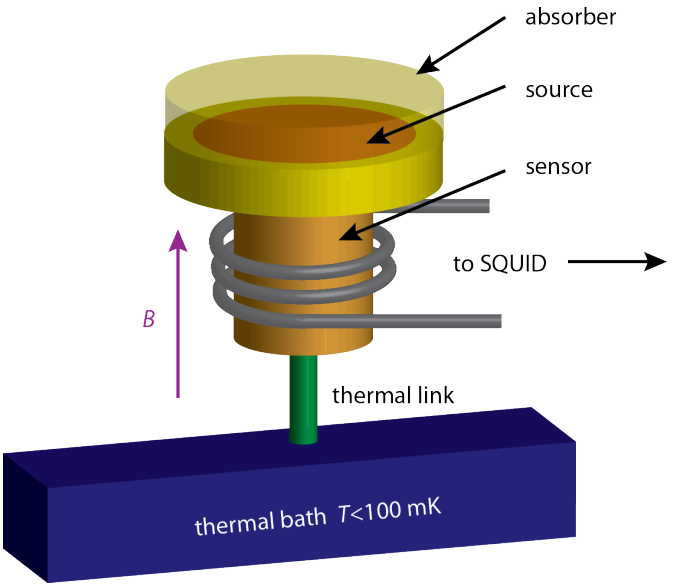

Figure 3.1 The schematic of a metallic magnetic calorimeter for calorimetric measurements. It shows the absorber with the embedded radioactive source, closely connected to the Au:Er sensor, which in turn is weakly connected to the thermal bath. The sensor is positioned in a weak magnetic field B and is surrounded by a superconducting loop connected to the read-out SQUID.

One of the first major challenges in a ^{163}Ho neutrino mass experiment is actually to measure the decay energy below $E < 3\,\mathrm{keV}$ with a resolution of $\Delta E_{\mathrm{FWHM}} < 10\,\mathrm{eV}$. This is simply not possible with classical semiconductor detectors, which show resolutions on the order of $\Delta E_{\mathrm{FWHM}} \approx 100\,\mathrm{eV}$. Thermal detectors operated at mK temperatures have on the other hand shown their capability to fulfill the requirements of a ^{163}Ho experiment.

These cryogenic detectors are based on the calorimetric principle, which means that they measure a rise in temperature ΔT proportional to the deposited energy ΔE:

$$\Delta T \approx \frac{\Delta E}{C_{\mathrm{tot}}} \ , \tag{3.1}$$

with the total heat capacity C_{tot} of the detector. After the initial temperature rise the detector slowly relaxes back to the temperature of the thermal bath, with a

relaxation time τ_1 defined by the weak thermal link G:

$$\tau_1 \approx \frac{C_{\mathrm{tot}}}{G} \quad . \tag{3.2}$$

Several different extremely sensitive "thermometers" have been under development to read-out the rise in temperature. The most established ones are semiconductor thermistors [McC05a], superconducting transition-edge sensors (TES) [Irw05] and metallic magnetic calorimeters [Fle05]. All of these detector types have shown energy resolutions $\Delta E_{\mathrm{FWHM}} < 10\,\mathrm{eV}$ for energies below $E < 10\,\mathrm{keV}$ and are suited for the application in a ^{163}Ho neutrino mass experiment.

The second task is to make sure that the measurement of the ^{163}Ho electron capture is calorimetric. This means that all released energy –independent of release channel– is measured in the detector. This can be achieved, if the decaying material is embedded into the detector and surrounded by enough absorber material that the absorption efficiency is as close to 100 % as reasonably possible. To reach an absorption efficiency of at least $P = 0.999$ for all decay channels at least seven times the attenuation length λ of the least stopped de-excitation should be used. For gold absorbers, which are commonly used with cryogenic detectors, the least stopped radiation for energies below $E < 3\,\mathrm{keV}$ are photons with energies just below the M_5-edge of gold with an energy of $E_{M_5} = 2205.7\,\mathrm{eV}$ [Hub04]. These photons show an attenuation length of $\lambda = 0.56\,\mu\mathrm{m}$.

A particle absorber suitable for this task will therefore consist e.g. of a planar first absorber layer made of approximately $h = 5\,\mu\mathrm{m}$ of gold on which the source material is deposited on a slightly reduced area. The absorber is then finished by a second absorber layer of the same dimensions as the first one and the source material is therefore surrounded by absorber material in all dimensions forming a so-called 4π geometry.

This work is based on metallic magnetic calorimeters (MMCs), which will be described in more detail in the following. A schematic of a metallic magnetic calorimeter for a calorimetric measurement is shown in figure 3.1. The thermometer used to read-out the rise in temperature is a paramagnetic alloy made of gold and a few hundred ppm of the rare earth erbium, positioned in a weak magnetic field of order $B \sim \mathrm{mT}$, which polarizes the spins in the sensor material. Operated at temperatures below $T < 100\,\mathrm{mK}$, Au:Er shows a very strong change of magnetization with temperature $\partial M/\partial T$, which is in turn read-out by a closed superconducting pick-up loop in close contact to the sensor material. The change of magnetization causes a change of flux in the superconducting loop and the resulting eddy currents are read-out by a Superconducting Quantum Interference Device (SQUID), that is inductively coupled to the pick-up loop. The resulting flux signal $\Delta\Phi_{\mathrm{S}}$ in the SQUID

is still proportional to the incident energy:

$$\Delta\Phi_{\mathrm{S}} \propto \frac{\partial M}{\partial T}\Delta T \approx \frac{\partial M}{\partial T}\frac{\Delta E}{C_{\mathrm{tot}}} \quad . \tag{3.3}$$

MMCs can be reliably and reproducibly fabricated by micro-fabrication techniques and have successfully shown energy resolutions as low as $\Delta E_{\mathrm{FWHM}} = 1.6\,\mathrm{eV}$ [Kra13] and rise times as low as $\tau_0 = 90\,\mathrm{ns}$ [Fle09] in their main application field of soft X-ray spectroscopy. Similar performance can be expected for calorimetric electron capture spectroscopy.

The detector design used for the measurements presented within this work is described in chapter 3.4. More general information on metallic magnetic calorimeters can be found e.g. in [Fle05, Fle09]. The detailed understanding of the sensor material Au:Er has been heavily pushed forward in [Sch00, Fle03a, Fle05] and is summarized in the appendix A.

3.2 Read-out geometry

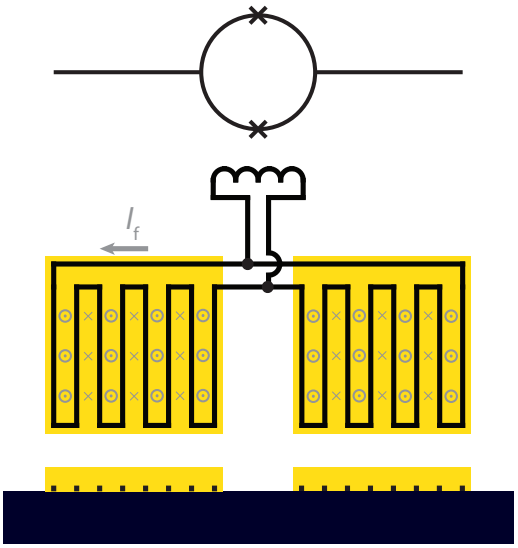

Figure 3.2 Schematic of the read-out geometry with meander shaped pick-up coils. The magnetic field as generated by the field generating current I_{f} is indicated.

The magnetization of the Au:Er sensor is detected as a change of flux in a suitable superconducting pick-up coil. Several approaches to measure the magnetization of the Au:Er sensor are discussed in [Fle05, Fle09]. The current working horse for micro-fabricated MMCs are meander-shaped pick-up coils as shown in figure 3.2.

The two pick-up coils are connected in parallel with opposite winding, forming a first order gradiometer, that is insensitive to changes in external magnetic fields. The input coil to the read-out SQUID is connected in parallel to the two meanders

as shown in figure 3.2. The Au:Er sensor material is deposited on top of the meander structures with a height of about one third of the pitch p of the meander structure, which was found to be the optimal height in numerical optimizations [Fle05, Fle09].

Au:Er can be deposited on one or both of the meanders. If only one meander is covered the detector is sensitive to absolute temperature changes and the magnetization of the sensor material can be measured to characterize the detector. By covering both meanders the magnetization signal of one sensor compensates the signal of the second sensor for a common temperature change. This makes the operation generally more stable and doubles the detection area at the cost of slightly increased noise, since the noise of both sensors couples incoherently into the common read-out SQUID.

3.2.1 Field generating persistent current

The meander structure can not only be used to pick-up the change in magnetization, but also to generate the magnetic field, that polarizes the sensor material. This is carried out by running a persistent current I_f of several mA through the coils as indicated in figure 3.2.

The setup for the preparation of the field current I_f is shown in figure 3.3. For this task an additional path is added to the meander, that is in close contact to a resistive heater, which acts as persistent current switch. The procedure is the following: first the field generating current I_f is injected into the field current leads as shown in figure 3.3 (a). Due to Kirchhoff's circuit laws for superconducting circuits the current is divided according to the inductances of the possible paths, therefore most of the current passes through the short path to the heater. In the next step, shown in figure 3.3 (b), a current is also injected into the heater. The power dissipated by the current in the resistance is enough to drive its close environment

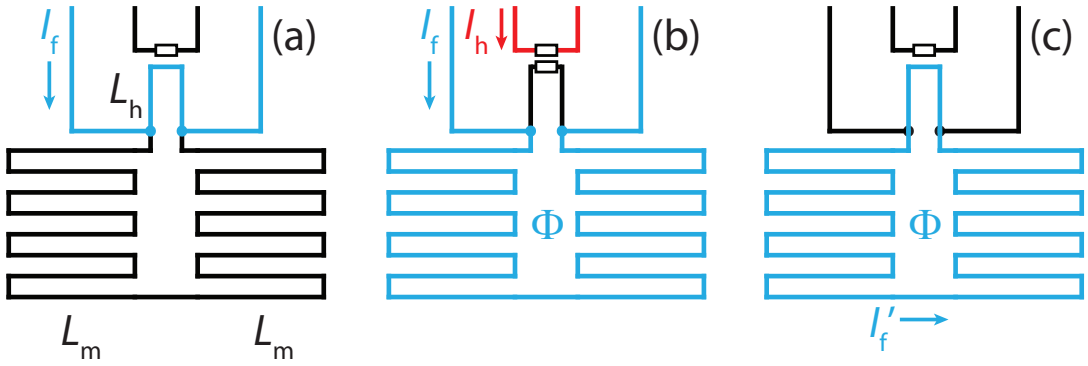

Figure 3.3 The schematic of the injection of a persistent current into a meander-shaped pick-up coil. The different steps are explained in the text.

to $T > T_c$, where T_c is the superconducting transition temperature of the meander material, and the part close to the heater becomes normal-conducting.

This opens the superconducting loop and will lead the field current I_f to run through the still superconducting meander structures. In the pick-up coil the current will create the magnetic flux Φ, that can now enter the loop. Once the heater is switched off, the path close to the heater will become superconducting again, as seen in figure 3.3 (c). The flux Φ is now conserved in the closed superconducting loop and the external current source can be switched off. The flux Φ leads to a persistent current of

$$I'_f = I_f \frac{2\,L_m}{2\,L_m + L_h} \quad . \tag{3.4}$$

with the inductances of the meanders L_m and of the heater path L_h. Usually $L_h \ll L_m$ and therefore the assumption of $I'_f \approx I_f$ is valid.

The created field is an inhomogeneous multi-pole field of high order. This has the advantage that the magnetic field and the coupling strength drop rapidly with distance to the meander structures and reduces magnetic crosstalk between neighboring detectors. It also allows to have magnetic impurities in close-by structures, that are e.g. introduced into the absorber by ion-implantation (see chapter 3.5.1 and 4.1.2), without disturbing the detector signal.

3.3 SQUID read-out

To measure the change of flux in the pick-up coil after an incident energy deposition in an MMC, SQUIDs can be used, that transform the flux change into a change of voltage, that can be easily recorded. The fundamental physics of SQUIDs exceeds the scope of this work and can be found elsewhere, e.g. in [Cla06], and the following remarks will be limited to a phenomenological description and will focus mainly on the use of dc-SQUIDs in combination with MMCs and the read-out as it was used for the experiments conducted in this work.

dc-SQUIDs, as shown in the schematic in figure 3.4 (a), consist of a superconducting loop, that is interrupted by two weak links, so-called Josephson junctions, which are mostly made of a thin layer (thickness $\sim$ nm) of a metal oxide between two superconducting leads. This combination allows the use of an elaborate combination of the Josephson effect and the macroscopic wave function that can be used to describe the coherent motion of Cooper pairs in a superconductor. The first consequence of the coherent motion is the flux quantization in closed superconducting loops to integer multiples of the magnetic flux quantum $\Phi_0 = h/2e \approx 2.07\,\mathrm{Wb}$.

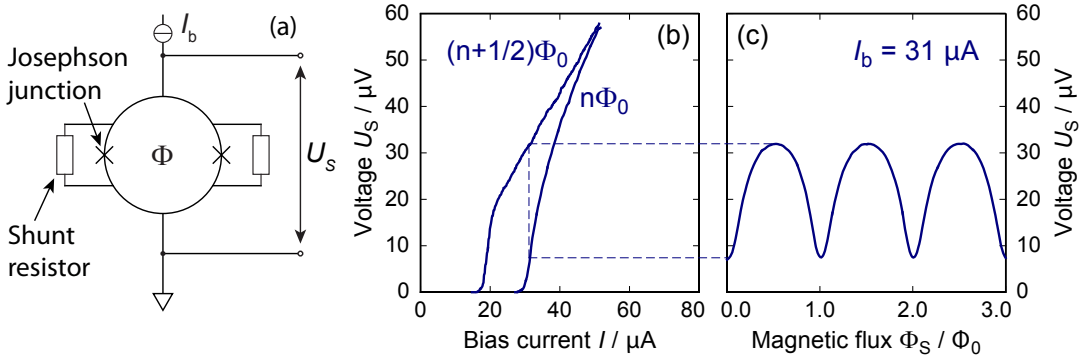

Figure 3.4 (a) Schematic of a SQUID (b) $I-U$ characteristics for the extreme flux states $\Phi = n\Phi_0$ and $\Phi = (n+1/2)\Phi_0$ (c) The $\Phi - U$ characteristics for a bias current of $I_\mathrm{b} = 31\,\mu\mathrm{A}$

As predicted in [Jos62], Cooper-pairs can tunnel through a Josephson junction up to a critical current I_c without any voltage drop. Once I_c is exceeded the supercurrent of I_c still flows but the excess current is carried by tunneling quasiparticles –electrons from broken Cooper-pairs– and a voltage drop is created across the junction. Additionally the wave function describing the Cooper pair motion will exhibit a phase shift δ when crossing the junction.

Maximum supercurrent The maximal supercurrent I through the device with two identical weak links A and B, which both show a critical current I_c, can maximally reach $I = 2\,I_\mathrm{c}$, but is also limited by the phase shift at each junction δ_a and δ_b:

$$I = I_\mathrm{c}(\sin\delta_\mathrm{a} + \sin\delta_\mathrm{b}) = 2I_\mathrm{c}\cos\left(\frac{\delta_\mathrm{a}-\delta_\mathrm{b}}{2}\right)\sin\left(\frac{\delta_\mathrm{a}+\delta_\mathrm{b}}{2}\right) \quad . \tag{3.5}$$

Additionally the circular current or screening current I_s of the device needs to fulfill the condition of magnetic flux quantization, even though flux quanta can enter or leave the loop through the weak links. Based on this fact a condition on the phase difference $(\delta_\mathrm{a} - \delta_\mathrm{b})$ can be calculated by integrating the vector potential $\boldsymbol{A}$ over a closed path $\boldsymbol{s}$ through the SQUID loop:

$$(\delta_\mathrm{a} - \delta_\mathrm{b}) = \frac{2e}{\hbar}\oint \boldsymbol{A}\,\mathrm{d}\boldsymbol{s} = \frac{2e\Phi}{\hbar} = \pi\frac{\Phi}{\Phi_0} \quad . \tag{3.6}$$

Here, Φ is the magnetic flux through the SQUID loop. Inserting equation (3.6) into equation (3.5) results in:

$$I = 2I_\mathrm{c}\sin\left(\frac{\delta_\mathrm{a}+\delta_\mathrm{b}}{2}\right)\cos\left(\pi\frac{\Phi}{\Phi_0}\right) := I_\mathrm{max}\cos\left(\pi\frac{\Phi}{\Phi_0}\right) \quad , \tag{3.7}$$

and by defining the maximum supercurrent $I_{\max} := 2I_c \sin(\delta_a + \delta_b/2)$, a convenient expression for the flux dependence of I can be found. The phase angle $(\delta_a + \delta_b)$ will also vary the amplitude of I with changing magnetic field, but with much weaker impact than the phase difference $(\delta_a - \delta_b)$ and can be neglected for small flux changes of a few Φ_0. Since the flux dependence shows an interference pattern, this effect is called "Quantum Interference".

Normal SQUID operation Under normal operating conditions one is interested in a flux dependent voltage drop across the SQUID, which is generated by biasing the SQUID with a current $I_b \geq I_{\max}$. The SQUID will always be in a resistive operating mode and a voltage drop will occur due to quasiparticle tunneling. Assuming a constant normal conducting resistance R_{sq} for the SQUID the following voltage drop can be deduced:

$$U(\Phi) = R_{sq} \left(I_b - I_{\max} \cos\left(\pi \frac{\Phi}{\Phi_0} \right) \right) \quad . \tag{3.8}$$

This simple representation easily illustrates the basic principle of a SQUID and shows estimates of the general behavior. A major factor that is not covered by this model is hysteresis, which can be avoided by connecting a correctly dimensioned shunt resistor in parallel to each junction, as already present in the schematic of figure 3.4 (a). Apart from that, figure 3.4 (b) also shows the $I_b - U$ characteristic for the extreme flux states of $\Phi = n\Phi_0$ and $\Phi = (n + 1/2)\Phi_0$, and figure 3.4 (c) the $\Phi - U$ characteristic for usual operation conditions of $I_b \geq I_{\max}$, which resembles a sinusoidal curve as expected from equation (3.8).

3.3.1 SQUID linearization

While the SQUID itself enables very sensitive flux measurements the $\Phi - U$ characteristic unfortunately is highly non-linear and can only be assumed to be linear in a flux range of approximately $\Delta\Phi \approx \Phi_0/4$ and to accurately detect larger flux changes a linearization scheme is necessary. Commonly a feedback circuit, also known as flux locked loop (FLL) circuit, is used for linearization.

The idea is that the SQUID is always kept at the same flux level, or the same working point, and the feedback signal that is necessary to achieve the compensation is used as a measure of the flux change $\Delta\Phi$ in the SQUID loop.

The voltage across the SQUID is measured with a differential amplifier and compared to a preset voltage U_b, which defines the working point, and is usually chosen to be at a point with the largest voltage per flux change $\partial U/\partial\Phi$. The output of

the differential amplifier is fed into a voltage integrator, whose output signal U_{out} is fed to a feedback resistor R_{fb} and transformed into a current signal $I_{\text{fb}} = U_{\text{out}}/R_{\text{fb}}$. This current is sent to an additional feedback coil closely coupled to the SQUID, where it creates the compensating flux $\Delta\Phi_{\text{fb}}$. The output voltage of the integrator U_{out} can be used as the output signal, since it is proportional to the feedback flux, according to $\Delta\Phi_{\text{fb}} = M_{\text{fb}}U_{\text{out}}/R = -\Delta\Phi$, with the mutual inductance M_{fb} between feedback coil and SQUID.

3.3.2 2-stage SQUID setup

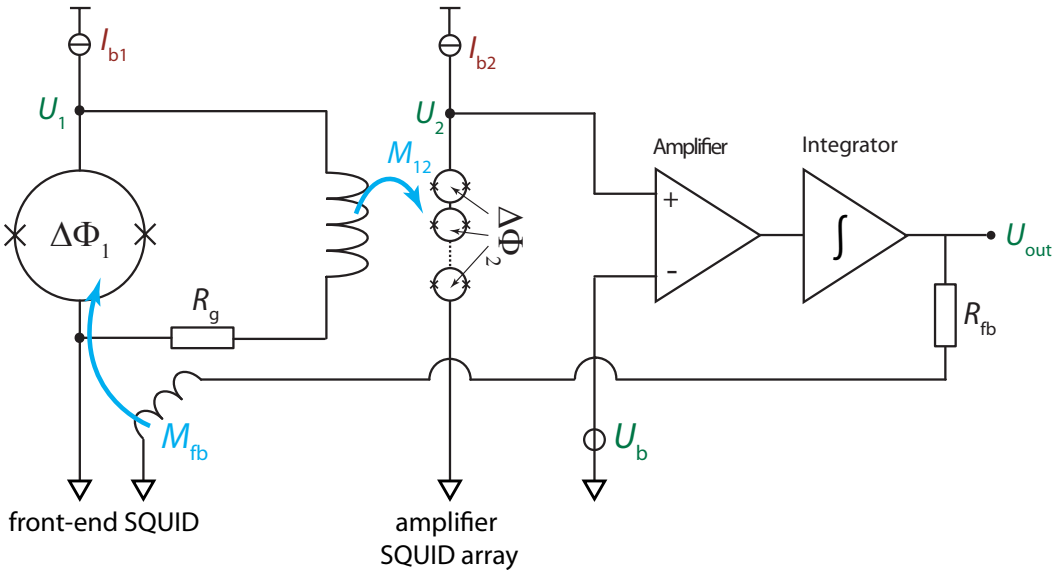

Figure 3.5 Schematic of a two stage SQUID setup including the flux locked loop circuit for linearization of the front-end SQUID.

The FLL electronics is operated at room temperature and even the best room temperature amplifiers can not compete with the unprecedented sensitivity of SQUIDs and the achievable noise level will be limited by the room temperature circuitry. To avoid this limitation a low-noise cryogenic pre-amplifier, e.g. also a SQUID or a SQUID series array, can be used.

In this scheme, shown in figure 3.5, the flux signal $\Delta\Phi_1$ of the first stage SQUID, often also called detector or front-end SQUID, creates a voltage signal ΔU_1 and is transformed into a current signal $\Delta I_1 = \Delta U_1/R_{\text{g}}$ with a gain resistor R_{g}. This current flows into the input coil of a second stage or amplifier SQUID, where a flux signal $\Delta\Phi_2 = M_{12}\,\Delta I_1$ is created. Here, M_{12} is the mutual inductance between the amplifier SQUID loop and the corresponding input coil.

Even though a flux-to-flux amplification of $G_\Phi = \Delta\Phi_1/\Delta\Phi_2 \approx 1$ is normally

achieved in setups as used within this work, a lot can be gained from this scheme, especially when using SQUID series arrays as amplifiers.

SQUID series arrays consists of n virtually identical SQUIDs connected in series. For amplifier SQUID arrays normally used for MMC read-out, the number can be $n = 14$ or $n = 16$. If all SQUIDs are biased at the same working point and are exposed to the same flux, which is usually achieved with a common input coil, the array acts as a single SQUID but with a larger voltage swing U_{pp}, which scales with n, while the input signal couples coherently into the n SQUIDs, the noise of the single SQUIDs is added incoherently, which means that the total noise of the array only scales with $\sqrt{n}$.

The 2-stage SQUID setup can be optimized so that the total flux noise is dominated by the flux noise of the front-end SQUID, which couples coherently into the SQUIDs of the array. In fact due to the larger voltage output of the array, the relative impact of the voltage noise of the room temperature electronics can be decreased down to a negligible level.

3.4 Detector prototype for the ^{163}Ho electron capture spectroscopy

The aim of the detector design was to already fulfill the demands of a large scale neutrino mass experiment on the single detector level. These demands are an energy resolution $\Delta E_{\mathrm{FWHM}} < 10\,\mathrm{eV}$, in the energy range below $E < 3\,\mathrm{keV}$, and a detector rise time on the order of $\tau_0 \approx 100\,\mathrm{ns}$, as for typical MMC designs.

The second aspect entering the design considerations is the ^{163}Ho source. The ^{163}Ho should be in atomic form inside of the gold absorbers, to prevent degrading effects due to chemical bonds of the ^{163}Ho atoms, and ion-implantation was considered for the deposition. The possibility of an ion-implantation in an online process at the ISOLDE[1] facility at CERN[2] was considered, which will be described in the following chapter 3.5. For this process the detector is exposed to an ion-beam with a diameter of approximately $d \approx 2\,\mathrm{mm}$. This gives the area, where the detectors can be located. Once the ^{163}Ho atoms have been implanted, an additional absorber layer needs to be added to the detector in order to create the 4π-geometry for the calorimetric measurement. All processes needed for the fabrication of the detectors should be compatible with the thin film micro-fabrication capabilities at the Kirchhoff-Institute for Physics of Heidelberg University, where this work was

[1] Isotope Separator On-Line Device

[2] Conseil Européen pour la Recherche Nucléaire – European Organization for Nuclear Research in Geneva, Switzerland

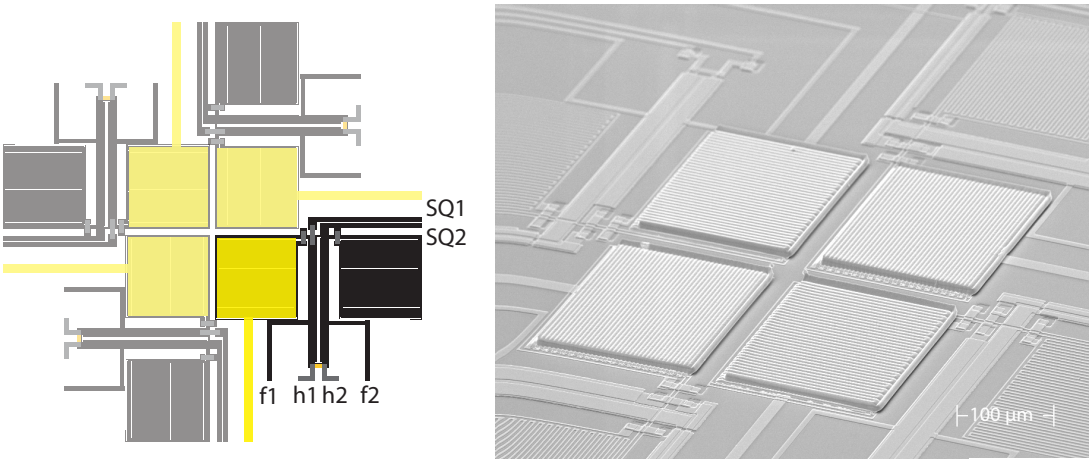

Figure 3.6 The top view on the center part of the detector design is shown with the four virtually identical detectors rotated around the center (left). In this way the active area of the detectors is confined on a small space allowing an efficient implantation. Additionally a SEM picture of the center part of a chip processed up to the first absorber layer is shown (right).

conducted.

Using all these requirements, the design of the first prototype of an MMC for the calorimetric measurement of the ^{163}Ho electron capture spectrum was developed [vS09].

A schematic of the design is shown in figure 3.6 together with a scanning electron microscope (SEM) picture of the center part of the detector chip. The detector is fabricated on a silicon substrate and each chip covers an area of 5 mm × 5 mm. The chip contains 4 virtually identical detectors rotated around the center of the substrate. This geometry was chosen to have a simultaneous ion-implantation without changing the focus point of the ion-beam.

The single detector consists of 8 thin film layers as shown in the blow-up cartoon in figure 3.7. The first layer made of 400 nm niobium contains the superconducting meander-shaped pickup-coil with a stripe width of $w = 2.5\,\mu$m and a pitch of $p = 5\,\mu$m, and most of the electronic circuitry. Afterwards the outer surface of the niobium is electrochemically oxidized to form $\sim$ 30 nm Nb_2O_5 and covered with 200 nm SiO_x as an insulation layer (not shown in figure 3.7) and only small areas are left open for electrical contacts. The third layer is made of 75 nm Au:Pd and acts as resistive heater for the persistent current switch, that is used to prepare the field generating persistent current in the meander-shaped pickup-coil. As fourth layer once again 700 nm thick niobium is used to provide further electrical contacts between separated elements of the first niobium layer, so-called vias, and to contact the persistent current switch. Next, as a fifth layer, 200 nm of gold are deposited, which is used to thermally contact the detector and adjust the thermal relaxation

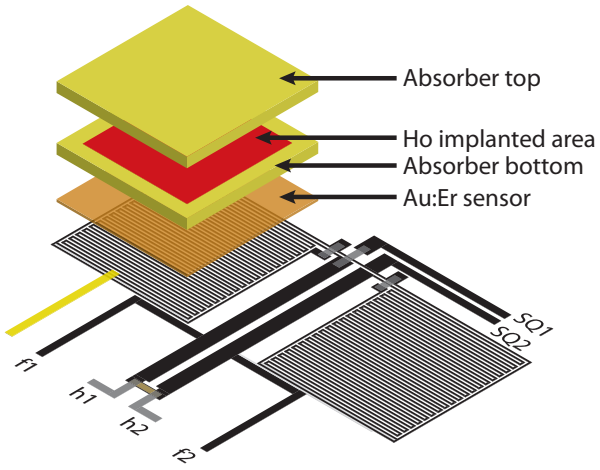

Figure 3.7 The blow-up cartoon of a single detector. The different layers can be seen, first the read-out structures, namely the first Nb layer (black) making up most of the superconducting circuity including the meander shaped pick-up coil, the Au:Pd heater in yellow contacted by the two lead label "h1" and "h2", and the second Nb layer (grey). Afterwards follow the "active' parts of the detector, namely the thermalization lead (thin yellow stripe) and the detector stack made of Au:Er (orange), the first absorber layer (yellow), the ion-implanted source area (red) and the second absorber layer (again yellow).

time. This is followed by 190 µm × 190 µm × 1.3 µm of the sensor material Au:Er above one of the meander wings of the pick-up coil. On top of the sensor, contacted over the full sensor area, is the first 185 µm × 185 µm × 5 µm gold absorber layer, which is ion-implanted at ISOLDE/CERN on a slightly reduced 160 µm × 160 µm area. This ion-implanted area was covered with a ∼ 100nm of gold about three months after the implantation still at CERN to enclose the radioactive material. After the detector was brought back the second 185 µm×185 µm×5 µm gold absorber layer was added.

The thin films of the detector structures are deposited by sputter deposition, apart from the first gold absorber layer, which is fabricated by electroplating. For details on the deposition techniques and the equipment used in the Kirchhoff-Institute for Physics, the reader is referred e.g. to [Pie12a]. The structuring is done in photolithographic processes, as e.g. described in [Pie08, Pab08].

The detector parameters are optimally balanced for an operating temperature of $T = 30\,\mathrm{mK}$, with the chosen geometry of the pick-up coil and an erbium concentration in the sensor of $C = 255\,\mathrm{ppm}$, and the gold thermalization structure is adjusted to allow a thermal relaxation time of $\tau_1 = 3\,\mathrm{ms}$ at $T = 30\,\mathrm{mK}$.

In combination with a state of the art dc-SQUID for the read-out and considering the known noise contributions and thermodynamic properties, the single detector should reach an energy resolution of $\Delta E_{\mathrm{FWHM}} \approx 2\,\mathrm{eV}$.

3.5 Ion-implantation at ISOLDE

After the detector chip has been processed to the first absorber layer the embedding of the ^{163}Ho needs to take place. After the restricted area of $160\,\mu\text{m} \times 160\,\mu\text{m}$ (shown in red in figure 3.7) had been defined by photoresist the chip was brought to the ISOLDE facility at CERN, where the embedding by ion-implantation took place.

The Isotope Separator On Line DEvice or short ISOLDE is embedded into the particle accelerator complex at CERN and uses the ISOL-technique (Isotope Separation On-Line) to produce ion-beams of radioactive and exotic nuclei. In the following a short introduction to the functioning principle and the capabilities of the ISOLDE facility is given, while a detailed description of both the technical and the physical aspects can e.g. be found in [FW00].

The facility was established in 1967 and in 1992 moved to a different location to be connected to the Proton Synchrotron Booster (PSB), that delivers 1.4 GeV protons to the ISOLDE facilities. ISOLDE contains two distinct target and ion source setups that are named after the mass separators connect to the targets, namely the General Purpose Separator (GPS) and the High-Resolution Separator (HRS). While the two mass separators differ in resolution and versatility, the basic functionality is the same.

The protons are guided into targets made of materials containing heavy nuclei, e.g. uranium carbide or tungsten, that are kept at elevated temperatures around $T = 2000\,^{\circ}\text{C}$. The energetic protons will be stopped in the target material and create lighter nuclei by spallation, fission or fragmentation reactions. Stimulated by the elevated temperatures the created nuclei can diffuse out of the bulk target material and are led into an ion-source, where the nuclides are ionized, either by hot surface, hot plasma or resonant laser ionization. The ionization chamber is held at an elevated voltage between $U = 30 \ldots 60\,\text{kV}$ and the created ions are accelerated and led to electro-magnet systems, where the ions are separated by their mass and led on to the experimental beam line. This mass-separator setup is where the two target stations are different. The HRS uses a more elaborate setup with two separator magnets and reaches a mass resolving power on the order of ~ 5000, while the GPS with a single magnet reaches a resolving power on the order of ~ 1000, but it allows to lead the lighter and heavier ions to two additional separate beam lines, where they can be used for additional experiments.

The mass separation allows only to select one isobaric family of nuclides, but the other parameters, like the target material, the target operating temperature, the proton energy or the ionization technique, allow to influence the element composition of the final ion-beam. And in this way the ISOLDE facility is able to provide quite pure ion-beams of approximately 70 elements and about 700 different isotopes.

These ions are used either by the eight permanently installed experiments or at different beam lines, that can be equipped with temporary experiments, typically lasting about a week.

3.5.1 ^{163}Ho implantation and element composition

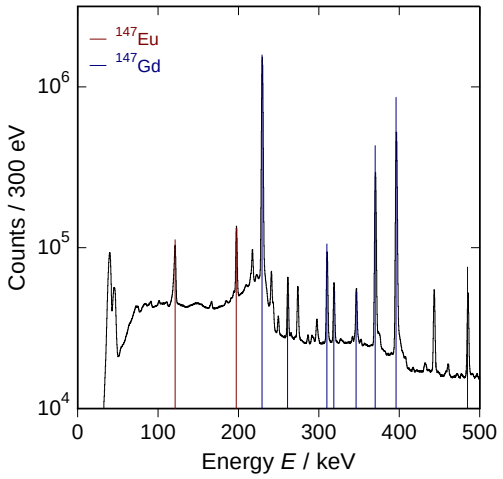

Figure 3.8 The γ-ray measurement of the ion-implanted sample shortly after the irradiation. Most of the observed lines can be identified with the main contaminants ^{147}Eu and ^{147}Gd. The γ-lines of these two elements are shown as vertical lines at the line energy, while the height gives the relative amplitudes.

For the production of ^{163}Ho a solid tantalum target at approximately $T = 1000\,\mathrm{K}$ was used at the GPS beam line of the ISOLDE facility. Surface ionization was used to extract the atoms from the target and the $^{163}Ho^{+}$ ions were led onto the detector with a beam current of $I_{\mathrm{ion}} = 75\,\mathrm{pA}$, which corresponds to approximately $n_{\mathrm{ion}} = 5 \times 10^{8}$ ions per second and the irradiation lasted for about $\Delta t = 40\,\mathrm{min}$. . Therefore approximately $n_{\mathrm{ion,\ tot}} = 10^{12}$ ions were implanted into the detector setup, while only a fraction of these ions were directly implanted into the detectors because of the restricted area of the detector surface. Assuming an ion-beam diameter of 2 mm with a homogeneous profile and the implantation area of a single detector of $160\,\mu\mathrm{m} \times 160\,\mu\mathrm{m}$, a total of $n_{\mathrm{tot,\ det}} = 10^{10}$ ions are expected in each detector, which roughly corresponds to an activity of $A = 0.1\,\mathrm{Bq}$ for ^{163}Ho. Only a fraction of the implanted ions is actually ^{163}Ho. In fact, while selecting the mass of $m = 163\,\mathrm{u}$, all isobaric ions as well as isobaric molecules present in the beam are selected. Within $m = 163\,\mathrm{u}$, the only stable nuclide is ^{163}Dy. ^{163}Hois the only one with a longer half-life, all other nuclides have half-lifes shorter than $T_{1/2} < 1.8\,\mathrm{h}$.

Therefore, a few days after the implantation, the atoms with mass $m = 163\,\mathrm{u}$ will only be ^{163}Dy and ^{163}Ho. The species that can be implanted as molecules are most likely in the form of oxides $^{147}X^{16}O$, but also fluorides $^{144}X^{19}F$ or more complicated molecules like dioxides $^{131}X^{16}O_2$ can be expected. To analyze the radioactive contaminations, the γ-rays from the the implanted detector chip were measured

with a germanium detector shortly after the implantation and the result of this measurement is shown in figure 3.8.

The most prominent radioactive isotopes identified in the γ-ray measurement are ^{147}Gd, which decays through electron capture with a half-life of $T_{1/2} = 38.06\,\mathrm{h}$ to ^{147}Eu. ^{147}Eu was also identified and decays with a half-life of $T_{1/2} = 24.1\,\mathrm{d}$ through electron capture to the quasi-stable ^{147}Sm, which decays through α-decay with a half-life of $T_{1/2} = 1.06 \times 10^{11}\,\mathrm{y}$. Since the first measurement with the implanted detector was performed approximately one year after the implantation took place, none of the mentioned contaminations will show a significant activity that will have a negative impact on the measurement. Secondly the number of atoms of the contaminating elements can be estimated from the observed activity of the γ-ray measurement, which results in a relative amount of $n_{\mathrm{cont}}/n_{\mathrm{tot}} \approx 10^{-3}$, which means that the total number of implanted ions is not even significantly influenced by these contaminations.

Another contaminant that was not identified by the γ-ray measurement, but in the calorimetric measurements is ^{144}Pm, which was implanted as $^{144}\mathrm{Pm}^{19}\mathrm{F}^{+}$. With the half-life of $T_{1/2} = 363\,\mathrm{d}$ of ^{144}Pm and the decays observed in the cryogenic measurements one can estimate that about $n_{^{144}\mathrm{Pm}} \approx 2 \times 10^6$ atoms were present after the implantation in every detector, which is also a relative amount of $n_{\mathrm{Pm}}/n_{\mathrm{tot}} \leq 10^{-3}$ and therefore also not significant on the total number of implanted atoms.

Within $m = 147\,\mathrm{u}$ and $m = 144\,\mathrm{u}$ are other isotopes with half-lifes large enough to be still present during the calorimetric measurements, namely ^{147}Pm with a half-life of $T_{1/2} = 2.62\,\mathrm{y}$ and ^{144}Ce with a half-life of $T_{1/2} = 284\,\mathrm{d}$. Since both of these are β-decaying nuclides they emit very small amounts of γ-rays and would not be detectable in the germanium detector. But they will most likely also be present with relative contributions on the order of $n/n_{\mathrm{tot}} = 10^{-3}$, similar to the other molecular contaminants, and have no impact on the total ion number.

Therefore, besides the small amounts of identified radioactive contaminants, the implanted atoms are all ^{163}Ho and the stable ^{163}Dy.

3.6 Experimental setup

After the ion-implantation took place and the second absorber layer was added to the detectors, the chip was glued into a dedicated experimental setup. The setup described here was used in run 3 and run 4 (see beginning of chapter 4), while the setup for run 1 and run 2 can be found in [vS09]. The main feature of the setup used for run 3 and run 4 was the possibility to read-out all four channels present on the chip.

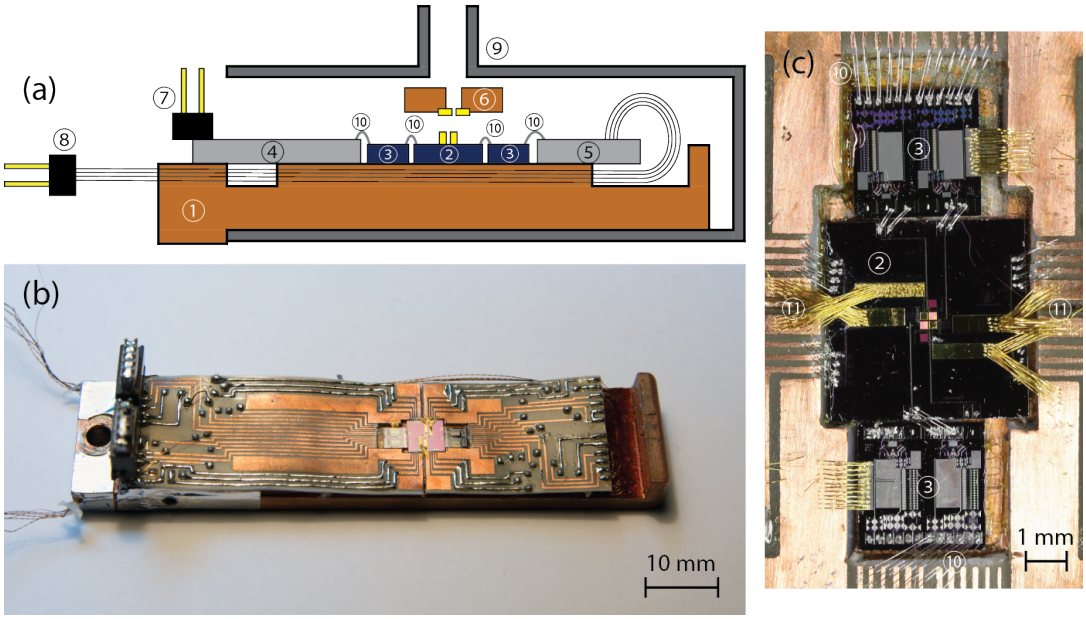

Figure 3.9 Overview over the experimental setup. (a) Schematic side-view (b) Photograph of the setup (c) Zoom into the central region showing the detector and SQUID chips

Only two detectors were measured in the final experiments, since the other two were not working. The magnetization signal of the two detectors was read-out using a 2-stage SQUID configuration. The detector SQUID and the amplifier SQUID array with 14 single SQUIDs were fabricated on the same chip. The chip for the complete 2-stage read-out is called C6X114W and has been produced at the Physikalisch Technische Bundesanstalt (PTB), Berlin, Germany.

The experimental setup is shown in figure 3.9 and is build onto an 18 mm × 80 mm experimental holder made of solid copper ①. The holder was additionally structured to have an elevated 23 mm × 16 mm platform. The detector ② and SQUID chips ③ were glued to this platform with GE 7031 varnish. The chips are surrounded by PTFE based circuit board CuFlon[3] ④+⑤, that provides the electrical connections for the read-out. The circuit board is glued with Stycast 2850 FT[4] to the elevated platform, while the remaining part of the circuit board is left flexible to allow bending due to the different coefficients of thermal expansion of the base material PTFE and the plating material copper.

To avoid electrical contact between the circuit board and the lower level of the experimental holder the surface of the holder is covered with Kapton foil.

[3]by Polyflon Company, One Willard Road, Norwalk, CT 06851, USA, URL `http://www.polyflon.com`

[4]by Emerson&Cuming, part of Henkel Corporation, 15350 Barranca Parkway, Irvine, CA 92618 USA, URL `http://www.henkel.com`

The front circuit board ④ is directly equipped with connectors ⑦, while the connections to the rear circuit board ⑤ are made with NbTi wires soldered to the circuit board. These wires are led in a groove below the circuit board to the front to have all connectors ⑧ combined on one side. The electrical connection from the circuit board to the chips and from the SQUIDs to the detector chip are made with wedge bonded 25 µm aluminum wires ⑩. At the usual operating temperature around $T = 30\,\mathrm{mK}$ the aluminum wire bonds are far below the critical temperature of $T_\mathrm{c} \approx 1.2\,\mathrm{K}$ and can establish superconducting connections.

Additionally both the detectors and the SQUIDs are thermally connected with wedge bonded 25 µm gold wires ⑪ to large copper areas on the circuit boards to enhance the thermal contact to the experimental platform.

For the measurements with an external calibration source (run 3) a collimator ⑥ was added. It consists of a 2 mm wide copper bridge with a hole in the middle, having a diameter of $d = 1\,\mathrm{mm}$. An additional $\sim 100\,\mu\mathrm{m}$ thick gold foil, having a hole with a diameter of $d \approx 100\,\mu\mathrm{m}$, was glued to the bridge towards the detector to reduce the collimation hole. This tiny hole is positioned above one of the detectors to make sure that the radiation from the external source only hits the one detector.

The whole setup is then placed in shielding ⑨ to shield the setup from time varying magnetic fields. The shield was made out of $\sim 1\,\mathrm{mm}$ thick welded lead, that is also superconducting a the operating temperature. To achieve the best possible magnetic shielding the lead shield is only open to the front side of the setup and the detector and SQUID chips are as far inside the shield as possible. For the measurements with the external source a $d \approx 2\,\mathrm{mm}$ hole was drilled into the lead shield above the detectors. To not compromise the magnetic shielding due to the hole a $l \approx 2.5\,\mathrm{cm}$ long welded lead cylinder with a diameter of $d \approx 2\,\mathrm{mm}$ was soldered on top of the hole as indicated in figure 3.9 (a).

3.7 ^{55}Fe X-ray calibration source

For the detector characterization and the energy calibration of the measured spectra an external ^{55}Fe X-ray calibration source was used. ^{55}Fe decays via electron capture to ^{55}Mn with a half-life of $T_{1/2} = 2.73\,\mathrm{y}$. About 28.4 % of the decays will end up emitting X-rays from the K-shell, which are divided into transitions to the L- and the M-shell. 89.5 % of the radiative K-transitions are to the L-shell under emission of a K_α X-ray with an energy of $E_{K_\alpha} = 5.895\,\mathrm{keV}$, while the remaining 10.5 % go to the M-shell under emission of a K_β X-ray with an energy of $E_{K_\beta} = 6.490\,\mathrm{keV}$. Both the K_α- and the K_β-lines show fine structure splitting due to the transitions to the sub-levels of the L- and M-shells, which has been characterized with a high-

resolution crystal spectrometer in [Höl97].

The remaining 71.6 % of the decays result either in radiative transitions from the L-shell or de-excitations via Auger electrons, which are usually absorbed in the source housing and are of no interest for the calibration.

In case of the used ^{55}Fe calibration source[5], the source material is electroplated to the face of a copper cylinder, that is positioned in a vacuum tight stainless steel housing with a diameter of $d \approx 8\,\mathrm{mm}$ and a height of $h \approx 5\,\mathrm{mm}$. The side facing the ^{55}Fe is welded shut with a 250 µm thick beryllium X-ray window. In this way the source material is completely enclosed and no source material can exit the housing and contaminate the surrounding. Secondly the X-ray window allows photons with an energy of $E = 6\,\mathrm{keV}$ to pass with a probability of $p = 89.0\,\%$, while electrons and L-transition X-rays are stopped with $p \approx 100\,\%$. Therefore only the highest energetic K_α and K_β X-rays can leave the source and can be used for calibration.

The source was delivered in late 2008 with an initial activity of $A = 40\,\mathrm{MBq}$ and by the time the measurements of this work took place in late 2012, the total activity had reduced to $A \approx 9\,\mathrm{MBq}$.

3.8 Room temperature electronics and data acquisition

The room temperature read-out starts with the flux locked loop circuit for the SQUID linearization. This part is taken over by the XXF-1[6] SQUID electronics, that contains the electronics for the SQUID operation, the FLL circuit and a pre-amplifier. The output voltage signal is then separated into two signal chains, that are individually amplified and band-pass filtered with SR560[7] low-noise pre-amplifiers.

One signal chain is used as the trigger signal that is strongly high-pass filtered, e.g. with a cut-off frequency of $f_0 = 100\,\mathrm{Hz}$, and low-pass filtered, e.g. with a cut-off frequency of $f_0 = 10\,\mathrm{kHz}$. When no thermal pulses are present the resulting signal is centered around $U = 0\,\mathrm{V}$. The noise level is very small, so that it is easier to identify the rising slope corresponding to the starting of a thermal pulse. A trigger voltage can be set very close to the noise level to acquire the pulses from very small energies, or can be set to higher voltages, if only larger pulses are of interest.

In the second signal chain the voltage signal is recorded as undisturbed as possible.

[5] by QSA Global Inc., 40 North Avenue, Burlington, MA 01803, USA URL `http://www.qsa-global.com`

[6] by Magnicon GmbH, Barkhausenweg 11, 22339 Hamburg, Germany URL `http://www.magnicon.com`

[7] by Stanford Research Systems Inc., 1290-D Reamwood Avenue, Sunnyvale, CA 94089, USA URL `http://www.thinksrs.com`

This means that it is only low-pass filtered to fulfill the Nyquist-Shannon theorem to avoid aliasing effects.

Two different high-speed digitizers with 12 bit resolution, namely a CompuScope SAC-8012A/PCI card and a CompuScope SAC-12100 card[8] were used for the digitization. Usually a time-window with $\sim 20\,\mathrm{ms}$ length was recorded with 16384 individual data points. The first quarter of the time-window recorded the signal before the start of the actual event. This part contains information about the detector temperature because of the sensor magnetization and can be used to correct the signal amplitudes, as will be described in chapter 4.2.2.

Additionally one time-window, where the preset trigger level was not exceeded, after each five triggered signals was recorded. These so-called baselines allow to calculate the noise spectrum of the device by discrete Fourier transform. These can be used for noise analysis.

3.9 Digital data analysis

The previously described data acquisition system allows to measure the voltage signal, that corresponds to an energy input. The algorithm to extract the energy information from the voltage signal can strongly influence the achieved resolution. An established algorithm that shows very good results and can be implemented at moderate computational cost is the optimal or matched filter algorithm. A general introduction to this algorithm can e.g. be found in [McC05b], while a detailed discussion with a focus on metallic magnetic calorimeters is given in [Fle03a].

The algorithm is based on the idea to find a weighting filter function, that can be convolved with every single event in time domain, that uses the optimal signal-to-noise ratio (SNR), as determined in frequency space. To calculate the filter function an average of several similar single events is taken to form a pattern event, which is then transformed into frequency space via discrete Fourier transform. The same procedure is applied to several baselines, that are measured alongside the triggered signals, which are first Fourier transformed and then averaged in frequency space.

The Fourier transform of the pattern event is then divided by the baseline Fourier transform, which gives the signal-to-noise ratio in the frequency domain. By transforming the SNR back into the time domain the filter function is determined.

The maximum of the curve created by convolving the filter function with an event is a measure for the incident energy of the event.

[8] both systems by GaGe Applied Technologies, part of DynamicSignals LLC, 900 N. State Street, Lockport, IL 60441, USA URL `http://www.gage-applied.com`

4. Experimental results

The experimental results discussed in the following were all obtained with the detector described in chapter 3.4. Mostly the one detector, that was ion-implanted at the ISOLDE-CERN facility as described in chapter 3.5, was used. Measurements with this detector were taken in four different experiments using different setups that are summarized in table 4.1.

The first run in August 2010 aimed to understand the detector behavior after the implantation took place. Only one of the four detector channels was read-out. The detector was characterized with a weak external ^{55}Fe with about 6×10^{-4} cps in the detector. The second run in November 2010 used the same setup but aimed for a characterization at different temperatures allowing for a better understanding of the thermodynamic properties of the detector. This run also involved a longer spectrum measurement over the course of three days.

For run 3 between September and December 2012 the experiment was entirely redesigned as described in chapter 3.6 to allow the read-out of all four channels on the detector chip. Only two channels were working and were measured in the experiment. With this measurement we could precisely calibrate the spectrum with an external ^{55}Fe source with a rate of 5.5×10^{-3} cps collimated on one of the two detectors. Additionally a "high statistics" spectrum with about 40 000 events in the final ^{163}Ho electron capture spectrum was acquired, over the course of several month of continuous measurement.

Run 4 had the goal to lower the background level and to improve the low energy threshold. The setup was modified as will be described in 4.2.6. And a different

	Start date	Δt	Ch #	SQUID(s)	External source
Run 1	08/2010	8 h	2	C4X1W+C5X16W	^{55}Fe (weak)
Run 2	11/2010	40 h	2	C4X1W+C5X16W	^{55}Fe (weak)
Run 3	09/2012	45 d	2, 4	C6X114W	^{55}Fe
Run 4	06/2013	21 d	2, 4	C6X114W	none

Table 4.1 Overview over the 4 runs of measurement with the ion-implanted detector chip. The start date, the longest spectrum measurement Δt, as well as the numbers of read-out channels, the used SQUIDs and the used external calibration source are quoted. The purpose and a brief overview of the obtained results of the different runs is given in the text.
All used SQUIDs are fabricated by the Physikalisch Technische Bundesanstalt (PTB), Berlin and are described in [Dru07] or are similar to the devices therein.

data acquisition system was used as will also be discussed in chapter 4.2.6. This modified setup was successfully used over the course of about 2 months, acquiring a second "high-statistics" spectrum with about 20 000 events.

4.1 Detector characterization

As described in the appendix A.4 the thermodynamic properties of metallic magnetic calorimeters are very well understood and can be accurately simulated. Therefore a first test is to check if the thermodynamic properties have been influenced by the implantation process. This was done by both a comparison to the numerical calculations as well as to the performance of a second detector[1] having the same detector design, that did not undergo the implantation process.

The second non-implanted detector was only processed to the first absorber layer. This difference was taken into account while comparing the properties of both detectors. The characterization of this detector was done in [vS09]. Part of the data have been reanalyzed and are reproduced in this work.

4.1.1 Coupling

To be able to correctly interpret the SQUID signal following an event in the detector it is important to understand the coupling of the magnetization signal of the sensor material Au:Er to the SQUID. While the amplitude of the magnetization signal is mostly influenced by the distribution and magnitude of the applied magnetic field, the coupling is given by the involved inductances. These are the inductances of the double meander of the detector, the inductance of the SQUID input coil and a stray inductance, that is mostly created by the aluminum wire bonds connecting detector and SQUID input coil. While the inductances can be simulated e.g. by finite element methods the experimentally determined inductances are mostly larger by roughly a factor of 2 compared to the simulations.

The flux coupling k_Φ for a gradiometric double meander to a SQUID input coil, as shown in the inset of figure 4.1, is given by:

$$k_\Phi = \frac{M_{\mathrm{is}}}{L_{\mathrm{m}} + 2\,(L_{\mathrm{i}} + L_{\mathrm{w}})} \ , \tag{4.1}$$

with the inductance of a single meander L_{m} and of the SQUID input coil L_{i}, the mutual inductance M_{is} between input coil and SQUID, as well as an additional

[1] Called the "non-implanted detector" in the following

stray inductance L_{w} dominated by the connecting aluminum bonding wires between detector and SQUID chip.

The input and mutual inductances of both of the used SQUID chips (see table 4.1) are specified by the manufacturer to be:

$$L_{\mathrm{i}} = 1.8\,\mathrm{nH} \tag{4.2}$$

$$M_{\mathrm{is}}^{-1} = 5.7\,\frac{\mu\mathrm{A}}{\Phi_0}\ , \tag{4.3}$$

with the magnetic flux quantum $\Phi_0 = h/2e \approx 2.07 \times 10^{-15}\,\mathrm{Wb}$.

The total inductance connected to the SQUID can be measured while the aluminum wire bonds are still normal conducting ($T > T_{\mathrm{c,\ Al}} = 1.175\,\mathrm{K}$) and act as white noise sources according to the fluctuation-dissipation theorem [Joh28, Nyq28] with the spectral density of the current fluctuations of:

$$S_{\mathrm{I}} = \frac{\langle I^2 \rangle}{\Delta f} = \frac{4 k_{\mathrm{B}} T}{R} \tag{4.4}$$

over the bandwidth Δf with the Boltzmann constant $k_{\mathrm{B}} \approx 1.38 \times 10^{-23}\,\mathrm{J/K}$, the temperature T and the normal state resistance R.

The resistance R of the wires combined with the total inductance L_{tot} of the circuit forms an LR-circuit acting as a low-pass filter with the characteristic cut-off frequency of:

$$f_0 = \frac{R}{2\pi\, L_{\mathrm{tot}}}\ . \tag{4.5}$$

Figure 4.1 shows an exemplary flux noise spectrum measured with channel 4 prior to run 3 in a liquid helium storage dewar at $T = 4.2\,\mathrm{K}$. For frequencies lower than $f < 10^5\,\mathrm{Hz}$ the noise is white with a level given by eq. (4.4). The intermediate frequencies up to $f \approx 3 \times 10^6\,\mathrm{Hz}$ are dominated by the low-pass with the cut-off frequency f_0 given by eq. (4.5). At high frequencies larger than $f > 3 \times 10^6\,\mathrm{Hz}$ the white noise contribution of the SQUID $S_{\Phi,\ \mathrm{SQ}}$ starts to influence the spectrum and leads to the second cut-off, that is caused by the finite SQUID bandwidth. The total spectrum can be described by:

$$S_\Phi(f) = M_{\mathrm{is}}^2\, S_{\mathrm{I}}(f) = M_{\mathrm{is}}^2\, \frac{4 k_{\mathrm{B}} T}{R}\, \frac{1}{\left(1 - \frac{f}{f_0}\right)} + S_{\Phi,\ \mathrm{SQ}}\ . \tag{4.6}$$

Fitting the data with least-square fit algorithm finds

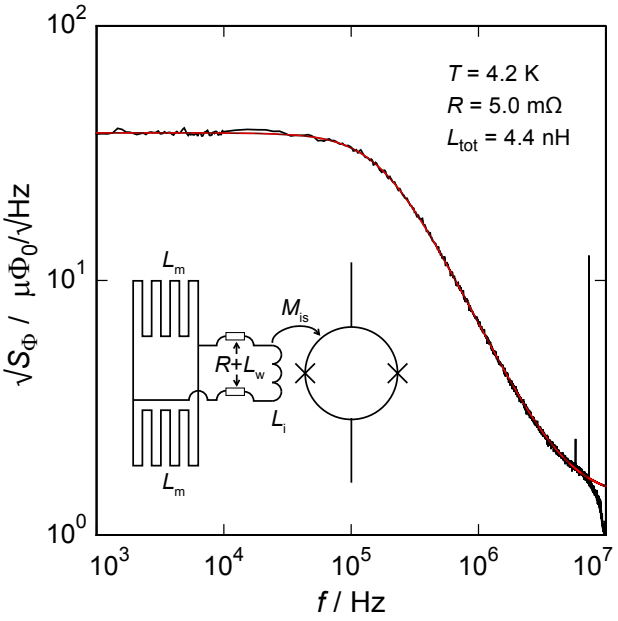

Figure 4.1 The measured spectral flux density in the SQUID for detector channel 4 before run 3. The data is shown in black while the fit with the parameters quoted in the graphic is shown by the red dashed line. The inset shows the schematic setup of the measurement.

$$L_{\mathrm{tot}} = 4.4\,\mathrm{nH} \text{ and} \tag{4.7}$$
$$R = 5.0\,\mathrm{m\Omega} \tag{4.8}$$

and by using Kirchhoff's circuit laws on the setup (shown schematically in the inset of figure 4.1) one finds:

$$L_{\mathrm{tot}} = L_{\mathrm{i}} + L_{\mathrm{w}} + \frac{L_{\mathrm{m}}}{2} \ . \tag{4.9}$$

The stray inductance caused by the aluminum bonding wires was empirically found to be

$$L_{\mathrm{w}} \approx 0.15\,R\,\frac{\mathrm{nH}}{\mathrm{m\Omega}} = 0.75\,\mathrm{nH} \ , \tag{4.10}$$

which lets us determine the meander inductance to be

$$L_{\mathrm{m}} = 3.7\,\mathrm{nH} \ , \tag{4.11}$$

compared to the simulated value of $L_{\mathrm{m}} = 2.0\,\mathrm{nH}$ this is significantly larger. The cause of the disagreement has not been found, but possible explanations are fabrication imperfections and the simplified geometry used in the simulations. For larger meander structures, as e.g. described in [Pie12a], the discrepancy becomes negligible.

Finally the coupling (eq. (4.1)) can be calculated to be

$$k_\Phi = 0.041 \ . \tag{4.12}$$

This characterization measurement was performed for every experiment prior to the cryogenic measurements and is already incorporated into the following analysis.

4.1.2 Magnetization

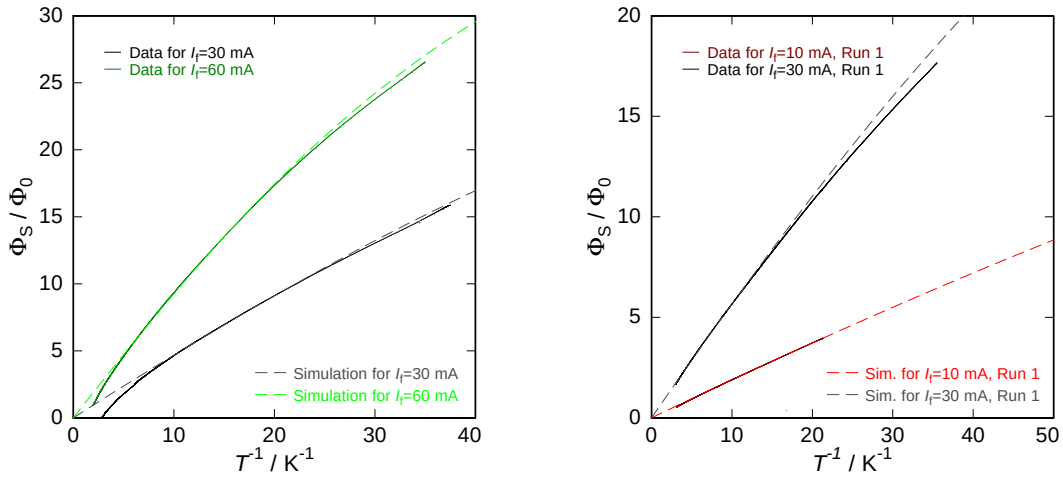

Figure 4.2 Magnetization data (solid lines) for the non-implanted detector (left) and channel 2 of the ion-implanted one (right) in comparison to simulated magnetization data (dashed lines) at different field generating currents I_f plotted against the inverse temperature. Deviations between data and simulation are caused by external magnetic fields at high temperatures (low T^{-1}), while at low temperatures (high T^{-1}) thermal decoupling from the thermal bath causes the smaller signal.

The magnetization measurement of the sensor material Au:Er is the temperature calibration for the used detectors and is therefore important for understanding the detector signal. Throughout the following chapters the magnetization changes are given in magnetic flux change in the front-end SQUID.

The experimental curves are compared to expected curves calculated using the properties of Au:$\mathrm{Er}_{255\ \mathrm{ppm}}$, whose erbium ion concentration has previously been measured on residual material from the micro-fabrication with a commercial MPMS XL5[2] magnetometer. Other parameters entering the calculated curves are the geometry of the meander and sensor as well as the injected field current, which allows the calculation of the magnetic field.

[2]by Quantum Design Inc., 6325 Lusk Boulevard, San Diego, CA 92121-3733, USA URL `https://www.qdusa.com`

More specific to this particular setup is the test of the magnetic influence of the implanted ^{163}Ho. Holmium atoms carry a magnetic moment and should show similar behavior to the Er ions in the sensor material of metallic magnetic calorimeters. This includes a magnetization signal in a weak magnetic field, that should show up in a magnetization measurement. This effect is described for the case of Er in Au in the appendix in chapter A.1. Additionally other isobaric nuclides or molecules, possibly with much stronger magnetic moments, can have been implanted together with the ^{163}Ho, as discussed in chapter 3.5.

The magnetization is measured by monitoring the SQUID signal and the temperature of the experimental platform while the temperature is slowly changed, both cooling and heating is possible. This allows the experiment itself to thermalize with the experimental platform. Figure 4.2 shows the measured magnetization both of the non-implanted detector (left) and of the ion-implanted detector (right) plotted against the inverse temperature T^{-1}, with the matching simulated data curves, clearly showing the expected quasi-linear Curie's law behavior (see appendix A.2). As can be seen, the measured data matches the simulation very well, except for small deviations at extreme temperatures.

The deviations at high temperatures (small T^{-1}) for the non-implanted detector (left plot) are caused by an external magnetic field from the adiabatic demagnetization refrigerator in combination with imperfect magnetic shielding. The deviations at low temperatures (large T^{-1}) are caused by thermal decoupling of the experiment. This is due to the power dissipation of the used front-end SQUIDs, that can be reduced by good thermal coupling between the thermal bath to both the SQUIDs and the detectors, but cannot be avoided entirely.

A particular case is the curve shown from run 4 in figure 4.3. In run 3 and 4 chips with both front-end SQUID and amplifier series SQUID array integrated on the same chip are used, which causes the power dissipation close to the detector to be strongly increased and the experiment strongly decouples from the thermal bath.

Based on the simulated magnetization data, the detector temperature in comparison to the bath temperature can be calculated as shown in figure 4.4 for run 4. As can be seen for the lowest bath temperatures around $T = 20\,\mathrm{mK}$, the detector temperature got as low as $T = 29\,\mathrm{mK}$ which is still low enough and around the optimal operation temperature for metallic magnetic calorimeters.

Ultimately no deviation, both between simulated and measured data and between the non- and the ion-implanted detector can be found, that can not be explained. That leads to the conclusion that the implantation process of ^{163}Ho and other lanthanoids in the absorber have no impact on the magnetization signal on the available accuracy level. This conclusion can be motivated due to large distance from the me-

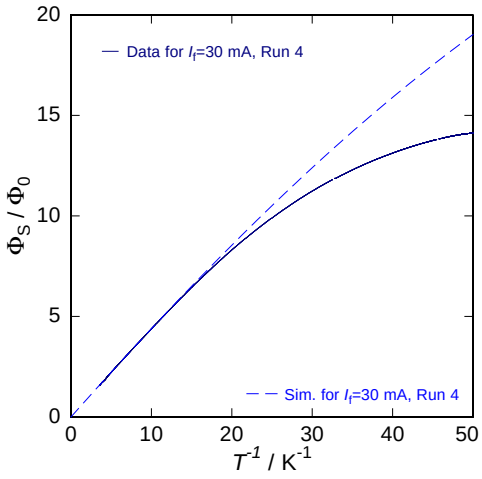

Figure 4.3 A magnetization measurement from channel 2, run 4 with $I_f = 30\,\mathrm{mK}$. At low temperatures the data strongly deviates from the calculation. This is due to the power dissipation of the nearby read-out SQUIDs, that keeps the detector temperature elevated compared to the thermal bath.

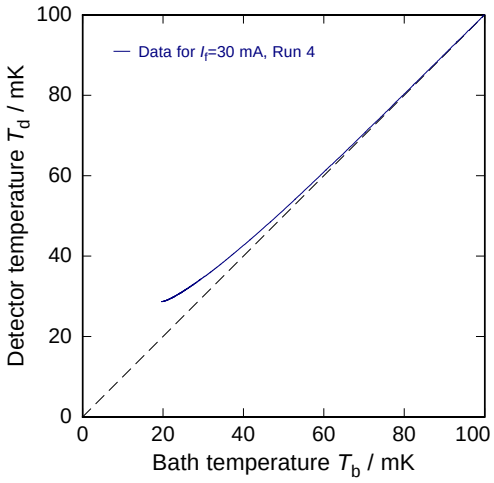

Figure 4.4 Temperature correction curve for the magnetization measurement of channel 2, run 4 of the ion-implanted detector shown in figure 4.3. The detector temperature starts decoupling from the thermal bath around $T = 80\,\mathrm{mK}$ and reaches $T_\mathrm{d} = 29\,\mathrm{mK}$ for the lowest bath temperature of $T_\mathrm{b} = 20\,\mathrm{mK}$.

ander shaped pick-up coil to the implantation area, which was about $d = 6.3\,\mu\mathrm{m}$, where the coupling to the pick-up coil is down to 0.03 compared to the average coupling in the Au:Er sensor volume. This is due to the fact that the meander geometry is optimized for the Au:Er sensor thickness of $h_{\mathrm{Au:Er}} = 1.3\,\mu\mathrm{m}$. Nonetheless it is satisfactory to have careful design decisions verified in experimental data.

4.1.3 Pulse shape

The signal shape of a metallic magnetic calorimeter is given by the point spread function, or the detector answer to a point-like excitation, and the signal amplitude.

In case of calorimetric detectors the signal amplitude is a rise in temperature

$$\Delta T \approx \frac{E}{C_\mathrm{tot}} \ , \tag{4.13}$$

depending on the incident energy E and the total heat capacity C_tot. For an MMC this temperature rise creates a flux signal in the SQUID of:

$$\Delta\Phi_\mathrm{S} = k_\Phi \frac{\partial M}{\partial T} \Delta T \approx k_\Phi \frac{\partial M}{\partial T} \frac{E}{C_\mathrm{tot}} \tag{4.14}$$

with the change of magnetization with temperature $\partial M/\partial T$, that is determined in the magnetization measurement.

With the magnetization and the coupling already known, only the heat capacity needs to be calculated to theoretically describe the signal amplitude. The specific heat per volume can be divided into three contributions:

- The electronic contribution c_e of sensor and absorber material,
- the phononic contribution c_{ph} of sensor and absorber material and
- the spin contribution of the paramagnetic ions in the sensor material, also called Zeeman-system, c_{Z}.

At temperatures much lower than the Debye temperature $T \ll \Theta_{\mathrm{D}}$ ($\Theta_{\mathrm{D}} = 164\,\mathrm{K}$ for gold) this adds up to:

$$c_{\mathrm{tot}} = \underbrace{\gamma T}_{\text{electronic}} + \underbrace{\frac{12\pi^4}{5} R \left(\frac{T}{\Theta_{\mathrm{D}}}\right)^3}_{\text{phononic}} + c_{\mathrm{Z}} \tag{4.15}$$

with the Sommerfeld coefficient γ ($\gamma = 0.729\,\mathrm{mJ/mol\,K^2}$ for bulk gold) and the ideal gas constant $R \approx 8.31\,\mathrm{J/mol\,K}$. The phonon contribution is usually negligibly small at the operating temperatures $T < 100\,\mathrm{mK}$, while the Zeeman contribution c_{Z} needs to be numerically calculated for the specific case, depending on Er ion concentration, temperature and applied magnetic field, as described in A.4. The properties of bulk Au:Er can be described very well by numerical calculations. The thermodynamic properties of thin film Au and Au:Er on the other hand can differ from bulk properties due to defects generated in the production process.

In figure 4.5 the theoretical signal amplitudes per unit energy (dashed lines) are compared to experimental data (dots) for the non-implanted detector (left) and the ion-implanted one (right). It can clearly be seen, that data and simulation do not match. By adding a temperature and magnetic field independent heat capacity the experimental data and the simulations (solid lines) can be matched for both detectors. This discrepancy has been seen in many other detectors. An empirical description of this effect has already been discussed in [Fle09]. The additional heat capacity needed to reproduce the data can be attributed to sputter deposited gold films in the detector. The microscopic origin of this heat capacity is not known, but likely candidates are defects in the material introduced in the deposition process.

The contribution has been found to be larger in the sputtered Au:Er sensor material with values up to $c_{\mathrm{add}} = 10\,\mathrm{J/K\,m^3}$, while in sputtered pure gold films the

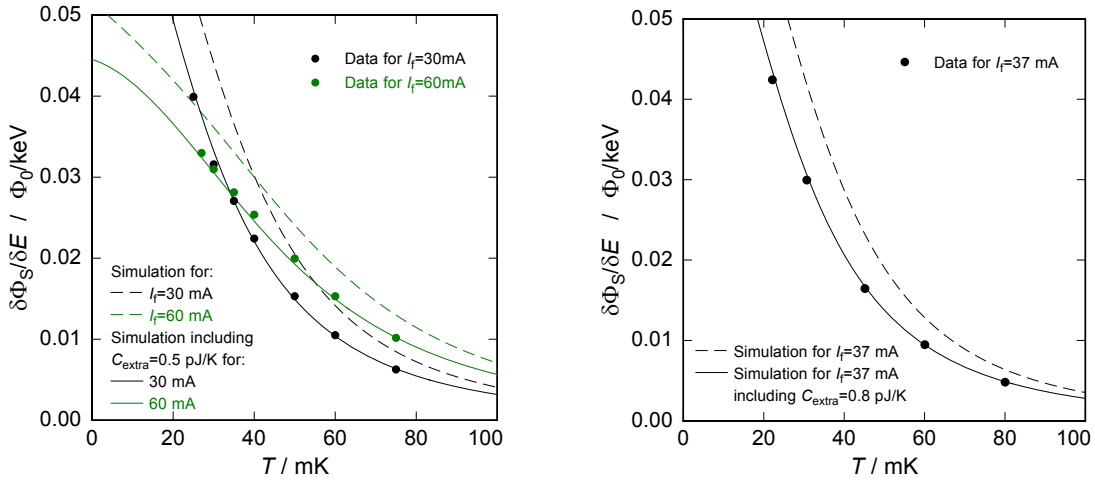

Figure 4.5 The measured normalized signal heights for the non-implanted detector (left) with $I_\mathrm{f} = 30\,\mathrm{mA}$ (black) and $I_\mathrm{f} = 60\,\mathrm{mA}$ (green) and for the ion-implanted detector (right) with $I_\mathrm{f} = 37\,\mathrm{mA}$. Also the expectations from simulation based on the detector geometry are given (dashed lines), but an excess heat capacity needs to be added to properly reproduce the measured data, as discussed in the text.

contribution can be as low as $c_\mathrm{add} = 2\,\mathrm{J/K\,m^3}$. In order to reduce the additional heat capacity in the detectors a technique to electroplate the gold absorbers was developed. This leads to a better structural quality of the film. No technique has been found to decrease the value of the specific heat of the Au:Er sensor to the literature value.

The non-implanted detector shows an additional heat capacity of $C_\mathrm{add} = 0.5\,\mathrm{pJ/K}$. This can be interpreted only as contribution in the sensor, since the absorber, which consists of only the first 5 µm gold layer is electro-deposited. The ion-implanted detector on the other hand shows an additional $C_\mathrm{add} = 0.8\,\mathrm{pJ/K}$ in total. Apart from the $C_\mathrm{add} = 0.5\,\mathrm{pJ/K}$ in the Au:Er sensor an extra $C_\mathrm{add} = 0.3\,\mathrm{pJ/K}$ can be found in the sputter deposited second absorber layer.

Therefore no significant increase of heat capacity can be observed that can be attributed to lattice defects caused by the implantation or to magnetic moments of the implanted ions.

The rise of the pulse shape of an MMCs is ultimately limited by the electron-spin interaction in the sensor material Au:Er, also called the Korringa relation giving a time constant of

$$\tau_0 = (1-\beta)\,\frac{\kappa}{T}\ , \tag{4.16}$$

with the relative heat capacity of the Zeeman-system $\beta = C_\mathrm{Z}/C_\mathrm{tot}$ and the Korringa

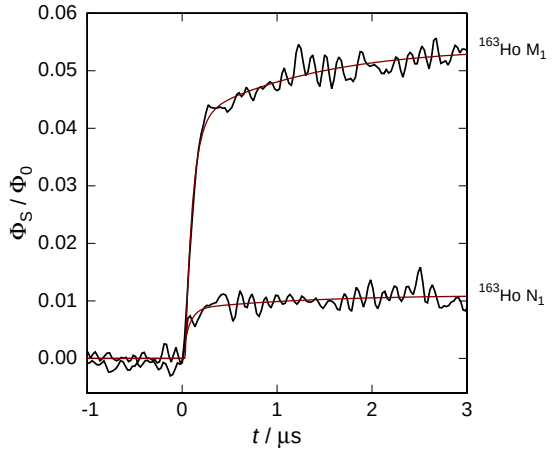

Figure 4.6 First few µs of single events of the M_1- and N_1-lines of the ^{163}Ho electron capture, at $E = 2.040\,\mathrm{keV}$ and $E = 0.411\,\mathrm{keV}$ respectively, showing the signal rise. The rise is fitted (shown in red) with two summed exponential functions. The rise is dominated with a rise time of $\tau_0 = 80\,\mathrm{ns}$, that makes up $\sim 80\,\%$ of the total signal amplitude.

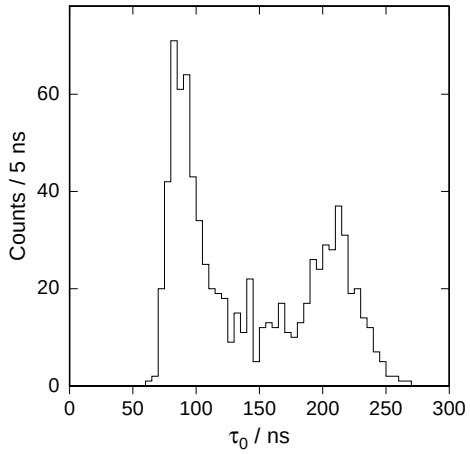

Figure 4.7 Distribution of the dominating rise time τ_0 for the M_1-line of the ^{163}Ho electron capture. While about half of the events show a rise time of $\tau_0 = (90{\pm}12)\,\mathrm{ns}$, that represent the events going down into the first electro-plated absorber layer, the second half shows $\tau_0 = (210 \pm 20)\,\mathrm{ns}$, which represent the events going up into the second sputter-deposited absorber layer.

constant κ. For Au:Er κ was determined in ESR measurements at $T = 1\,\mathrm{K}$ to be $\kappa = 7 \times 10^{-9}\,\mathrm{Ks}$ [Sjø75]. For a usual operation temperature of $T = 30\,\mathrm{mK}$ and with the usual goal of $\beta = 0.5$ this gives $\tau_0 \approx 110\,\mathrm{ns}$. In experiments rise times as low as $\tau_0 = 90\,\mathrm{ns}$ have been observed [Fle09] (see also appendix A.5).

The case of the ion-implanted detector is described in the following. For the usual operating conditions of $T = 30\,\mathrm{mK}$ and $I_\mathrm{f} = 30\,\mathrm{mA}$ the parameters are $C_\mathrm{Z} = 1.14\,\mathrm{pJ/K}$ and $C_e = 1.53\,\mathrm{pJ/K}$, which gives $\beta = 0.43$ and $\tau_0 \approx 130\,\mathrm{ns}$. Rise times as low as $\tau_0 = 80\,\mathrm{ns}$ have been observed and are shown in figure 4.6 for the N_1- and M_1-line of the ^{163}Ho electron capture, at $E = 0.411\,\mathrm{keV}$ and $E = 2.040\,\mathrm{keV}$, respectively. But the rise times are distributed over a wider range, as shown in figure 4.7 for the ^{163}Ho M_1-line. The distribution shows two distinct peaks, one with a faster rise time of $\tau_0 = (90 \pm 12)\,\mathrm{ns}$ and one with a slower and wider distributed rise time of $\tau_0 = (210 \pm 20)\,\mathrm{ns}$. Both peaks show approximately the same number of events.

A possible explanation for the different rise times is the following: The faster rising pulses can be attributed to events going down into the first absorber layer from the implanted source, while the events going up into the sputter deposited second absorber layer show the slower rise. After the ion-implantation took place the source area was directly covered with a thin $d \approx 100\,\mathrm{nm}$ gold layer to enclose the source material. The surface was not cleaned previous to the gold deposition,

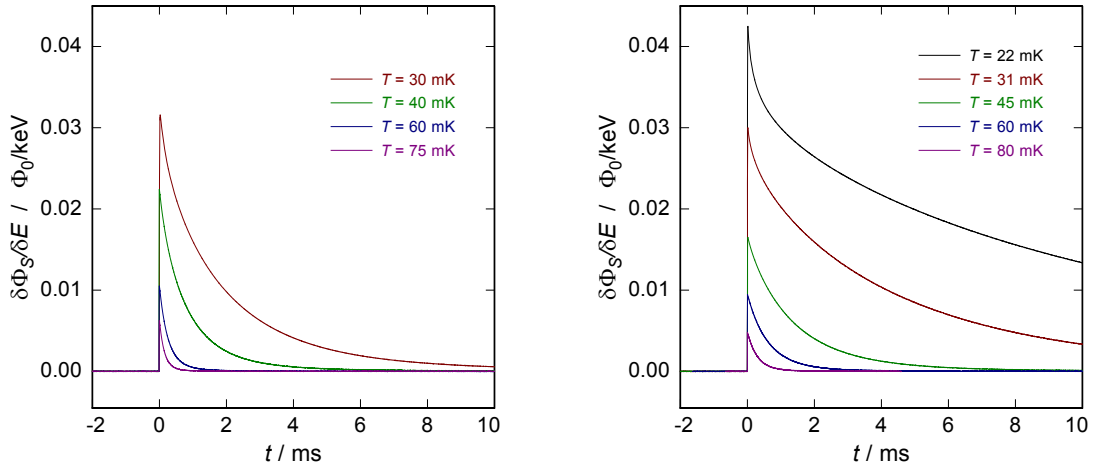

Figure 4.8 The signal shapes normalized in energy for the non-implanted detector with $I_\mathrm{f} = 30\,\mathrm{mA}$ (left) and the ion-implanted one with $I_\mathrm{f} = 37\,\mathrm{mA}$ (right) at several temperatures in the usual operation range below $T < 100\,\mathrm{mK}$. Roughly comparable signals are given in the same color, but due to the different field generating currents, different coupling and differences in fabrication of the two detectors the comparison should be done cautiously.

in order to keep the implanted area unaffected. This might have resulted in bad contact between the lower absorber part and the deposited gold layer. Afterwards the second absorber layer is added with the usual cleaning steps to enable good contact to the newly deposited layer. Therefore the heat deposited in the upper absorber layer might need to diffuse to the border of the absorber, where the top and bottom absorber layer meet with no additional layer in between. The lateral diffusion in sputtered gold layers of the absorber dimensions can take times on the order of $t_\mathrm{d} \approx 100\,\mathrm{ns}$, which matches the observed rise time difference.

Figure 4.8 shows the pulse shape on a milli-second time-scale for the non-implanted detector (left) with a field generating persistent current of $I_\mathrm{f} = 30\,\mathrm{mA}$ and the ion-implanted detector (right) with $I_\mathrm{f} = 37\,\mathrm{mA}$ at several temperatures below $T = 100\,\mathrm{mK}$.

As describe in chapter 3.1, the decay of an event is given by the thermal relaxation time through the weak thermal link G_eb to the thermal bath temperature given by:

$$\tau_1 \approx \frac{C_\mathrm{tot}}{G_\mathrm{eb}} \quad . \tag{4.17}$$

This well describes he general shape of the events shown in figure 4.8. One obvious exception is pulse at $T = 22\,\mathrm{mK}$ in the ion-implanted detector shown in the right plot, that loses approximately 20 % of its signal amplitude in the first $\Delta t \approx 0.5\,\mathrm{ms}$ before going into a much slower relaxation with a decay constant of $\tau \approx 15\,\mathrm{ms}$. This

relaxation is caused by the heat flow into an additional heat capacity caused by the hyperfine splitting of the host gold nuclei due to the crystal field distortions in the vicinity of the embedded Er-ions. This additional decay time can be observed in all MMCs based on Au:Er, and shows a time constant of $\tau \approx 200\,\mu s$ [Ens00] (see also appendix A.5).

The decay time constants of the two detectors differ due to the heat capacity added with the second absorber layer of the implanted detector as well as its weaker thermal link caused by differences in the fabrication of the two detectors, adding up to about a factor of two in the final relaxation time.

4.1.4 Noise

The energy resolution of the detector is defined by the signal-to-noise ratio. Therefore the understanding of the noise plays an important role for optimizing the detector performance. Metallic magnetic calorimeters show a number of intrinsic noise sources that will be summarized in the following.

The most intrinsic one is the thermodynamic energy fluctuation noise. For this issue the detector can be modeled as a canonical ensemble with two distinct subsystems, the electronic system C_e and the Zeeman system C_Z, as shown in figure 4.9. These are connected to each other through a thermal link G_{eZ} while the electronic system is connected to the thermal bath via the thermal link G_{eb}. These two systems will in turn exchange energy between them and with the thermal bath. According to the fluctuation-dissipation theorem, the white power spectral density is given by

$$S_{P_{eb/eZ}} = 4k_B T^2 G_{eb/eZ} \ , \tag{4.18}$$

respectively for eb and eZ.

To calculate the spectral density of the energy fluctuations in the Zeeman-system, which is the measured variable, a set of two coupled differential equations can be

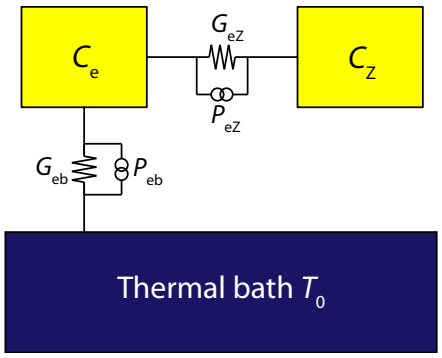

Figure 4.9 Thermodynamic model of a metallic magnetic calorimeter as a canonical ensemble with two subsystems.

solved (for details see e.g. [Fle05]) and transformed into frequency space. Assuming incoherence between the two contributing noise sources, the resulting power spectrum is:

$$S_{\mathrm{E_Z}}(f) = k_{\mathrm{B}} C_{\mathrm{Z}} T^2 \left((1-\beta) \frac{4\tau_0}{1+(2\pi f \tau_0)^2} + \beta \frac{4\tau_1}{1+(2\pi f \tau_1)^2} \right) \ , \tag{4.19}$$

in the relevant cases of $C_{\mathrm{Z}} \simeq C_{\mathrm{e}}$ and $\tau_0 \ll \tau_1$. The integral $\int_0^\infty S_{\mathrm{E_Z}} \mathrm{d}f = k_{\mathrm{B}} C_{\mathrm{Z}} T^2$ corresponds to the energy fluctuations of a canonical ensemble with heat capacity C_{Z} at temperature T, while the frequency evolution is determined by the two time constants $\tau_{0/1}$ of the detector system (see the previous section 4.1.3).

A second noise contribution that is intrinsic to metallic magnetic calorimeters is caused by the erbium ions present in the sensor material. It was empirically determined to show a spectral noise density of

$$S_{\mathrm{Er}}(f) \simeq 0.1 \, \frac{\mu_{\mathrm{B}}^2}{f^\eta} \tag{4.20}$$

per Er ion, with the Bohr magneton μ_{B} and the exponent η of the frequency dependence taking values between $0.8 \ldots 1$. Recent investigations have shown that the noise contribution is caused by the fluctuations in the AC-susceptibility of the sensor material Au:Er [Hof12, Wiß13] (see also appendix A.5.1).

Non-intrinsic but still not avoidable is the read-out noise in the detector system. This is dominated by the flux noise of the front-end SQUID. SQUID noise consists of two independent contributions. A white spectral noise contribution with a typical level for the utilized SQUIDs of $S_\Phi \leq (0.5)^2 \, \mu\Phi_0^2/\mathrm{Hz}$ that corresponds to the fluctuation noise of the shunt resistors in parallel to the Josephson junctions. The second contribution shows a frequency dependency of $S_\Phi \propto f^{-\alpha}$, where α usually takes values around and below 1 and was found for well performing devices to be around $\alpha = 0.6$ [Dru11], but is not well understood. This noise is usually characterized by giving the value at 1 Hz. For the newest SQUID generation the noise level was found to be $S_\Phi(1\,\mathrm{Hz}) \approx (2 \ldots 4)^2 \, \mu\Phi_0^2/\mathrm{Hz}$. The contribution of the room temperature electronics can be suppressed e.g. in a two-stage SQUID setup with a SQUID series array as an amplifier. This read-out scheme was used for the presented measurements and is described in chapter 3.3.2.

Another possible noise contribution is related to random thermal motion of the conduction electrons both in the sensor and the experimental holder. This leads to fluctuating B-fields, which can couple into the detector pick-up coil or into the SQUID loop. Due to the chosen geometries in SQUID and detector, which reduce the magnetic field coupling to small volumes around the coil, these contributions

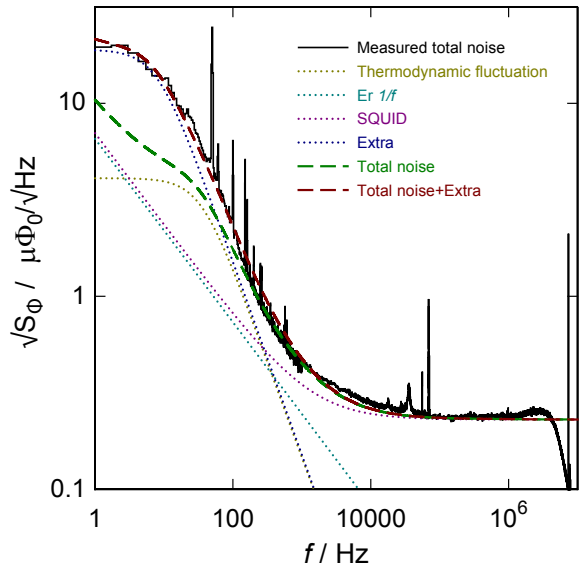

Figure 4.10 The measured flux noise of channel 2 in run 4 of the ion-implanted detector at $T_\mathrm{d} = 29\,\mathrm{mK}$ with $I_\mathrm{f} = 30\,\mathrm{mA}$. The different independent contributions, that are described in the text, are shown in dotted lines as well as the summed predicted noise as a dashed line. To describe the measured spectrum an excess contribution needs to be added, that can be explained by additional temperature fluctuations as reasoned in the text.

were found to be negligibly small and are not considered in the description of the measured noise spectrum.

Figure 4.10 shows the measured $\sqrt{S_\Phi}$ power density from detector channel 2 in run 4. The contributions are calculated with the following settings:

$$\begin{aligned} \sqrt{S}_{\Phi,\ \mathrm{SQ},\ \mathrm{white}} &= 0.23\,\frac{\mu\Phi_0}{\sqrt{\mathrm{Hz}}} \\ \sqrt{S}_{\Phi,\ \mathrm{SQ},\ 1/\mathrm{f}\,(1\,\mathrm{Hz})} &= 7\,\frac{\mu\Phi_0}{\sqrt{\mathrm{Hz}}} \\ \eta \;=\; \alpha &= 0.95\ , \end{aligned}$$

while the other parameters are determined from the numerical simulations considering the adjustments, e.g. the additional heat capacity in sputtered gold films, discussed in the previous sections.

Apart from single peaks due to external noise sources, e.g. the mains hum, the spectrum is very well reproduced by the calculation for higher frequencies $f > 300\,\mathrm{Hz}$ but at lower frequencies the measurement shows excess noise with a plateau of $\sqrt{S_\Phi} \approx 22\,\mu\Phi_0/\sqrt{\mathrm{Hz}}$ and a cut-off frequency of $f_2 \approx 8\,\mathrm{Hz}$. To match the data an additional noise contribution of

$$\sqrt{S}_{\Phi,\ \mathrm{extra}} = 19\,\frac{\mu\Phi_0}{\sqrt{\mathrm{Hz}}} \times \frac{1}{1+\left(\frac{f}{f_2}\right)^2} \tag{4.21}$$

needs to be added incoherently to the calculated spectrum. The origin of this excess noise is not precisely known, but similar effects have been observed earlier in [Sch12, Pie12a] and additional temperature fluctuations of the detector or the whole detector chip could cause this behavior. In the previously reported cases the cut-off corresponded to the thermal decay time of the detector, which in this measurement was determined to $\tau_1 \simeq 4.5\,\mathrm{ms}$. In contrast to this observation the time constant to match the measured spectrum is longer with $\tau_2 = 1/2\pi f_2 \approx 20\,\mathrm{ms}$. Similar decay times have been observed in substrate events, which will be discussed in chapter 4.2.1.

This would mean that the substrate of the chip itself is not perfectly coupled to the thermal bath but the temperature fluctuates with a cut-off time constant of τ_2. From the additional contribution also the amplitude of the temperature fluctuations can be calculated to

$$\sqrt{S}_{T,\,\mathrm{extra}} = \left(\frac{\partial\Phi}{\partial T}\right)^{-1} \sqrt{S}_{\Phi,\,\mathrm{extra}} = 0.8\,\frac{\mu\mathrm{K}}{\sqrt{\mathrm{Hz}}}\ . \tag{4.22}$$

For the origin of the temperature fluctuations two different causes come to mind. First are the implanted sources of the detector-pixels that are not read-out during the measurement. The frequent decays in these sources could easily cause the substrate temperature to fluctuate. Even though the non-operational pixels have been removed prior to run 4, the removal might not have been complete and some residual source material is left on the chip and could cause the temperature fluctuations. Against this hypothesis can be argued that higher energetic decays of this kind should be observable as thermal crosstalk, which will also be discussed in chapter 4.2.1.

The second possible reason is the stability of the SQUID operation. As already discussed in chapter 4.1.2 the SQUIDs significantly heated the detector chip. While the SQUIDs were usually operated in a way, that the detector temperature did not exceed $T_\mathrm{d} = 30\,\mathrm{mK}$, temperatures of $T_\mathrm{d} = 50\,\mathrm{mK}$ were easily reached with different SQUID tuning. With that in mind one can picture that statistical fluctuation of the SQUID tuning can cause temperature fluctuations on this level.

4.1.5 Detector response and energy calibration

In order to extract the detector response function and to precisely calibrate the energy scale of the acquired spectra, an external ^{55}Fe source has been used in the experimental runs 1, 2 and 3.

Detector response

The detector response is extracted from the analysis of the K_α-line of the ^{55}Fe electron capture. The histogram of the K_α-line is fitted with a function given by the convolution of the natural line shape [Höl97] with the function describing the detecor response given by a normalized Gaussian:

$$g(x) = \frac{1}{\sigma\sqrt{2\pi}} \exp\left(-\frac{1}{2}\left(\frac{x-\mu}{\sigma}\right)^2\right) \quad , \tag{4.23}$$

with the expected value μ and the variance $\sigma = \Delta E/2\sqrt{2\ln(2)}$. In some cases a modification is necessary to the Gaussian detector response. This is to describe the effect, that in the energy down-conversion process after an initial energetic particle is stopped, high-energetic, athermal phonons are created, that have a finite probability to travel through the whole detector into the substrate without interacting in the detector after their creation, and are therefore lost for the energy determination. These energy losses, visible as low energetic "tails" in the line-shape, can empirically be described by adding an exponentially modified Gaussian to the Gaussian response:

$$\begin{aligned} g(x) \;=\; & a_\mathrm{g} \frac{1}{\sigma\sqrt{2\pi}} \exp\left(-\frac{1}{2}\left(\frac{x-\mu}{\sigma}\right)^2\right) + \\ & (1-a_\mathrm{g}) \frac{\lambda}{2} \exp\left(\frac{\lambda}{2}\left(2\mu+\lambda\sigma^2+2x\right)\right) \operatorname{erfc}\left(\frac{\mu+\lambda\sigma^2+x}{\sqrt{2}}\right) \quad , \end{aligned} \tag{4.24}$$

with the relative amplitude of the normal Gaussian a_g, the exponential decay rate λ and the complementary error function $\operatorname{erfc}(x) = 1 - \operatorname{erf}(x) = \frac{2}{\sqrt{\pi}} \int_x^\infty \exp(-t^2)\mathrm{d}t$.

Figure 4.11 shows the K_α-line measured with the non-implanted detector (left) as measured at $T = 30\,\mathrm{mK}$ with $I_\mathrm{f} = 30\,\mathrm{mA}$ and the ion-implanted detector (right), also measured at $T = 30\,\mathrm{mK}$ with $I_\mathrm{f} = 30\,\mathrm{mA}$. For the non-implanted detector the exponentially modified Gaussian (equation (4.24)), with $\Delta E_\mathrm{FWHM} = 7.0\,\mathrm{eV}$, was used in the convolution to describe the low energetic tails, while the ion-implanted detector with its twice as thick absorber was sufficiently described by the normal Gaussian (equation (4.23)), with $\Delta E_\mathrm{FWHM} = 7.3\,\mathrm{eV}$. The energy loss problem was cured by the thicker absorbers, limiting the X-ray interaction to the top 5 µm of the absorber. In general to reduce the phonon loss, a reduction of contact area between absorber and sensor layer through the introduction of stems can be used [Sch12]. This approach will be used in the next detector generation for the spectroscopy of the ^{163}Ho electron capture as described in chapter 5.3.1.

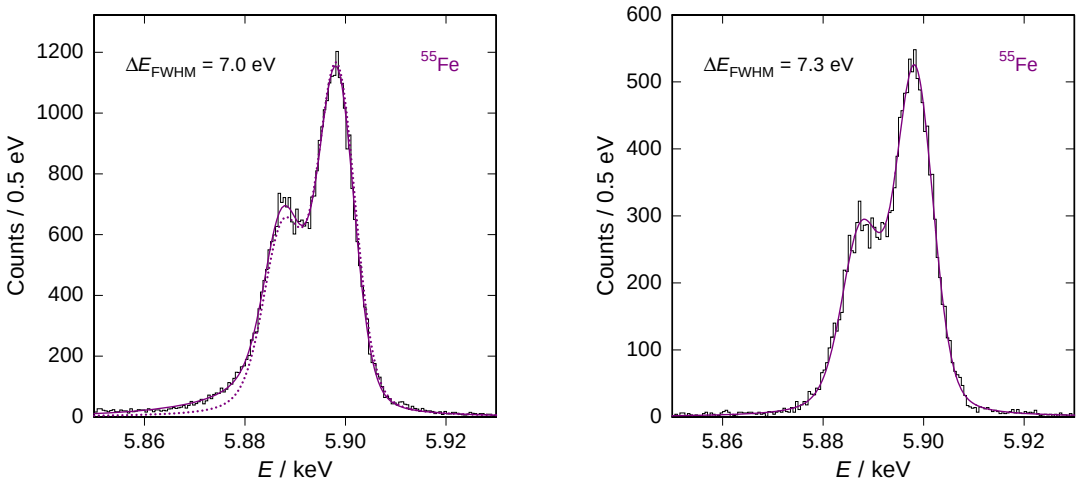

Figure 4.11 The measured K_α-line of the ^{55}Fe electron capture measured with the non-implanted detector (left) and the ion-implanted detector (right). Both spectra were take at $T \approx 30\,\mathrm{mK}$ with $I_\mathrm{f} = 30\,\mathrm{mA}$. The fit (in magenta) is determined by convolving the natural line shape after [Höl97] with eq. (4.24) (left) and with eq. (4.23) (right). In the left plot also the convolution with eq. (4.23) is shown as a dotted line for comparison.

A second way to assess the energy resolution is to use baselines. By using the same optimal filtering algorithm, as described in chapter 3.9, that is normally used for triggered signals, on baselines, the algorithm will assign an amplitude value to the baseline. The resulting distribution around zero energy is the most direct access to the detector response in the limit of small signals, that ideally should not change towards higher energies.

Figure 4.12 shows these baseline spectra for the two detectors acquired in parallel to the ^{55}Fe spectra shown in figure 4.11. Both spectra a well described with a Gaussian after equation (4.23) with $\Delta E_\mathrm{FWHM} = 4.9\,\mathrm{eV}$ for the non-implanted detector and $\Delta E_\mathrm{FWHM} = 6.4\,\mathrm{eV}$ for the ion-implanted one.

Comparing the two results for the non-implanted detector a significant difference between the baseline resolution of $\Delta E_{\mathrm{FWHM,\ base}} = 4.9\,\mathrm{eV}$ and for the K_α of $\Delta E_{\mathrm{FWHM,\ }K_\alpha} = 7.0\,\mathrm{eV}$ can be seen. This discrepancy can be explained by insufficient temperature stability of the cryostat on the seconds to minutes range that influences the amplitude of the energetic signals, since it slightly changes the heat capacity and the magnetization change $\partial M/\partial T$.

The difference for the ion-implanted detector from a baseline resolution of $\Delta E_{\mathrm{FWHM,\ base}} = 6.4\,\mathrm{eV}$ to a resolution in the spectrum of $\Delta E_{\mathrm{FWHM,\ }K_\alpha} = 7.3\,\mathrm{eV}$ shows that the experimental factors were under better control, but still deteriorated the energy resolution by a small amount.

Considering the experimental conditions present during the measurements and

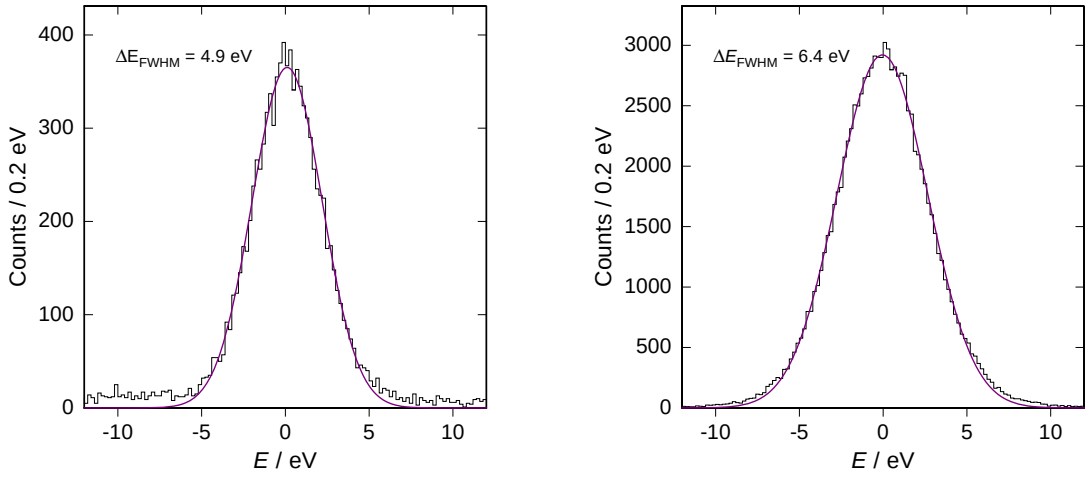

Figure 4.12 The baseline spectra of the non-implanted detector (left) and the ion-implanted one (right). The spectra are both well described by a Gaussian (magenta colored curve) with a half-width of $\Delta E_{\mathrm{FWHM}} = 4.9\,\mathrm{eV}$ for the non-implanted detector, while for the ion-implanted detector a half-width of $\Delta E_{\mathrm{FWHM}} = 6.4\,\mathrm{eV}$ is observed.

including the excess noise and the additional heat capacity discussed in previous sections, the expected energy resolution can be calculated. The expected energy resolution for the non-implanted detector is $\Delta E_{\mathrm{FWHM}} = 4.6\,\mathrm{eV}$ and for the ion-implanted one $\Delta E_{\mathrm{FWHM}} = 6.0\,\mathrm{eV}$, which agree well with the experimentally observed baseline resolutions.

Non-linearity

In order to calibrate the spectrum the K_α- and the K_β-lines as provided from the ^{55}Fe source are used. The observed line positions are not strictly linear compared to their literature values, that are given in [Höl97].

This small non-linear contribution to the signal amplitude is expected because of the temperature dependence of both the heat capacity and the magnetization change of the detector, as first described in [Lin07]. It is also shown there that the energy dependence of the signal amplitude can be very well described by a polynomial of second order:

$$\delta\Phi \simeq \frac{\partial\Phi}{\partial E}\delta E + \frac{\partial^2\Phi}{\partial E^2}\delta E^2 \ . \tag{4.25}$$

The result of the non-linearity analysis is shown in figure 4.13. It shows the literature values of the energy on the abscissa compared to the measured signal amplitude (left), respectively the experimentally observed energy (right), on the

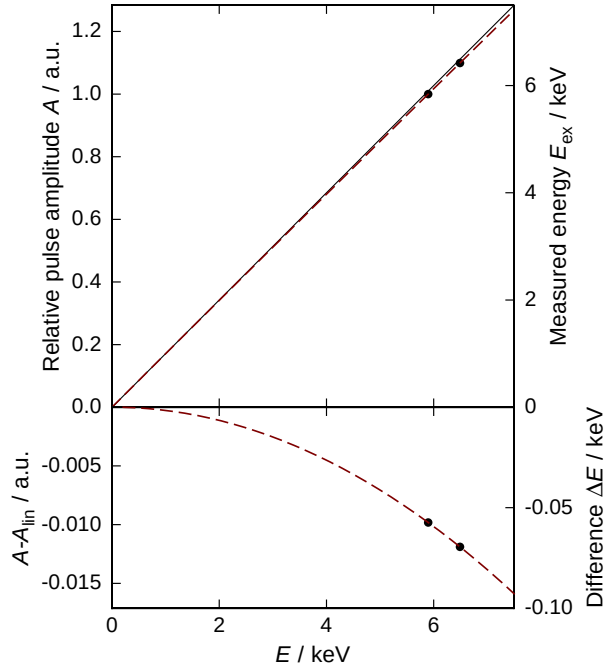

Figure 4.13 The relative signal amplitude of the K_α- and K_β-lines of the ^{55}Fe electron capture plotted against their literature energy values. A little quadratic deviation from a linear detector behavior (indicated by the black line) can be seen and is shown in the lower part of the plot. In the energy range of the ^{163}Ho electron capture spectrum below $E < 3\,\mathrm{keV}$ the non-linearity contribution is less than $\Delta A < 0.5\,\%$.

ordinate. A small deviation of the fitted red curve from a perfectly linear behavior, shown in the black straight line, can be observed. The deviation from the linear behavior is shown in the lower part of figure 4.13 and is roughly $\Delta A = 1\,\%$ around the calibration data at $E = 6\,\mathrm{keV}$ and in the interesting region for the ^{163}Ho electron capture spectroscopy below $E < 3\,\mathrm{keV}$ even smaller than $\Delta A = 0.5\,\%$. By knowing this behavior and an analytical description, the non-linearity contribution can easily be corrected using the inverse function of eq. (4.25).

Long time stability

The last aspect concerning the detector behavior is the stability of the performance during the measuring time. For an experiment for neutrino mass determination it is necessary to run continuously for months up to several years to collect the required statistics. Therefore it is beneficial if the detector system can run for long periods of time without changing its performance or the need of extensive maintenance.

Channel 2 in run 3 will therefore be exemplarily analyzed under this aspect. The total acquisition time was about $t_{\mathrm{acq}} = 850\,\mathrm{h}$ ($\approx 35\,\mathrm{days}$) over the course of 45 days. The dead time of the experiment was mainly due to failure of the data acquisition system and cryostat maintenance. Of the $t_{\mathrm{acq}} = 850\,\mathrm{h}$ approximately $t_{\mathrm{lost}} = 90\,\mathrm{h}$ of data were discarded because of worse than average detector performance. The remaining $t^*_{\mathrm{acq}} = 760\,\mathrm{h}$ correspond to 18 single spectra with varying durations between $t_{\mathrm{spec}} = 10 \ldots 100\,\mathrm{h}$.

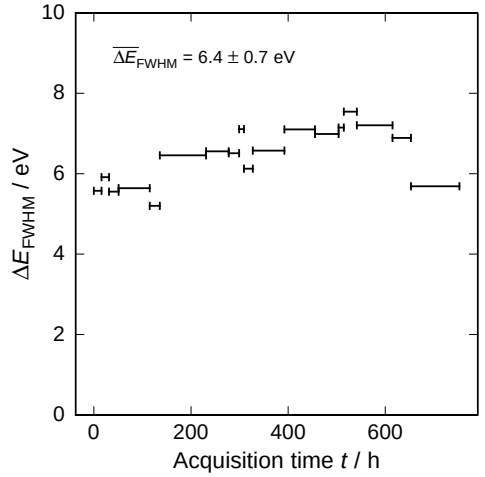

Figure 4.14 The duration of the 18 individual spectrum measurements of channel 2 in run 3 plotted against the baseline resolution. The average resolution, weighted by the duration of the measurement, of $\overline{\Delta E}_{\mathrm{FWHM,\ base}} = (6.4 \pm 0.7)\,\mathrm{eV}$ is also quoted and agrees very well with the combined baseline spectrum that is shown in figure 4.12 and shows a resolution of $\Delta E_{\mathrm{FWHM,\ base}} = 6.4\,\mathrm{eV}$.

To monitor the detector performance the baseline resolution was used. Figure 4.14 shows the baseline resolution of the 18 single spectra with their individual acquisition time given by the width of the shown bar. The average, weighted by acquisition time, of

$$\overline{\Delta E}_{\mathrm{FWHM,\ base}} = (6.4 \pm 0.7)\,\mathrm{eV} \quad , \tag{4.26}$$

is still varying, but well within the $\Delta E_{\mathrm{FWHM}} \leq 10\,\mathrm{eV}$, a limit set by statistical analyses of the ^{163}Ho electron capture spectrum (see chapter 2.4.4).

The efficiency of this measurement with about 2/3 of the time used for data acquisition and 1/3 of time for maintenance or acquisition of eventually discarded data can certainly be improved upon. Possible improvements include a dry dilution cryostat, a data acquisition system optimized for these long measurement campaigns and a "cleaner" environment, allowing long measurements without external disturbances, that can for example create excess noise.

4.2 Spectrum analysis

4.2.1 Single channel spectrum extraction

All rare event searches, like $0\nu\beta\beta$-experiments and dark matter searches, as well as neutrino mass experiments require a perfect understanding of the background sources to understand their data well and to not accidentally interpret a background signal as true signal. While this is also true for the neutrino mass searches with ^{163}Ho, the presented measurements also suffer from additional thermal signals that are created outside of the detectors and need to be discriminated from the "real"

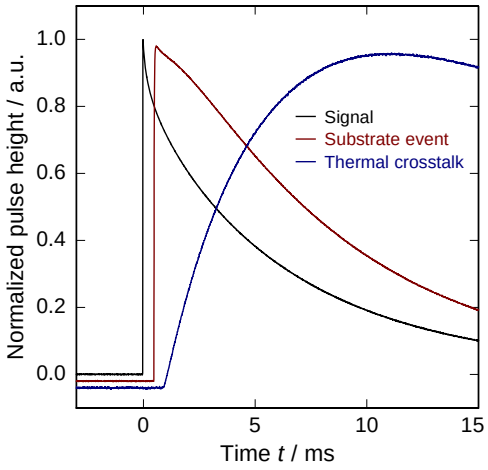

Figure 4.15 Exemplary events of the three types that can be observed in the spectrum measurements at $T_\mathrm{d} \approx 30\,\mathrm{mK}$ with $I_\mathrm{f} = 30\,\mathrm{mA}$ with normalized amplitudes. The different types are events directly happening in the read-out detector (black), events absorbed in the solid silicon substrate (red) and the thermal crosstalk from an event that happened in a neighboring detector (blue).

signals.

The different events can be roughly divided into three categories with exemplary events shown in figure 4.15. The event types are described in the following for the usual conditions of longer spectrum acquisitions, namely a field generating persistent current of $I_\mathrm{f} = 30\,\mathrm{mA}$ and a detector temperature of $T_\mathrm{d} \approx 30\,\mathrm{mK}$.

The events that are directly absorbed in the detector have a rise time around $\tau_0 \approx 100\,\mathrm{ns}$ and a thermal relaxation with $\tau_1 \approx 5\,\mathrm{ms}$ as already described in chapter 4.1.3. In figure 4.15 these events are indicated with a black line.

The second type of events is most likely due to particles, which interact in the solid Si substrate. These events also show a quite fast rise time with $\tau_0 \approx 10\,\mu\mathrm{s}$ with a second rise with $\tau \sim 1\,\mathrm{ms}$ that creates the "bump" visible in the "substrate event" shown in figure 4.15 in red. The fast rise can be caused by athermal phonons, while the second rise is created by thermal phonons. The decay of the substrate events is partly with the same decay time as for the direct signals ($\tau \approx 5\,\mathrm{ms}$), but they show a major contribution of a longer relaxation time (larger than $\tau > 10\,\mathrm{ms}$), corresponding to the relaxation time causing the cut-off of the excess noise as described in chapter 4.1.4.

The third event type is created if an event is absorbed in a neighboring detector and while relaxing back to equilibrium some of the energy flows through the solid substrate to the observed detector and creates a signal there. They show an amplitude on the order of 1 % of the event in the original detector, a rise time in the millisecond range and a decay time comparable to the long relaxation time of the substrate events ($\tau > 10\,\mathrm{ms}$).

While the difference between the event types in figure 4.15 is obvious to the naked eye, this might get more difficult for small amplitudes that are comparable

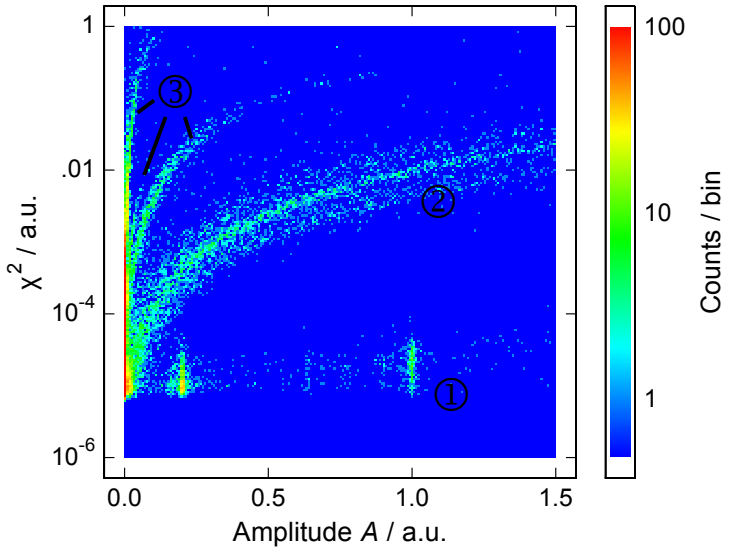

Figure 4.16 The density plot shows the amplitude plotted against the χ^2-value of the events, while the color shows the number of events for the amplitude-χ^2 combination. The direct events can be found below $\chi^2 < 10^{-4}$ indicated with ①, while the substrate events ② and thermal crosstalk ③ events show larger χ^2-values. The substrate events show a broad band, while the thermal crosstalk events are subdivided into three families. Only in the region of the amplitude $A < 0.1$ the discrimination between the different types fails based on the χ^2-value.

to the noise level. On the other hand one would like to have an objective way to distinguish between them to automize the process. An established way to approach this problem for temporally discretized signals with n samples is by using the χ^2-test. The test calculates the sum over the mean square deviation from each signal sample O_i to the discretized detector response p_i stretched by the amplitude A of the signal:

$$\chi^2 = \sum_{i=0}^{n} \frac{(O_i - A\,p_i)^2}{A\,p_i} \quad . \tag{4.27}$$

The detector response is normally obtained from the average over a large number of events from one mono-energetic spectral line. For figure 4.16 the events that are associated with the M_1-line of the ^{163}Ho electron capture were used as average. These events can be found around $A = 1$ with $\chi^2 < 10^{-4}$ in the density plot of the obtained χ^2-values plotted against the signal amplitudes.

In figure 4.16 the direct events in the detector can be found with values of $\chi^2 < 10^{-4}$. At larger amplitudes this simple criterion seems very reliable, while for amplitudes below $A < 0.1$ the other event types are interfering and no reliable

discrimination is possible any more. Other properties of the events, e.g. the event area or the rise time, can be used to refine this cut, but the low amplitude threshold is not much improved. Therefore the data below the threshold $A < 0.1 \approx 0.2\,\mathrm{keV}$ is discarded and no lower energetic events can be measured by using this technique, that relies on the data of a single detector channel.

4.2.2 Spectrum combination

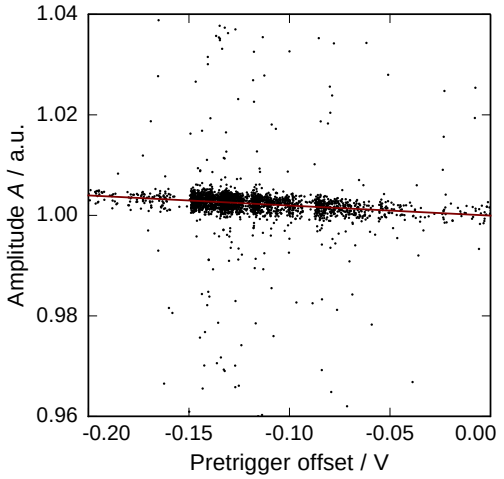

Figure 4.17 The pre-trigger offset, that is temperature sensitive because of the magnetization change of the Au:Er sensor material, plotted against the signal amplitude value of the ^{55}Fe K_α-line of a single spectrum measurement of channel 2 in run 3. A linear fit through the data, that is shown by the red solid line, is used to correct the amplitude values for the temperature dependence.

As already described in chapter 4.1.5 the "high statistics" spectra are combined data from several individual measurements. The procedure to combine the spectra will be explained in the following.

Each individual spectrum is first fitted with its own average from the events associated with the K_α-line of the ^{55}Fe calibration source or, if no ^{55}Fe source was used, the M_1-line of the ^{163}Ho electron capture. The cut described in chapter 4.2.1 is applied. The amplitude of the pulse is rescaled taking into account a possible temperature drift using the recorded pre-trigger samples (see chapter 3.8). For the small temperature changes occurring during a measurement, the signal amplitude can be approximated as linearly dependent on temperature as shown in figure 4.17 and corrected to a constant level.

Afterwards each spectrum is energy calibrated as described in chapter 4.1.5. In experiments having the external ^{55}Fe source the K_α- and K_β-lines are used. If no ^{55}Fe source was used the spectrum is calibrated using the L-lines from the ^{144}Pm electron capture and the M-lines from the ^{163}Ho electron capture. In this case the energy values, which are used for the calibration are the ones obtained by the analysis of the spectrum calibrated with the ^{55}Fe source. These energy values are shown in table 4.2.

4.2.3 Data analysis for run 3

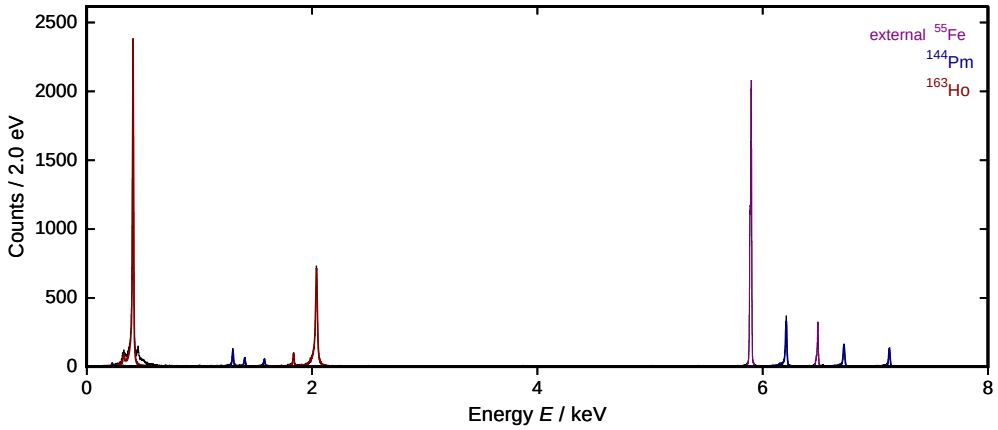

Figure 4.18 The combined spectrum measured with channel 2 and 4 in run 3 in the energy range $0\,\text{keV} < E < 8\,\text{keV}$. The spectrum includes the K_α- and K_β-lines (magenta) from the external ^{55}Fe calibration source, the spectrum that results from the electron capture of ^{144}Pm (blue) and the electron capture spectrum of ^{163}Ho (red).

The spectrum measured in run 3 is shown in figure 4.18. Structures due to three different nuclides can be found in the spectrum. First, fitted in magenta, are the calibration peaks from the ^{55}Fe source with one line at $E = 5.9\,\text{keV}$ and one at $E = 6.5\,\text{keV}$. Fitted in blue, are the peaks from the electron capture of ^{144}Pm decaying to ^{144}Nd. As already discussed in chapter 3.5.1 the ^{144}Pm was ion-implanted together with ^{163}Ho in the form of $^{144}\text{Pm}^{19}\text{F}^+$. In this energy range the ^{144}Pm decay spectrum shows three groups with three lines each, the L-lines ($L_1,\ L_2,\ L_3$) around 7 keV, the M-lines ($M_1,\ M_2,\ M_3$) around 1.5 keV and the N-lines ($N_1,\ N_2,\ N_3$) around 0.3 keV. The N-lines are not visible in figure 4.18, because of their small amplitudes. Additionally the K-line of the spectrum around 40 keV was also observed. The ^{144}Pm decay spectrum will be discussed in the following section 4.2.4. The third nuclide contributing to the spectrum is ^{163}Ho with its electron capture spectrum fitted in red.

In the following the different contributions of the measured spectrum will be referred to by the name of the mother atom, namely ^{55}Fe, ^{144}Pm and ^{163}Ho.

Table 4.2 shows the experimentally observed line positions of the ^{144}Pm and the ^{163}Ho decay spectra as obtained from the ^{55}Fe calibrated spectra compared to the electron binding energies of the associated electron levels of the daughter nuclides. All lines are observed at slightly lower energies compared to the binding energies. This is due to the fact that the electron shell after the electron capture has still the same structure as the shell of the mother atom without the captured electron and needs to relax not only to the ground state, but also to the electron

Element	Line	E_{lit} [keV]	E_{exp} [keV]
^{163}Ho	M_1	2.0469	2.040
^{163}Ho	M_2	1.8446	1.836
^{163}Ho	N_1	0.4204	0.411
^{163}Ho	N_2	0.3406	0.329
^{144}Pm	L_1	7.1302	7.125
^{144}Pm	L_2	6.7271	6.721
^{144}Pm	L_3	6.2139	6.208
^{144}Pm	M_1	1.5815	1.576
^{144}Pm	M_2	1.4068	1.402
^{144}Pm	M_3	1.3017	1.297

Table 4.2 The energies of the spectral lines observed in the spectrum as measured in channel 2 of run 3 obtained after calibrating the energy scale with the K_α and K_β-lines from the ^{55}Fe source. The observed values are compared to the binding energies of the captured e^- in the daughter atom as determined in [Des03].

shell configuration of the daughter atom. For the X-rays of the radiative $M_1O_{2,3}$ transition this interaction energy shift has been found to be $\Delta E = 19\,\text{eV}$, which is also in agreement with theoretical expectations [Spr85].

A precise description how the shell relaxation mechanism shifts the de-excitation energy has to be calculated. The discussed measurement provides accurate values for the middle energy of each peak. On the other hand, the measured de-excitation energies might also be affected by solid state effects due to the embedding of the ^{163}Ho nucleus in gold. Both these aspects will be investigated in future within the ECHo experiment (see chapter 5).

4.2.4 Analysis of the ^{144}Pm electron capture spectrum

$^{144}_{61}$Pm decays via electron capture or β^+-decay into $^{144}_{60}$Nd with a half-life of $T_{1/2} = 360\,\text{d}$ and an end-point of $Q_{\text{EC}} = 2331.7\,\text{keV}$ [Tul89]. The emitted γ-rays with energies larger than $E > 300\,\text{keV}$ are generally too high energetic to be stopped in the detector and the resulting signals are too large to be resolved in the measurements. The de-excitations following an electron capture on the other hand can be stopped with a finite probability.

The observable energies for a capture from the corresponding electron shell are given in table 4.3. The electron capture has the highest probability to be from the $1s$ electron (the K-level). For the K-line, the radiative de-excitations dominate, while electronic transitions only account for approximately 8 %. In the radiative transitions photons of an energy around $E \approx 40\,\text{keV}$ are emitted, which have a probability of about $p = 25\,\%$ to be stopped in the absorber. The exact energy values and absorption probabilities are also given in table 4.3. Auger-electrons and the de-excitations of captures from higher levels can be detected with a probability close to $p = 100\,\%$.

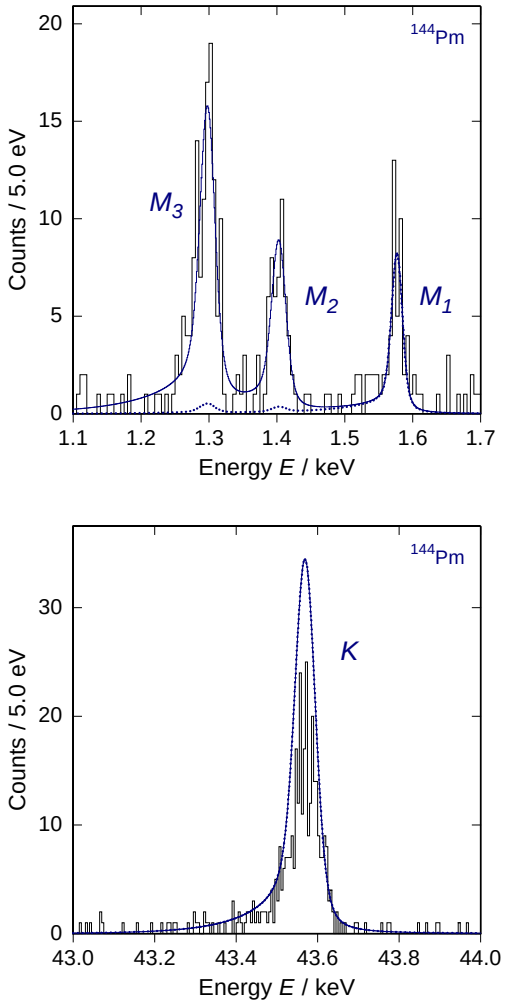

Figure 4.19 Sections of the spectrum measured in run 1 showing the spectrum contributions of ^{144}Pm. The three M-lines (top left), the three L-lines (top right) and the K-line (bottom left). Fits are shown in all plots, namely the expected line shape and amplitudes without (dotted line) and with (solid line) enhancement from the K-shell transitions as explained in the text.

After an electron from a shell, e.g. the K-shell, is captured the created hole will be filled from a lower energetic shell, e.g. the L_2-shell, under emission of an X-ray or an Auger-electron. Following this initial step the new hole is filled again from a lower energetic shell until the atom is entirely de-excited and brought to its ground state. The life-time of the single intermediate steps is on the order of $\tau \sim 10^{-16}\,\mathrm{s}$, therefore the whole cascade will appear as a single event in an MMC with a response time on the order of $\tau_0 \approx 10^{-7}\,\mathrm{s}$.

The data discussed here was measured in run 1 because of the largest specific activity from ^{144}Pm with the K-line included in the measurement. Figure 4.19 shows the sections of the measured spectrum showing the M-lines (top left), the L-lines (top right) and the K-line (bottom left). Each line has been fitted (dashed blue line) using the electron capture spectral shape after eq. (2.30) convolved with an exponentially modified Gaussian (eq. (4.24)). Due to the stopping power of the absorber only the amplitude of the K-line is reduced.

X-ray	$E_{\mathrm{X-ray}}$ / keV	Level	E_{lvl} / keV	p_{t} / %	p_{a} / %	n_{theo}	n_{exp}
		K	43.575			505	264
		L_1	7.130			202	202
$K_{\alpha 2}$	36.848	L_2	6.727	26.4	29.4	302	207
$K_{\alpha 1}$	37.361	L_3	6.214	48.1	28.6	557	418
		M_1	1.582			43	50
$K_{\beta 3}$	42.169	M_2	1.407	4.63	22.3	59	57
$K_{\beta 1}$	42.274	M_3	1.302	8.95	22.2	114	128

Table 4.3 The X-ray transition probabilities from a vacancy in the K-shell of Nd. The table shows the X-ray's name in the Siegbahn-notation, the X-ray's energy [Des03], the transition level in X-ray notation with the level's energy [Des03]. Also given is the transition probability p_{t} from the K-shell [Chu99] and the absorption probability p_{a} of the X-ray, as determined by a Monte-Carlo simulation of the possible track length in the detector combined with the X-ray attenuation [Hub04]. The last two columns show the calculated and the observed number of events, normalized to the L_1-line.

Since part of the energy of the de-excitation of the K-line is not stopped in the absorber for about 75 % of the K-captures, the detector only sees a fraction of energy corresponding to the de-excitation of the level from which the e^- filled the hole in the K-shell. For these levels, the absorption of energy in the detector will be close to $p = 100\,\%$. Due to angular momentum conservation, only transitions to states with an orbital quantum number larger than $l \geq 1$ ($L_2,\ L_3,\ M_2,\ M_3 \ldots$) are allowed. Therefore the observed number of counts in these levels are enhanced by the not complete detection of the de-excitation energy of the K-shell.

Including this enhancement effect from the K-shell transitions leads to the second calculation shown in figure 4.19 (solid blue line). As can be seen this description works well to reproduce the observed ^{144}Pm spectrum at the M-lines, while the L_2- and L_3-, as well as the K-line are slightly overestimated. A closer look, especially by comparing the observed and the expected counts, which are normalized to the L_1-line and are also given in table 4.3, confirms the before mentioned deviations.

Two possible explanations for the deviations were found. First of all the simulations to determine the absorption probability do not consider physical effects like Compton scattering of the initial K X-rays. A Compton scattered photon would deposit only a part of its energy, which is then combined with the energy of the following de-excitation cascade. Therefore the event would show some intermediate energy and does not contribute to one of the spectral lines. This would decrease both the observed amplitude of the K-line, as well as the amplitude of the enhancement effect. This can be cleared up by a dedicated simulation, that considers the particle interactions in the absorber.

Secondly, there is a technical issue with the detection of the de-excitation from a K-capture. Since these events are about seven times larger than the events, the detector is optimized for, the read-out electronics can not reliably trigger and record all events in this energy range. Therefore not all events contributing to the K-line would be identified as such, which leads to a decrease of the K-line's amplitude. This issue can be fixed by optimizing the detector design and the electronics performance. This was not attempted, since the ^{144}Pm is actually an undesired impurity in the embedded source and the understanding of the ^{144}Pm spectrum came as a by-product of the presented measurements on the ^{163}Ho electron capture.

4.2.5 Analysis of the ^{163}Ho electron capture spectrum

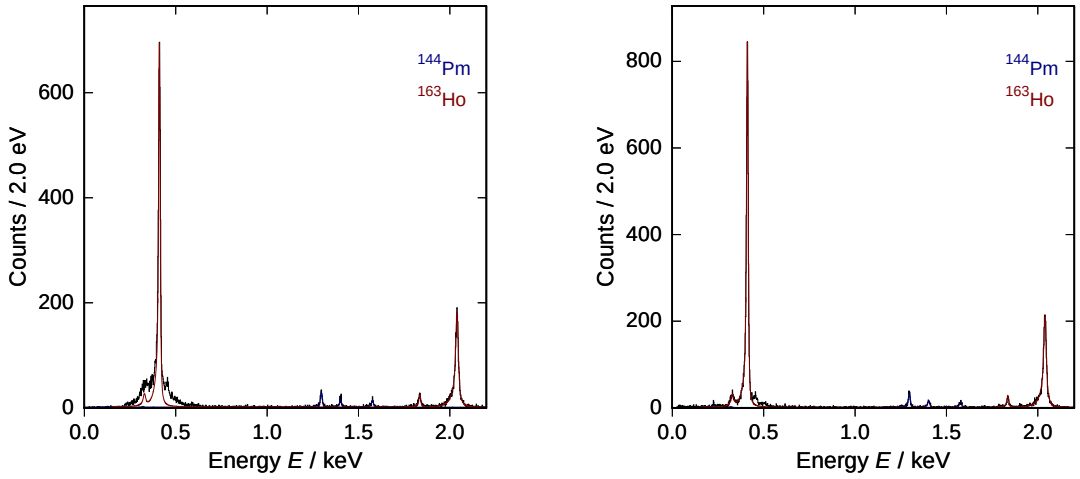

Figure 4.20 The spectra measured in run 3 with channel 2 (left) and channel 4 (right) showing the section most interesting for the ^{163}Ho electron capture spectrum below $E < 2.2\,\mathrm{keV}$. The fitted spectral shapes for the ^{163}Dy (red) and the ^{144}Nd (blue) are also shown. The spectrum in channel 2 (left) is contaminated around the N_1-line due to the opening to the environment or the presence of the ^{55}Fe source.

The analysis of the ^{163}Ho electron capture spectrum is divided into two different parts corresponding to the spectra measured in run 3 and run 4. The analysis of run 3 and run 4 are presented separately due to the different experimental conditions and the different outcome. Run 3 used an ^{55}Fe source for external calibration to determine the properties of the spectral lines in the spectrum. The calibration has already been described in chapter 4.1.5.

The first observation was that the activity in channel 2 was about twice as large as the one in channel 4. This can be explained by the Gaussian profile of the ion-beam during the implantation and the exact focus point on the detector. If the

Parameter	Value	Error	Expected value	Varied?
$m^2(\nu_e)$	0			no
$\varphi^2_{\mathrm{H}}(0)$	tab. 2.2			no
B_{H}	tab. 2.2			no
ΔE_{FWHM}	7.3 eV			no
E_{M_1}	2039.9 eV	0.1 eV	2046.9 eV	yes
E_{M_2}	1836.2 eV	0.2 eV	1844.6 eV	yes
Γ_{M_1}	13.4 eV	0.1 eV	13.2 eV	yes
Γ_{M_2}	4.8 eV	0.4 eV	6.0 eV	yes
m_{g}	$-0.0156\,\mathrm{keV}^{-1}$	$0.0006\,\mathrm{keV}^{-1}$		yes
n_{g}	0.903	0.003		yes
$m_{1/\lambda}$	$0.00173\,\mathrm{keV}^{-1}$	$9 \times 10^{-5}\,\mathrm{keV}^{-1}$		yes
$n_{1/\lambda}$	0.0168	0.0003		yes

Table 4.4 The parameters going into the fit or that are extracted from the fit to the spectral shape of the ^{163}Ho spectrum for run 3.

beam focus was a little off center the detectors further away from the focus can easily be implanted with less ions.

Figure 4.20 shows the ^{163}Ho electron capture spectrum as measured in run 3 by channel 2 (left) and channel 4 (right). For channel 2 only a part of the recorded data is shown since the channel suffered from an inconsistent trigger efficiency with the consequence that only about half of the recorded data showed the whole spectrum down to low energies, including the N_1- and N_2-lines.

Also shown in figure 4.20 is a fit to the ^{163}Ho spectrum after equation (2.30) that was convolved with an exponentially modified Gaussian after equation (4.24). For the fit the following parameters were fixed:

- The average electron neutrino mass was assumed to be zero $m^2(\nu_e) = 0\,\mathrm{eV}$,
- the electron wave functions at the nucleus $\varphi^2_{\mathrm{H}}(0)$ and the exchange and overlap corrections B_{H} were used as given in table 2.2 and
- the energy resolution of $\Delta E_{\mathrm{FWHM}} = 7.3\,\mathrm{eV}$ was used, as determined from the K_α-line from the external ^{55}Fe source as shown in figure 4.11.

The following parameters were left free within the fit:

- The central line energies E_{H} that are compared to the binding energies of the corresponding electron of the daughter atom ^{163}Dy [Des03],

- the Lorentzian line widths Γ_{H}, that are compared to the literature values [Cam01],
- the end-point energy Q_{EC}
- the relative amplitude of the pure Gaussian in the exponentially modified Gaussian (eq. (4.24)) was assumed to be linearly dependent on the energy $a_{\mathrm{g}}(E) = m_{\mathrm{g}}\,E + n_{\mathrm{g}}$ as well as
- the exponential decay rate $1/\lambda(E) = m_{1/\lambda}\,E + n_{1/\lambda}$.

With this fit the measured spectrum is described very well. Only around the N_1-line two additional structures can be found. First an additional structure at an energy of $E \approx 450\,\mathrm{eV}$ can be found in both channels. These additional events can also be found in the spectrum published in [Gat97] that is reproduced in figure 2.3. Unfortunately no consistent explanation for this structure has been found and requires further investigation.

The second inconsistency is the badly matching fit in figure 4.20 (left) around the N_1- and N_2-lines, where additional events can be found, that are only present in channel 2. The absence of these counts in channel 4 leads to the conclusion that these counts are caused either by the ^{55}Fe calibration source or generally by the opening in the shielding to the environment, that allowed the X-rays from the external source, and possibly other energetic particles, to reach the detector.

The parameters of the fit to the whole data recorded in channel 2 can be found in table 4.4. The data of channel 4 is not used because the fixed energy resolution $\Delta E_{\mathrm{FWHM}} = 7.3\,\mathrm{eV}$ in the fit plays an important role in order to determine the line width Γ_{H}. The energy resolution is determined from the K_α-line of the ^{55}Fe calibration source, which channel 4 was not exposed to.

Also the parameters from the N_1- and N_2-lines are left out because of the additional events in the same energy range and the trigger efficiency issues mentioned earlier. Therefore also the Q_{EC}-value is left out since the strongest tool for its determination is the measured relative amplitude of N- to M-lines.

The energies of the lines E_{H} and the fact that they are slightly lower energetic than the expectation from the electron binding energies has already been discussed at the end of chapter 4.2.3.

The widths Γ_{H}, on the other hand, agree quite well with the literature values within the available accuracy. Even though the presented measurements are the ones with the best resolution on the electron capture spectrum of ^{163}Ho up to this point, the instrumental width (energy resolution) is only comparable to the natural line widths. Therefore the sensitivity on the line widths is somewhat limited and is even more reduced by the low-energetic tails. For an accurate determination, a

detector with an energy resolution on the order of $\Delta E_{\mathrm{FWHM}} \approx 2\,\mathrm{eV}$ with strongly reduced athermal phonon loss (low-energetic tails) seems therefore necessary.

4.2.6 Improvements and further analysis

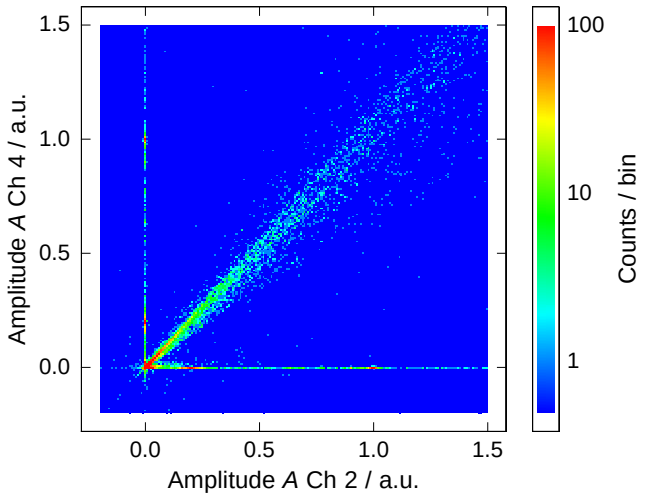

Figure 4.21 The amplitude determined in one detector channel potted against the amplitude simultaneously determined in the second channel. The anti-coincident signals with $A = 0$ on the opposing channel are the "true" signals in the detector and show the desired spectrum. The coincident signals around to the diagonal background events (see chapter 4.2.1) and are therefore omitted.

As already briefly described in the beginning of chapter 4 the goal of run 4 was to lower the background and lower the low energy threshold of the measurement. By removing the two non-functional detectors, not employing a calibration source and closing off the shielding, the potential sources for external background were reduced. By far the largest impact was created by the simultaneous and synchronized measurement of two detectors.

Another property of the different pulse types, that has not already been discussed in chapter 4.2.1, is their signature in a second neighboring detector. Both substrate events and thermal crosstalk events are transmitted through the common silicon substrate and therefore show very similar pulse shapes and amplitudes in both detectors and therefore show coincident signals in both channels. Events happening in one detector will be seen as thermal crosstalk in the other detector with very slow rise times, and a much lower amplitude on the order of $A_{\mathrm{rel}} \leq 1\,\%$. For the interesting energy range below $E < 3\,\mathrm{keV}$ the thermal crosstalk events can not be distinguished from the usual noise level. Therefore for each channel, events happening in the corresponding detector can be distinguished from background by pulse shape and by anti-coincidence with the signal in the other channel.

To use this method for event discrimination, a new data acquisitions system was developed. The new system, equipped with a 4-channel Razor CompuScope 14X2

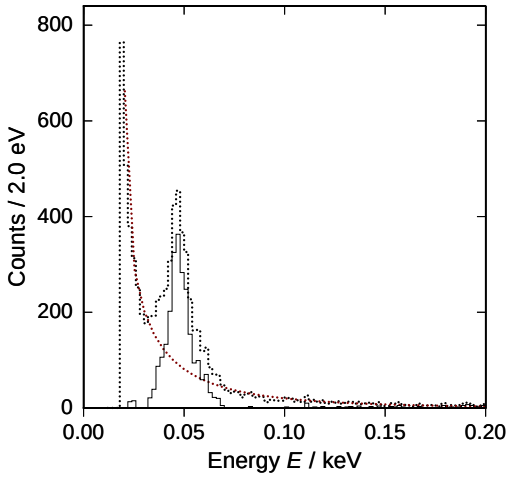

Figure 4.22 The low energy part of the measured spectrum after cuts (dotted black histogram) shows additional background. The cutoff at $E \approx 20\,\mathrm{eV}$ is an artificial cutoff set in the analysis. To be able to analyze the spectrum in this energy range a smooth background (dotted red line) is assumed and subtracted from the data resulting in the shown spectrum (full black histogram).

CSE1442 digitizer card[3], allowed the synchronized recording of two detector signals with a dedicated trigger channel for each detector. Figure 4.21 shows the amplitude of the signal in channel 2 plotted versus the amplitude of events in channel 4. The events showing amplitude $A = 0$ in one of the two channels are events occurring in the other channel. These events can be found in two regions. One is along the abscissa, corresponding to events in channel 2, the second on along the ordinate, corresponding to events in channel 4. The events along the diagonal combines substrate and crosstalk events that show very strong correlation between the two channels and are therefore easily discriminated from the events in the detectors down to amplitudes of $A \approx 0.02$ or energies of $E \approx 40\,\mathrm{eV}$. By using the previously described cuts on χ^2 and area, the efficiency is once again slightly improved.

Within run 4 a spectrum with about 20 000 events in the ^{163}Ho electron capture spectrum was measured in about 500 h (≈ 21 days) over the course of 44 days with two detector channels. Even though the acquisition to maintenance time was even worse than in run 3, the detector performance was more stable and slightly better than in run 3. The average baseline energy resolution of channel 2 was $\overline{\Delta E}_{\mathrm{FWHM,\ base}} = 5.6 \pm 0.5\,\mathrm{eV}$ and for channel 4 it was $\overline{\Delta E}_{\mathrm{FWHM,\ base}} = 5.2 \pm 0.4\,\mathrm{eV}$. The shielding was entirely closed off and no external calibration source was used in this measurement, solely relying on the self-calibration capability of the ^{163}Ho spectrum.

Unfortunately the spectrum was not entirely background-free at very low energies. This is most likely due to the thermal crosstalk events of the spectral lines, that show up in this low energy region and can not be perfectly separated. A smooth background was assumed and subtracted from the spectrum to extract the spectral

[3]by GaGe Applied Technologies, part of DynamicSignals LLC, 900 N. State Street, Lockport, IL 60441, USA URL `http://www.gage-applied.com`

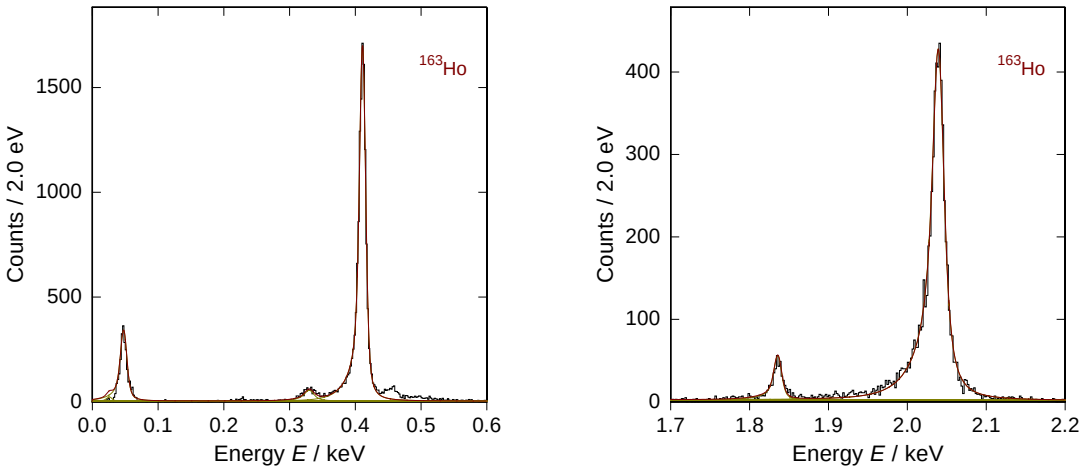

Figure 4.23 The combined spectrum of channel 2 and 4 as measured in run 4. Only the contributions from the ^{163}Dy spectrum are shown, divided into the lower energetic part with energies below $E < 0.6\,\mathrm{keV}$ (left) showing the contributions from the N_1- and N_2-lines and for the first time the O_1-line with a mean energy of $E_{O_1} = 48\,\mathrm{eV}$. The higher energetic part with energies in the range of $1.7\,\mathrm{keV} < E < 2.2\,\mathrm{keV}$ shows the M_1- and M_2-lines. The fit to the total spectrum is shown in red while the contributions from the single lines are shown separately in yellow.

features below $E < 200\,\mathrm{eV}$ as shown in figure 4.22. The resulting spectrum is shown in figure 4.23 divided into a lower and a higher energy part to allow a closer view on the features of the Dy spectrum, including the Dy O_1-line at $E_{O_1} = 48\,\mathrm{eV}$ that was observed for the first time within this work. The only additional structures around $E \approx 0.4\,\mathrm{keV}$ are the additional structures with a peak at $E \approx 0.45\,\mathrm{keV}$, while the ones attributed to the external ^{55}Fe source are not present. This substantiates the assumption of the origin of these events.

A fit as described in the previous section was performed on the data and shown in red in figure 4.23. For the fit the following parameters were kept constant:

- The average electron neutrino mass $m^2(\nu_e) = 0\,\mathrm{eV}$,
- the electron wave functions at the nucleus $\varphi^2_{\mathrm{H}}(0)$ and the exchange and overlap corrections B_{H} and
- the widths Γ_{H} and
- the energies E_{H} of the M_1- and M_2-lines as determined from run 3 (see table 4.4).

The following parameters were left free within the fit:

- The energy resolution ΔE_{FWHM},

Parameter	Value	Error	Expected value	Varied?
$m^2(\nu_e)$	0			no
$\varphi^2_{\mathrm{H}}(0)$	tab. 2.2			no
B_{H}	tab. 2.2			no
Q_{EC}	2866 eV	5 eV	2555 eV	yes
ΔE_{FWHM}	8.3 eV	0.1 eV		yes
E_{M_1}	2039.9 eV		2046.9 eV	no
E_{M_2}	1836.2 eV		1844.6 eV	no
E_{N_1}	411.1 eV	0.1 eV	420.4 eV	yes
E_{N_2}	330.3 eV	1.4 eV	340.6 eV	yes
E_{O_1}	48 eV	15 eV	49.9 eV	yes
Γ_{M_1}	13.4 eV		13.2 eV	no
Γ_{M_2}	4.8 eV		6.0 eV	no
Γ_{N_1}	4.7 eV	0.1 eV	5.4 eV	yes
Γ_{N_2}	13.2 eV	1.4 eV	5.3 eV	yes
Γ_{O_1}	5.9 eV	0.3 eV	3.7 eV	yes
m_{g}	$-0.0142\,\mathrm{keV}^{-1}$	$0.0006\,\mathrm{keV}^{-1}$		yes
n_{g}	0.905	0.003		yes
$m_{1/\lambda}$	$0.0021\,\mathrm{keV}^{-1}$	$2 \times 10^{-4}\,\mathrm{keV}^{-1}$		yes
$n_{1/\lambda}$	0.0156	0.0004		yes

Table 4.5 The parameters going into the fit or are extracted from the fit to the spectral shape of the ^{163}Dy spectrum for run 4.

- the widths Γ_{H} and energies E_{H} of the N_1-, N_2- and O_1-lines,
- the end-point energy Q_{EC},
- the relative amplitude of the pure Gaussian $a_{\mathrm{g}}(E) = m_{\mathrm{g}}\,E + n_{\mathrm{g}}$ as well as
- the exponential decay rate $1/\lambda(E) = m_{1/\lambda}\,E + n_{1/\lambda}$.

And the found parameters are quoted in table 4.5. The energy resolution in the spectrum turned out to be worse than in run 3, even though the baseline resolution was better. This can be caused by experimental influences and is not of major concern. The parameters concerning the exponential modified Gaussian stayed roughly the same, which was to be expected since the detector was operated under identical conditions as in run 3. The width of the N_1-line is comparable to its literature value, but Γ_{N_2} is determined to be much larger. This could be a true value, since the recommended value of $\Gamma_{N_2} = 5.3\,\mathrm{eV}$ has only been theoretically estimated and no direct measurement is reported in [Cam01]. It is more likely that the line is not

fitted correctly because of its low number of events and since it is heavily overlaid by the tail of the N_1-line. Additionally the N-lines of the ^{144}Pm electron capture can also be found in this region. The parameters of the O_1-line agree with the literature values even though the data is very close to the low energy threshold of the detector.

The end-point energy Q_{EC}

The end-point energy presents one of the most crucial parameters of the ^{163}Ho electron capture spectrum, since it directly impacts the statistical sensitivity on the electron neutrino mass $m^2(\nu_e)$. As discussed in chapter 2.4.4, the value directly determines the feasibility of a direct neutrino mass determination with ^{163}Ho.

The cleanest way to determine the Q_{EC} is by a measurement of the atomic masses of the parent ^{163}Ho and daughter ^{163}Dy atom as planned within the ECHo collaboration by penning trap mass spectrometry (see chapter 5.5.1). As discussed in chapter 2.4.4, the Q_{EC} was determined in various experiments by analyzing X-ray spectra and calorimetric spectra, with very differing results. Different ways to assess the Q_{EC} from the presented data will be discussed in the following.

The first way to determine the end-point is directly from the fit of the spectral shape to the measured data. As given in table 4.5 this gives $Q_{\mathrm{EC}} = (2.866 \pm 0.005)\,\mathrm{keV}$. But because there are a lot of parameters going into the fit, which might lead to a false interpretation of the data a second way to determine the Q_{EC} will be presented.

This approach is based on the idea to determine the amplitude of the phase space factor $\mathcal{C}(Q_{\mathrm{EC}} - E)\sqrt{(Q_{\mathrm{EC}} - E)^2 - m^2(\nu_e)} \approx \mathcal{C}(Q_{\mathrm{EC}} - E)^2$ (see eq. (2.30)) at the spectral lines and use the energy dependence to determine Q_{EC}. For each spectral line H the number of events n_{H} corresponding to that line are determined and than normalized by the expected line amplitudes defined by the amplitude of the electron wave function at the nucleus $\varphi^2_{\mathrm{H}}(0)$ and the exchange and overlap corrections B_{H}. Conveniently the square root of this value is taken since the root of the phase space factor is linearly dependent on the energy:

$$\Phi_{\mathrm{H}} = \sqrt{\mathcal{C}}(Q_{\mathrm{EC}} - E_{\mathrm{H}}) = \sqrt{\frac{n_{\mathrm{H}}}{\varphi^2_{\mathrm{H}}(0) B_{\mathrm{H}}}} \tag{4.28}$$

The number of events n_{H} in each line is determined in the following way: a fit to the spectral shape as described in the previous section is performed. This time the amplitudes of the individual spectral lines are allowed to vary in addition to the other parameters. Then, the integral of the fit to the individual line is taken as n_{H}. Assuming Poisson statistics, the statistical errors are defined to be

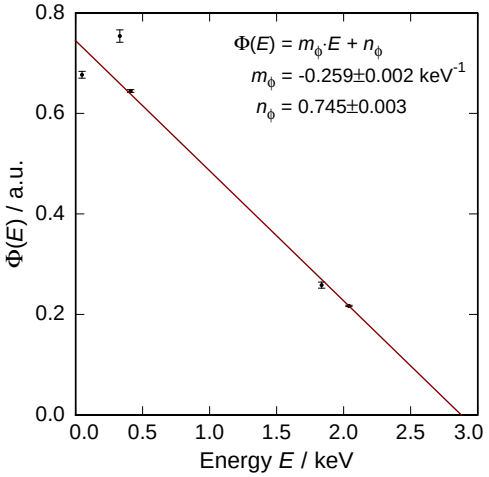

Figure 4.24 The phase space factor Φ_{H} as determined from the measured spectral lines are shown as black data points with their statistical errors. The red line shows the linear fit of $\Phi(E)$ with the parameters given in the graphic. The Q_{EC} is determined by the intersection of the fit and the abscissa.

$\sigma_{n_{\mathrm{H}}} = \sqrt{n_{\mathrm{H}}}$ (stat.). All other parameters entering this analysis are presumed to be free of errors.

The resulting phase space factors with their statistical errors are shown in figure 4.24 with a weighted linear fit $\Phi(E) = m_\phi\, E + n_\phi$. The value for the N_2-line deviates from the fit, most likely due to the influence of the tail of N_1. The deviation for the O_1-line can be justified by the close vicinity to the low energy threshold of the detector. The Q_{EC} is given by the intersection of the linear fit and the energy axis:

$$Q_{\mathrm{EC}} = -\frac{n_\phi}{m_\phi} = (2.877 \pm 0.022)\,\mathrm{keV} \ . \tag{4.29}$$

To reduce the systematic effects from the lines with smaller amplitude, the same analysis can be done by only using the events from the M_1- and N_1-lines, which results in $Q'_{\mathrm{EC}} = (2.866 \pm 0.024)\,\mathrm{keV}$. Both values of Q_{EC} extracted form the phase space factors agree very well within errors with the one from the non-linear least square fit to the spectral shape, which substantiates the determined values.

The last factor that should be discussed in the context of the end-point energy Q_{EC} are the additional events with energies slightly higher than the N_1-line. As already mentioned in chapter 4.2.5 these are of unknown origin and can therefore be very well part of the ^{163}Ho electron capture spectrum. If this is the case the events are most likely associated with captures from the N_1-shell, but are shifted to higher energies. Then these events would need to be taken into account for the Q_{EC} determination. By using the number of N_1 events increased by number of the additional events up to an energy of $E = 0.6\,\mathrm{keV}$ with the M_1 events in the phase space factor analysis a best fit value for the end-point of $Q^*_{\mathrm{EC}} = 2.815\,\mathrm{keV}$ can be determined. Because of the unknown origin of these additional events their effect

needs to be taken into account as a systematic uncertainty. As magnitude of the uncertainty the difference $Q'_{\mathrm{EC}} - Q^*_{\mathrm{EC}} = 0.051\,\mathrm{keV}$ is chosen.

Combining these factors leads to the final result on the end-point energy as determined from the data of run 4:

$$Q_{\mathrm{EC}} = (2.877 \pm 0.022\ (\mathrm{stat.})\ ^{+0}_{-0.06}\,(\mathrm{syst.}))\,\mathrm{keV}\ . \tag{4.30}$$

5. The Electron Capture ^{163}Ho Experiment – ECHo

This work is embedded in the Electron Capture ^{163}Ho Experiment (ECHo), that combines the research efforts in different fields around the ^{163}Ho electron capture and will be described in the following.

The Electron Capture ^{163}Ho Experiment (ECHo) aims to investigate the electron neutrino mass $m(\nu_e)$ with a sensitivity below $m(\nu_e) < 1\,\mathrm{eV}$. The approach is to analyze a high-resolution, high-statistics calorimetric spectrum of the electron capture process of ^{163}Ho, which offers a very good tool for neutrino mass determination as already discussed in chapter 2.4.4. In a first stage within the coming three years, a sensitivity on the order of $m(\nu_e) < 10\,\mathrm{eV}$ is envisioned, accompanied by the technological innovations and the feasibility tests for the next stage with the goal to reach the final sensitivity below $m(\nu_e) < 1\,\mathrm{eV}$.

In the following the different tasks and task-groups within the first stage that have been defined in order to reach the envisioned goals will be described.

5.1 ^{163}Ho production and purification

A very important aspect for the ECHo project is the production of a high purity ^{163}Ho source. With no primordial ^{163}Ho left on earth the nuclide needs to be artificially produced. Not only the production is an issue that needs to be addressed but also the contamination level of the source. The end-point region of the energy spectrum, which is most sensitive to the neutrino mass, needs to be as free of background as possible, and especially radioactive nuclides with continuous decay spectra, e.g. from β-decay, present a huge hazard.

In general there are three ways to artificially produce nuclides, namely nuclear spallation, thermal neutron activation and charged particle activation [Eng13].

Nuclear spallation has already been discussed in chapter 3.5 and is no option for the ECHo experiment because of the low cross section of $\sigma \approx 50\,\mu\mathrm{b}$ [Luk06] and the source contaminations discussed in chapter 3.5.1 and 4.2.4.

Neutron and charged particle activation are both based on the principle that a nucleus of a target material captures a particle and the desired nuclide is either directly produced or a precursor is created that quickly decays to the desired nuclide.

In case of ^{163}Ho the mostly used route is to produce the precursor ^{163}Er, which decays via electron capture or β^+-decay with a half-life of $T_{1/2} = 75\,\text{min}$ to ^{163}Ho.

The charged particle activation route offers a lot of possibilities. Starting from the particles used for the irradiation, e.g. protons, deuterons, α-particles or even heavier particles like ^{7}Li are considered. Secondly the different reactions can be used, e.g. direct ones $^{\text{nat.}}\text{Dy}(p, xn)^{163}\text{Ho}$ or $^{163}\text{Dy}(d, 2n)^{163}\text{Ho}$ and indirect ones like $^{\text{nat.}}\text{Dy}(\alpha, xn)^{163}\text{Er}(\text{EC}, \beta^+)^{163}\text{Ho}$. All reactions differ in their energy dependent cross sections and need to be evaluated under this aspect. Also the possible side reactions, that can happen alongside the main process and unintentionally produce radioactive contaminants need to be investigated. One very promising reaction is e.g. $^{164}\text{Dy}(p, 2n)^{163}\text{Ho}$ with a maximum cross section of $\sigma \approx 1\,\text{b}$ [Eng13, Lah13].

As a part of the ECHo project this evaluation and first experimental tests of this ^{163}Ho production route and the expected side reactions has been undertaken by a group from the Saha Institute of Nuclear Physics, Kolkata, India, the Indian Institute of Technology Roorkee, Roorkee, India and the Institute of Nuclear Research of the Hungarian Academy of Sciences, Debrecen, Hungary and is collected e.g. in [Lah13].

For neutron activation an erbium target enriched in ^{162}Er is irradiated in research reactor facilities. The ^{163}Ho is produced in the process $^{162}\text{Er}(n, \gamma)^{163}\text{Er}(\text{EC}, \beta^+)^{163}\text{Ho}$. The target can be left in the reactor for extended periods of time and the produced amount of ^{163}Ho depends on the amount of ^{162}Er in the target, on the neutron flux from the reactor and on the exposure time. This method is very efficient due to the large cross-section of $\sigma \approx 19\,\text{b}$. The neutrons can also capture on other materials present in the target, and several other nuclides can be produced, which are partly also radioactive and present possible sources for background. A very harmful nuclide is e.g. the metastable state $^{166\text{m}}$Ho that decays via β-decay with a half-life of $T_{1/2} \approx 1200\,\text{y}$. The $^{166\text{m}}$Ho can e.g. produced in the process $^{165}\text{Ho}(n, \gamma)^{166\text{m}}\text{Ho}$ with a cross-section of $\sigma = 3.1\,\text{b}$. Since it is an isotope of the same element as the desired ^{163}Ho no chemical separation is possible, and a physical mass-separation is needed.

Generally speaking, the available production rates are higher with neutron activation, but the charged particle activation processes are more selective and can be optimized for ^{163}Ho production and less contaminants are created than with neutron activation.

For all target materials used in the ^{163}Ho production chemical separation is necessary to achieve the necessary radio-purity of the produced sample. This can be done by the established process of cation-exchange chromatography with α-hydroxyisobutyric acid (α-HIB) as the solvent. With speciality highly effective exchange resins

lanthanoid separation efficiencies on the order of 90 % can be reached. A purification step before the irradiation can be used to remove the lighter lanthanoids, while a post-irradiation separation can be used to remove the heavier lanthanoids. In this way a chemically pure sample of Ho can be obtained.

Within the ECHo project a group of the Institute of Nuclear Chemistry of Johannes Gutenberg University, Mainz, Germany is handling the samples for neutron activation and their chemical processing. Three samples of erbium salts enriched in ^{162}Er have been irradiated at research reactors for ^{163}Ho production. A first test sample was irradiated at the BER II research reactor for 11 days and chemically purified only after the irradiation yielding approximately 10^{16} ^{163}Ho atoms. Two additional samples were irradiated at the research reactor at the Institute Laue-Langevin (ILL) in Grenoble. These samples were chemically separated both before and after the irradiation with a new highly efficient exchange resin. The samples were estimated to contain 10^{19} ^{163}Ho atoms and show no contaminants other than a fraction of $\sim 2 \times 10^{-4}$ ^{166m}Ho atoms, which is already very promising.

5.2 Detector production and internal ^{163}Ho source

The experimental results presented in chapter 4 show that some improvements on the single detector need to be implemented, that will improve the detector performance. The contact area between absorber and Au:Er sensor should be reduce with stems, which will reduce the athermal phonon loss, that causes the low energetic tails, as discussed in chapter 4.1.5.

Additionally the process of adding the second absorber layer for the next generation of experiments will be conducted differently. The prototype detector was ion-implanted in an online process at ISOLDE/CERN as described in chapter 3.5. The radioactive contaminants required, that the detector was left to cool down for about three month and that a thin 100 nm gold layer was added to close off the implantation area. The limited facilities for the gold deposition, that were available did not allow a suitable surface cleaning before the gold deposition. This fact might have caused the rise time distribution shown in figure 4.7. Fortunately the next generation of experiments will use a much more radio-pure source, that will not require to be immediately closed off after the deposition. Therefore the addition of the second absorber layer can be executed in a better controlled clean room environment with all facilities, that are normally used for the detector production. Additionally the second absorber layer will be added by electroplating to avoid the excess heat capacity observed in sputter deposited gold films as discussed in chapter 4.1.3.

Another aspect directly connected to the detector preparation is the embedded

^{163}Ho source. In [Gat97] the ^{163}Ho source material was in form of an organic salt that was sandwiched between two thin absorber layers made of tin. They observed unexpected energy shifts in the ^{163}Ho electron capture spectrum compared to their calibration data. The conclusion can be drawn, that it is not only important to contain all emitted energy from the decay to make the measurement calorimetric, but also the chemical state of the source material can have a significant impact on the measured spectrum.

Therefore the ^{163}Ho source should be in atomic form when it is introduced into the detector's absorber. The first possible way to achieve that is the preparation of intermetallic samples containing the source material. For this process the source material is deposited onto a nobel metal foil in any organic salt form by molecular plating and is subsequently reduced at elevated temperatures in a pure hydrogen flow. After the reduction the source material will diffuse into the nobel metal and form a chemically stable intermetallic phase.

This process has successfully been shown for several lanthanides (Gd, Nd, Eu) on a Pd foil [Uso12] and can possibly applied to Ho as well. The reported efficiencies in the molecular plating process are very high, close to 100 %, which is a great advantage, considering the challenging ^{163}Ho production. This reported efficiency needs to be treated with caution, since the total efficiency after the reduction process is not reported. Additionally there is some development necessary to make this process compatible with metallic magnetic calorimeters. Unfortunately the necessary temperatures of around $T \approx 1000\,^{\circ}\mathrm{C}$ are not compatible with the standard microfabrication of MMCs and the fabrication of Josephson junctions for the multiplexed read-out. As a consequence the source foil or the absorber and source sandwich would need to be produced first and then be attached to an already prepared detector.

The second aspect that will need investigation is the host material used in the process. While Pd works very well in the reduction process because of its chemical properties it has never been used in combination with MMCs. Therefore both the compatibility of MMCs with Pd as well as alternative host materials should be investigated.

The second considered process is ion-implantation in an offline process. The previously produced and purified source material in acid solution is dried on a suitable substrate. The ^{163}Ho is subsequently introduced into an ion-source, is accelerated, mass separated and ion-implanted into the detectors, as already described in chapter 3.5.

The ion-implantation technique has already been successfully used for the detectors used in this thesis and has shown very promising results. Neither the detector

behavior and performance nor the spectral shape have been compromised by the process outside the expectation (see chapter 4). This has encouraged the further application of the ion-implantation technique for the next stage of the ECHo project. The mass separation, which comes natural with the ion-implantation, will be necessary for the source produced by thermal neutron activation. The largest radioactive contaminant after the chemical separation is in fact a fraction of 2×10^{-4} ^{166m}Ho atoms, that can be strongly suppressed to a least a fraction of 10^{-6} or completely removed by mass separation. If the subsequent experiments reveal, that the amount of ^{166m}Ho present after the mass separation is still too large, a different starting material will be required, that is e.g. produced by charged particle activation.

A major drawback of ion-implantation, especially for a large scale experiment, is the efficiency of the process. Depending on the ionization technique only about $10 \ldots 20\,\%$ of the source atoms will contribute to the final ion beam. Secondly the implantation area will be only a fraction of the total detector surface and a part of the ions will be lost due to the detector geometry. This places the total efficiency of the process around $\sim 10\,\%$.

Within the first stage of the ECHo project, the ion-implantation will be used on the source material produced by thermal neutron activation. The ion-implantation will be optimized to reach an efficiency as high as possible. The optimization and implantation tests will be conducted at the RISIKO mass separator at Johannes Gutenberg University, Mainz, Germany, while the final implantation will take place at ISOLDE/CERN. Meanwhile other deposition techniques, e.g. the formation of intermetallic samples, are under investigation for future larger scale experiments.

5.3 Multiplexed read-out of metallic magnetic calorimeters

A different aspect that needs to be addressed within the ECHo project is the detector read-out. Typically metallic magnetic calorimeters are read-out with dc-SQUIDs, which have been described in chapter 3.3. A detector read-out by means of a two-stage dc-SQUID fulfills the requirements on noise performance and available bandwidth very well. Unfortunately the two-stage SQUID detector read-out is only usable for detector counts up to an order of 100, before the necessary read-out infrastructure becomes too extensive and hardly manageable. The required number of wires and the number of read-out electronics increases linearly with the detector count. This will also increase the heat load on the experimental platform, until the local detector temperature is too large for an optimal detector operation.

Because of the strong requirements on statistics (see chapter 2.4.4) for neutrino mass searches, the required detector count within ECHo will be on the order of

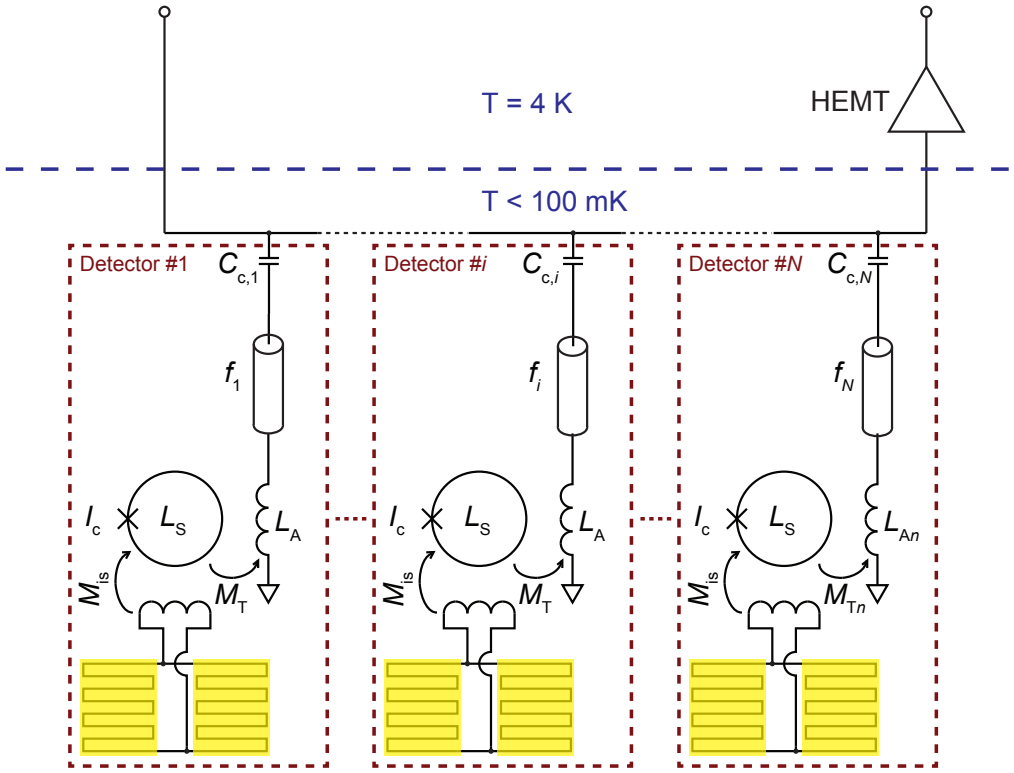

Figure 5.1 Schematic of the microwave SQUID multiplexing scheme for metallic magnetic calorimeters. The N detectors are coupled to rf-SQUIDs L_S, which are in turn coupled to load inductors L_A that are terminating microwave resonators with a unique resonance frequency f_i. The resonators are the capacitively coupled to a common feedline through $C_{c,i}$. The detector signals are encoded into a frequency shift of the resonators and can be read-out through amplitude or phase shift.

$10^4 \ldots 10^6$. Therefore a multiplexing technique needs to be utilized, which will allow multiple detectors to be read-out through a single read-out channel. Ideally this technique should preserve the important detector properties, above all the energy resolution and the rise time, while greatly simplifying the cryogenic setup and the room temperature electronics.

Out of the available multiplexing techniques that can be applied to MMCs, the microwave SQUID multiplexing technique is the most favorable one for the read-out of large ($N > 100$) detector arrays. This read-out scheme has been first demonstrated for transition-edge sensors [Mat08, Mat11] and has later been adapted for metallic magnetic calorimeters [Kem12, Kem13, Kem14].

A schematic of this read-out scheme is shown in figure 5.1. Each detector is inductively coupled via the mutual inductance M_{is} to a single junction un-shunted non-hysteretic SQUID, that is described by the loop inductance L_S and the critical current of the Josephson junction I_c. For $\beta_L := 2\pi L_S I_c/\Phi_0 < 1$, the SQUID

can be modelled as a flux-sensitive inductance, whose actual value depends on the magnetic flux Φ flowing through the SQUID loop. The SQUID is coupled via the mutual inductance M_{T} to a load inductors L_{A}, that terminates a superconducting transmission line resonator with a unique resonance frequency f_i. Because of the flux sensitivity of the SQUID, the load inductor becomes flux sensitive and can be described by the effective inductance $L_{\mathrm{eff}}(\Phi)$. The frequency shift corresponding to a detector signal can then be monitored with the help of standard homodyne or heterodyne detection techniques.

Each resonator is on the other hand capacitively coupled to a common transmission line via the capacitance $C_{\mathrm{c},i}$, making it possible to simultaneously read-out hundreds or thousands of individual detectors.

For this, all resonators are simultaneously driven by injecting a frequency comb and the amplitude or phase of the transmitted signal are continuously monitored.

The number of detectors per channel that can be read-out by this technique is limited by the required bandwidth for each detector, the bandwidth of the cryogenic pre-amplifier, as well as the required level of crosstalk between adjacent resonators. To be able to resolve the fast rise time $\tau_0 \approx 100\,\mathrm{ns}$ of metallic magnetic calorimeters a bandwidth of at least $B \approx 2\,\mathrm{MHz}$ per detector is necessary and the bandwidth of cryogenic low-noise high-electron-mobility transistor (HEMT) amplifiers are on the order of $B = 4\,\mathrm{GHz}$. With the low crosstalk, that has been reached for microwave kinetic inductance detectors (MKIDs) [Day03] with closely packed resonators [Nor12], potentially hundreds of detectors can be read-out by this multiplexing technique.

The generation of the frequency comb and the later analysis of the GHz-frequency signals can in general be handled by digital Software-Defined-Radio (SDR) techniques, that have been successfully used for read-out of cryogenic detectors [Maz06]. In SDR the frequency comb is created with digital-to-analog converters at MHz frequencies with the right frequency spacing between the resonances. This signal is then mixed up to the desired frequency band in the GHz range. The detection side works in a similar fashion, that the signal is first mixed down to MHz frequencies and then digitized with analog-to-digital converters.

A collaborative effort based on the idea presented in [Maz06] has lead to the development of a commercially available open-source SDR system within the CASPER[1] collaboration that can be customized to the specific use. Within this framework an array of 1024 MKIDs, which also use a similar setup of microwave resonators, have been read-out with a bandwidth of $B = 500\,\mathrm{kHz}$ per channel and a time resolution between events of $\Delta t = 1\,\mu\mathrm{s}$ [McH12]. A similar performance will be sufficient for the

[1] Collaboration for Astronomy Signal Processing and Electronics Research, URL `http://casper.berkeley.edu`

first stage of ECHo, a final experiment with a statistical sensitivity of $m(\nu_e) < 1\,\mathrm{eV}$ will need to be able to resolve the full bandwidth of $B \approx 2\,\mathrm{MHz}$ to be able to reach the event discrimination time of $\Delta t \approx 100\,\mathrm{ns}$ that has been shown with metallic magnetic calorimeters.

5.3.1 The ECHo prototype detector array

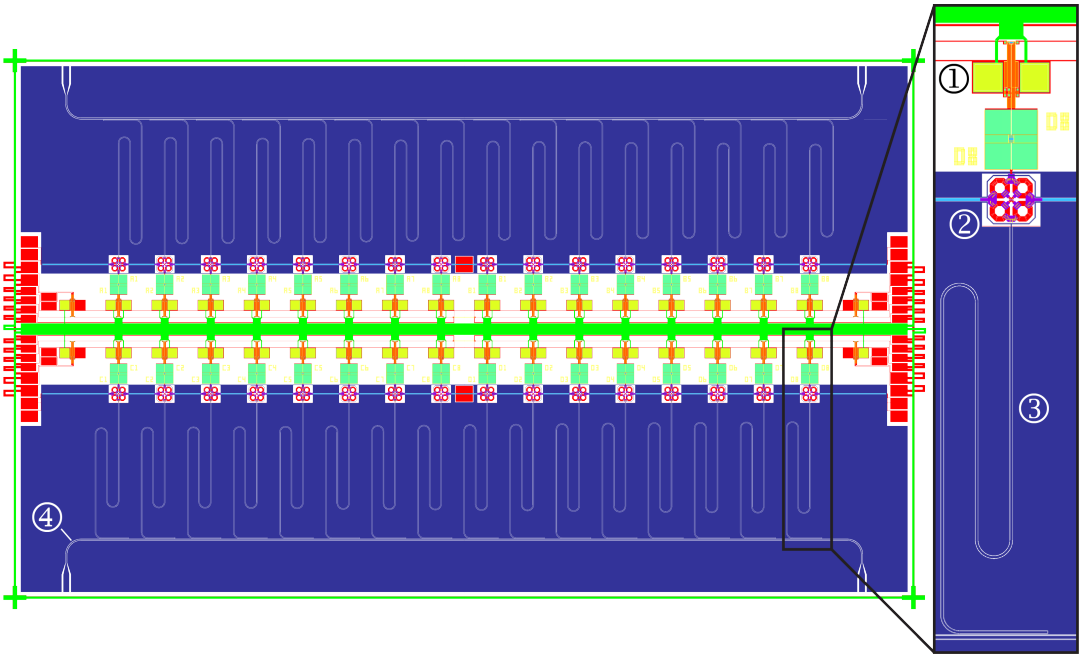

Figure 5.2 Design drawing of the ECHo#1 detector array. The 9.1 mm × 15.4 mm chip contains 64 detector pixels with integrated rf-SQUID multiplexed read-out. The zoom shows one of the basically identical read-out channels consisting of a detector ①, an rf-SQUID ② and a coplanar superconducting transmission line resonator ③. The different resonators on the chip are coupled to a common transmission line ④.

The presented results on the ^{163}Ho electron capture decay show how well suited metallic magnetic calorimeters are for neutrino mass determination utilizing the ^{163}Ho electron capture. To show a significant sensitivity on the neutrino mass much larger statistics will be necessary. This can only be achieved with a combination of more detectors, a stronger source and more acquisition time.

The next step towards more detectors has been undertaken in [Weg13, Kem13], where an array of 64 detector pixels with an integrated rf-SQUID multiplexer was designed and fabricated. An overview over the chip design is shown in figure 5.2. The detector array is fabricated on a 9.1 mm × 15.4 mm thermally oxidized Si substrate and consists of basically identical 32 read-out channels. Each channel contains an MMC with two detector pixels (fig. 5.2 ①) and the read-out infrastructure consisting of an rf-SQUID (fig. 5.2 ②) and a coplanar superconducting transmission

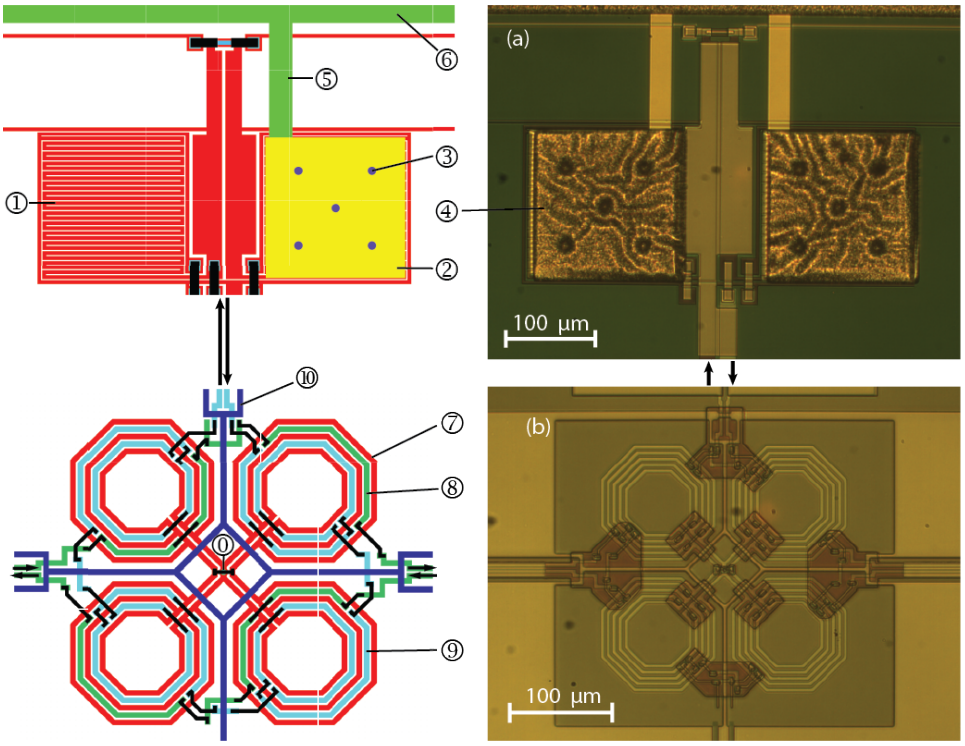

Figure 5.3 Design drawing and optical photos of (a) a detector with two pixels and (b) An rf-SQUID. The elements of the detector are the meander-shaped pick-up coil ①, the Au:Er sensor ②, the stems ③, the absorber ④ and the thermal link ⑤ to the common on chip heat bath ⑥. The rf-SQUID is composed of a Josephson junction ⓪, a slotted washer ⑦, a modulation coil ⑧, an input coil ⑨ and a load inductor ⑩. The connection between meander structure and SQUID input coil is indicated by the arrows between detector and SQUID.

line resonator (fig. 5.2 ③). The different resonators are coupled to a common transmission line (fig. 5.2 ④).

A design drawing and an optical view of one of the MMCs is shown in figure 5.3 (a). The detectors are based around 170 µm × 170 µm × 10 µm particle absorbers (fig. 5.3 ④) with a heat capacity of $C_{\mathrm{abs}} = 1\,\mathrm{pJ/K}$ at $T = 30\,\mathrm{mK}$, that consist of two 5 µm layers, that will contain the ^{163}Ho source material in between. The absorbers are contacted to the Au:Er sensor (fig. 5.3 ②) via five stems (fig. 5.3 ③) that only make up about 2 % of the total absorber area, therefore reducing the athermal phonon loss to the solid substrate. The 170 µm × 170 µm × 1.35 µm Au:Er sensor has an erbium concentration of $c_{\mathrm{Er}} = 300\,\mathrm{ppm}$ and is positioned on top of a meander-shaped pick-up coil (fig. 5.3 ①) with a stripe width of $w = 3\,\mu\mathrm{m}$ and a pitch of $p = 6\,\mu\mathrm{m}$. The broad gold stripes (fig. 5.3 ⑤) connect the sensors with a common thermal bath (fig. 5.3 ⑥) in the middle of the chip and adjust the thermal

relaxation time to $\tau_1 \approx 1\,\mathrm{ms}$ at the planned operating temperature of $T = 30\,\mathrm{mK}$. The leads to the bottom connect the detector to the input coil of the rf-SQUID.

The meander-shaped pick-up coil is connected in parallel to the input-coil (fig. 5.3 ⑨) of an rf-SQUID shown in figure 5.3 (b). The SQUID forms a second order gradiometer, that is formed from four slotted octagonal washers (fig. 5.3 ⑦) connected in parallel. With a nominal inductance of 200 pH of each washer, the SQUID loop has a total inductance of $L_\mathrm{S} = 50\,\mathrm{nH}$. The Josephson junction (fig. 5.3 ⓪) is designed with a critical current of $I_\mathrm{c} = 5\,\mu\mathrm{A}$, resulting in a hysteresis parameter of $\beta_\mathrm{L} = 0.76$. Additionally the SQUID is equipped with a common flux modulation coil (fig. 5.3 ⑧), that runs through all SQUID on the chip. This coil can be used for simultaneous flux biasing and flux ramp modulation [Mat12].

The load inductor (fig. 5.3 ⑩) couples the SQUID to the coplanar transmission line resonator (fig. 5.2 ③) with a resonance frequency f_i between 4 and 6 GHz, which is set by its geometrical length. The coupling capacitance C_c is adjusted accordingly to reach a loaded quality factor of $Q_\mathrm{l} = 5000$, by varying the length, that the resonator runs in parallel to the common transmission line (fig. 5.2 ④).

With these design parameters and the usual operating conditions for the read-out, an energy resolution of $\Delta E_\mathrm{FWHM} = 5\,\mathrm{eV}$ can be expected for the detectors.

This detector array is currently being tested and will provide a very crucial asset to the ECHo experiment in the coming time. A detector based on this or an optimized design, that takes adjustments resulting from the tests into account, will be ion-implanted with ^{163}Ho, which is scheduled at ISOLDE/CERN in late 2014. One or several of these detectors will provide the grounds for the first stage of the ECHo project and will allow to measure the ^{163}Ho electron capture spectrum with approximately $N_\mathrm{ev} = 10^{10}$ events, allowing a statistical sensitivity of $m(\nu_e) < 10\,\mathrm{eV}$ on the electron neutrino mass within one year of acquisition time.

5.4 Background studies

The statistical analysis of the ^{163}Ho electron capture spectrum for neutrino mass determination in the end comes down to the analysis of a narrow energy range below the spectrum end-point Q_EC. Considering an end-point of $Q_\mathrm{EC} = 2.8\,\mathrm{keV}$, a zero neutrino mass $m^2(\nu_e) = 0\,\mathrm{eV}$ and an energy range of 10 eV below the end-point, a fraction of about 6×10^{-10} of the total number of counts is expected. For a total of 10^{14} events, which can be realistically acquired within 3 years of measurement, this means that about 60 000 events will be located in the last 10 eV of the spectrum. Only one background event in approximately 4 days over the whole acquisition time in this energy range will create an error larger than the statistical error on the

number of counts.

This illustrates how easily a statistical analysis can be influenced and compromised by unidentified background. Therefore the reduction of background sources, or if no further reduction is feasible, a good understanding of it is of utmost importance. Over the course of the last decades a broad range of computational tools and experimental techniques for background identification and reduction have been developed, mainly for neutrinoless double β-decay experiments and dark matter searches. The computational tools are mainly based Monte Carlo simulations of background sources and their signature in the detectors. Experimental techniques include handling and characterization of materials used in and close to the detectors, passive shielding materials as well as active veto methods.

Unfortunately all established tools are normally used at much higher energies, since the region of interest of most rare event searches is in the MeV range. Nonetheless e.g. the "Cryogenic Rare Event Search with Superconducting Thermometers" (CRESST) experiment has observed background events below $E < 10\,\mathrm{keV}$ [Ang12] and in the region of interest of ECHo.

On the other hand ECHo is dealing with totally different detector and source masses than the before mentioned rare event searches. Current $0\nu\beta\beta$-experiments for example are on the order of $10 \ldots 100\,\mathrm{kg}$ source mass that is in most cases equal to the detector mass with single detectors weighing several hundred grams. ECHo uses single detectors with masses of $m_\mathrm{d} \approx 5\,\mu\mathrm{g}$, a total detector mass for a large scale experiment in the gram range and a source mass below $m_\mathrm{s} < 1\,\mathrm{mg}$.

All these different constraints need to be taken into account while estimating background and require appropriate adjustments. On the other hand a lot can be learned from dedicated experiments for background estimation. This mainly includes experiments with the same detectors that will be used for the ECHo measurements, but without ^{163}Ho source material under different conditions. These conditions include, but are not limited to, measurements in underground laboratories to see the influence of secondary particle showers caused by cosmic rays and the effects mainly caused by cosmic muons and electrons. Also studied will be different shielding materials, both at cryogenic temperatures close to the detectors or at room temperature outside the cryostat. This will most likely be a mix of high-Z materials like lead to shield γ-rays and low-Z materials like polyethylene to stop massive particles like neutrons, α-particles and electrons without creating a lot of bremsstrahlung. By operating the cryogenic detectors in coincidence with active veto detectors will for example reveal, what signature will be picked up by the cryogenic detectors if a cosmic muon passes through the cryostat.

Another aspect that falls into the realm of background reduction is the selection

and the screening for radioactive contaminants of high purity materials, that will be used for the detector setup and the shielding.

As detailed studies and dedicated experiments as possible will be conducted during the first phase of ECHo to define the measures for background reduction and identification during that stage. From the experience of the first phase the studies will be continued and improved to the necessary level of a large scale experiment.

5.5 ^{163}Ho electron capture spectrum parametrization

The statistical sensitivity discussed in chapter 2.4.4 considers the parameterization given in equation (2.30), when all the parameters describing the spectrum, besides the Q_{EC}, as precisely known. In order to refine the statistical analysis and to quantify and reduce the errors on the parameters entering in the spectrum, dedicated investigations are carried out within the ECHo experiment. This parametrization will be performed by a range of dedicated experiments as well as theoretical calculations.

5.5.1 Q_{EC} determination by Penning-trap mass spectrometry

The end-point energy Q_{EC} of the ^{163}Ho electron capture spectrum has the largest influence on the sensitivity of a ^{163}Ho experiment. An independent determination of its value is of utmost importance, first of all to refine the statistical analysis as well as to analyse the final spectrum.

The most sensitive way to determine the Q_{EC}-value of a decay is by a mass measurement of the mother, in this case ^{163}Ho, and the daughter atom, in this case ^{163}Dy. Presently the most precise tool for mass spectrometry are ion traps, especially Penning-trap mass spectrometers (see e.g. [Bla06]). These use the fact that the cyclotron frequency ν_{c} of a charged particle, with charge q, in a magnetic field B depends on the particles mass M:

$$\nu_{\mathrm{c}} = \frac{1}{2\pi}\frac{q}{M}B \ . \tag{5.1}$$

To prolong the observation time on the cyclotron frequency and therefore the measurements accuracy the particles are trapped. The particle's motion can be confined to volumes on the order of tens of cubic micrometers by superimposing a quadrupole electric field to the magnetic field. With state of the art Penning-trap mass spectrometers relative accuracies below the level of $< 10^{-11}$ have been

reached [Rai04], which will be necessary to measure the Q_{EC} of ^{163}Ho with an accuracy on the single eV-level.

To reach this accuracy level very precise knowledge and control of all experimental parameters is needed. This includes the magnetic and electric fields of the trap, but comes down to the laboratory environment, including precise control over the temperature and pressure in the room and shielding from surrounding electric and magnetic fields.

For the ECHo project three different experimental setups are involved in the Q_{EC} determination. At the TRIGA-TRAP [Ket08] the ion-preparation of ^{163}Ho and ^{163}Dy will be developed and tested, combined with a first measurement of Q_{EC} with an expected accuracy of a few hundred eV. This is followed by a measurement at SHIPTRAP [Blo07] that will adapt the previously developed ion-preparation processes and is expected to reach an accuracy on the order of $30 \ldots 50\,\mathrm{eV}$ due to its more elaborate detector system, as recently shown in the Q_{EC} determination of the β-decay of ^{187}Re to ^{187}Os [Eli14].

The highest accuracy for the ^{163}Ho Q_{EC} will be made by using the novel Penning-trap mass spectrometer PENTATRAP [Rep12], that is currently being comissioned. The expected accuracy is on the order of $< 10^{-11}$ which translates into an accuracy on the Q_{EC} of ^{163}Ho of around $\sim 1\,\mathrm{eV}$.

5.5.2 Theoretical description of the electron capture of ^{163}Ho

In [DR82] a theoretical description of the ^{163}Ho electron capture spectrum under ideal conditions was described. Many effects that could influence the spectral shape, like second order transitions and solid state effects were considered negligible until recently. State of the art detectors, as they will be used for ECHo, would be sensitive to these effects. Many of the small effects will have no immediate effect on the pure analysis of the end-point region for the effect of the neutrino mass [DR13]. Other influences, especially effects, that could shift the observed end-point Q_{EC} will directly influence the end-point region analysis. Additionally, these effects on the whole differential spectrum, as it is measured within ECHo, will not be negligible and a good understanding of the spectral shape will reduce systematic uncertainties.

The first factor that needs to be addressed are the partial capture rates from the different electron shells that the capture is allowed from. These have already been calculated with different approaches and are collected e.g. in [Bam77] or [Ban86]. Theoretical models as well as the computational power have largely improved within the last 30 years and will lead to a major improvement in a new, dedicated evaluation.

Additionally chemical effects can influence most of the spectral parameters. Most calculations on the spectral parameters are done on single atoms in vacuum. Within a calorimetric measurement the atoms will be embedded in some sort of host material and interactions between the source atoms with one another and with host material atoms will occur. This circumstance can influence the observed Q_{EC} value, the observed energy levels and the level widths and could lead to different intensities for radiative and electronic de-excitations.

A precise knowledge of the spectral parameters will not only reduce the systematic error for the investigation of $m(\nu_e)$, but allow to investigate other effects related to neutrinos, as for example the possible sterile neutrino admixture.

6. Summary and outlook

The electron capture of ^{163}Ho offers a very powerful tool for neutrino mass determination due to its low end-point energy Q_{EC}, that has been reported to be in the range of $Q_{\mathrm{EC}} = 2.3 \ldots 2.8\,\mathrm{keV}$. Thermal detectors operated at cryogenic temperatures below $T < 1\,\mathrm{K}$ have shown very good performance in this energy range.

In this work a cryogenic metallic magnetic calorimeter was ion-implanted with ^{163}Ho at the ISOLDE/CERN facility in order to perform a calorimetric measurement on the ^{163}Ho electron capture. The detector was characterized to determine the influence of the ^{163}Ho source on the otherwise very well understood detector. The characterization revealed that neither the thermodynamic properties nor the detector performance were impaired by the presence or the implantation process of the ^{163}Ho source. Furthermore an energy resolution of $\Delta E_{\mathrm{FWHM}} = 7.3\,\mathrm{eV}$ and rise times as low as of $\tau_0 = 80\,\mathrm{ns}$ were measured. This implies that the achieved detector performance is perfectly suited for a neutrino mass experiment based on ^{163}Ho.

The ^{163}Ho electron capture spectrum was measured with the same detector, which is the best resolved spectrum up to now and offers various possibilities to extract the parameters, that describe the spectrum. For the first time the de-excitation of an electron capture from the ^{163}Ho O_1-level at $E_{O_1} = 48\,\mathrm{eV}$ has been measured calorimetrically. It was found that the central line energies are shifted towards lower energies by about $\Delta E < 10\,\mathrm{eV}$ compared to the corresponding binding energies of the daughter atom ^{163}Dy. The line width agree with the literature values within the experimental resolution. One of the most important parameters, namely the end-point energy has been determined to $Q_{\mathrm{EC}} = (2.877 \pm 0.022\ (\mathrm{stat.})\ ^{+0}_{-0.06}\ (\mathrm{syst.}))\,\mathrm{keV}$.

A lot of experience was gained in the event discrimination with metallic magnetic calorimeters, the combination and analysis of measured spectra, as well as with long-term measurements. This will be useful in future measurements, that will require stable detector operation for several month up to years at a time.

The results also revealed that there are several aspects that can improve the measurements. The analysis of the detector response suggests to use stems to avoid energy losses due to athermal phonons and to improve the fabrication of the second gold absorber layer, that currently affects the rise of the signals. In the online implantation the source could not be purified and contaminations were seen in the measured spectrum. The ion-implantation process should in future be used in an offline process from a previously produced and purified target, which will also allow a larger activity per pixel. There still remain many open questions on the ^{163}Ho

electron capture spectrum, which can only be answered in future research efforts.

The background was not addressed in this work because of the large impact of the contaminations in the source, but it needs to be addressed in future. Higher order corrections to the spectral shape will require investigations. Atomic physics, nuclear physics and solid state physics will be considered when describing the spectrum and these theoretical studies will be supported by dedicated experiments, e.g. by embedding ^{163}Ho in different suitable absorber materials. The analysis of the end-point energy Q_{EC} presented in this work and previous studies require theoretical input of the atomic parameters, that need to be re-evaluated, and suffer from the same systematic uncertainties as the measurement of the spectrum itself. Therefore also independent experimental determination of Q_{EC} will be needed.

The results presented in this work have encouraged the international scientific community to consider the ^{163}Ho electron capture as a viable option for future neutrino mass experiments. Two major collaborations investigating the electron capture of ^{163}Ho have recently been formed, the HOLMES experiment and the ECHo experiment. This work is part of the ECHo experiment.

The aim of the ECHo experiment is to set up large arrays of metallic magnetic calorimeters with $10^4 \ldots 10^6$ individual detectors, that will be read-out by the microwave SQUID multiplexing technique. These arrays will be used to acquire a high-statistics spectrum of the ^{163}Ho electron capture to allow a sub-eV sensitivity on the electron neutrino mass.

The ^{163}Ho production and purification is an important task to provide the source material for the experiments. The production processes need to be optimized and the capabilities of nuclear chemistry need to be fully utilized to provide a as radiopure source as possible for the subsequent measurements.

The detectors need to be optimized to reach the best possible performance in reliability, energy resolution and rise time not to impair the statistical sensitivity. Highly efficient multiplexing techniques need to be employed to allow the read-out of the large detector arrays, that are necessary to reach the required statistics.

The background reduction and prediction of the experiment will require work in an uninvestigated low energy range, which will put the experience and the models applied to higher energies to the test.

Also the parametrization of the ^{163}Ho electron capture spectrum is not finalized at this point. Dedicated experiments as well as theoretical calculations will be required to correctly understand the measured spectrum and avoid systematic uncertainties.

While there is still a long way to go from here, the foundation for the neutrino mass determination utilizing the ^{163}Ho electron capture is laid.

A. Physical properties of the sensor material Au:Er

This summarization of the physical properties of the sensor material Au:Er is primarily based upon and partly reproduced from the explanations in [Sch00, Fle03b, Fle05] and is added for the convenience of the reader. Other sources are cited throughout the text.

A.1 Properties of Erbium in Gold

Erbium in low concentrations forms a solid solution with gold [Rid65]. Erbium in the 3+ state substitutes for Au at regular fcc lattice sites giving three of its electrons to the conduction band. The Er^{3+} ion has the electron configuration $[Kr]4d^{10}4f^{11}5s^25p^6$. The paramagnetic behavior results from the partially filled $4f$ shell, having a radius of only about 0.3 Å and located deep inside the outer $5s$ and $5p$ shells. For comparison, the ionic radius of Er^{3+} is about 1 Å, as is depicted in figure A.1. Because of this the influence of the crystal field is greatly reduced and the magnetic moment can be calculated from the orbital angular momentum $\boldsymbol{L}$ the spin angular momentum $\boldsymbol{S}$ and the total angular momentum $\boldsymbol{J}$, which are derived according to Hund's rules. To a good approximation the admixture of exited electronic states can be neglected and the magnetic moment $\boldsymbol{\mu}$ can be written as

$$\boldsymbol{\mu} = g_J \boldsymbol{J} \tag{A.1}$$

with the Landé factor

$$g_J = 1 + \frac{J(J+1) + S(S+1) - L(L+1)}{2J(J+1)} \quad . \tag{A.2}$$

For Er^{3+}, $L = 6$, $S = {}^3/_2$, $J = {}^{15}/_2$ and $g_J = {}^6/_5$. In dilute Au:Er samples the magnetization can indeed be characterized by (A.1) at temperatures above about 100 K [Wil69]. At lower temperatures it is necessary to include crystal field effects in the description. The crystal field with fcc symmetry lifts the sixteen-fold degeneracy of the Er^{3+} ground state, splitting it into a series of multiplets (one Γ_6 and one Γ_7 doublet and three Γ_8 quartets). The lowest lying multiplet is a Γ_7 Kramers doublet. At sufficiently low temperatures and low magnetic fields the behavior of erbium in gold can be approximated as a two level system with effective spin $\tilde{S} = {}^1/_2$ with an isotropic g factor of $\tilde{g} = {}^{34}/_5$. This theoretical value has been confirmed by several

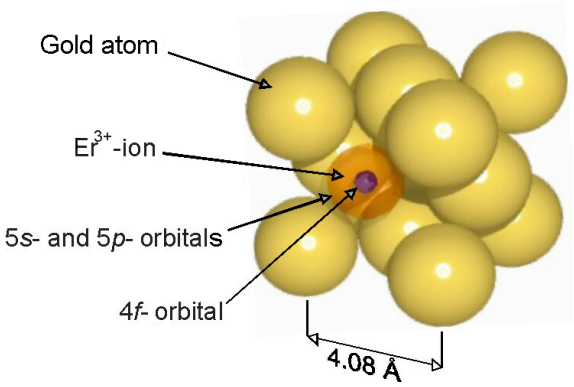

Figure A.1 Schematic of a lattice section of the Au:Er-alloy. The Er^{3+}-ions take regular sites within the Au-lattice. The only partially filled Er $4f$-shell lies deep within the ion.

ESR experiments (see, for example [Tao71]). The magnitude of energy splitting between the ground state doublet and the first excited multiplet (Γ_8 quartet) has been reported in different experiments [Sjø75, Dav73, Wil69, Hah92] to be between 11 K and 19 K.

Figure A.2 shows the magnetic susceptibility of Au doped with 600 ppm Er in the temperature range between 100 µK and 300 K. The data have been obtained in three different experiments [Her00, Fle03b]. While the data at high temperatures ($T > 100$ K) are in good agreement with the Curie law for $J = {}^{15}/_{2}$ and $g_J = {}^{6}/_{5}$ there is an increasing deviation from the high temperature approximation below 100 K. This is a result of the depopulation of the multiplets with higher energies. At temperatures below about 1.5 K the data follow a Curie law once again, but with a reduced Curie constant in agreement with the effective spin $\tilde{S} = {}^{1}/_{2}$ and g factor $\tilde{g} = 6.8$ for the ground state doublet. At temperatures below 50 mK and in low magnetic fields such that saturation is unimportant ($\tilde{g}\mu_B B < k_B T$), the susceptibility becomes much less temperature dependent. This is a result of the influence of the exchange interaction between the magnetic moments. Finally, at a temperature of about 0.9 mK a maximum in the magnetic susceptibility of the 600 ppm sample is observed, which is the result of a transition to a spin glass state.

A.2 Thermodynamic characterization of non-interacting magnetic moments

The magnetization of the Au:Er alloy, due to the properties of the Er^{3+}-ions, can be used as a temperature information. And since the magnetization is a thermodynamic equilibrium property it can be accurately described theoretically. Starting from a

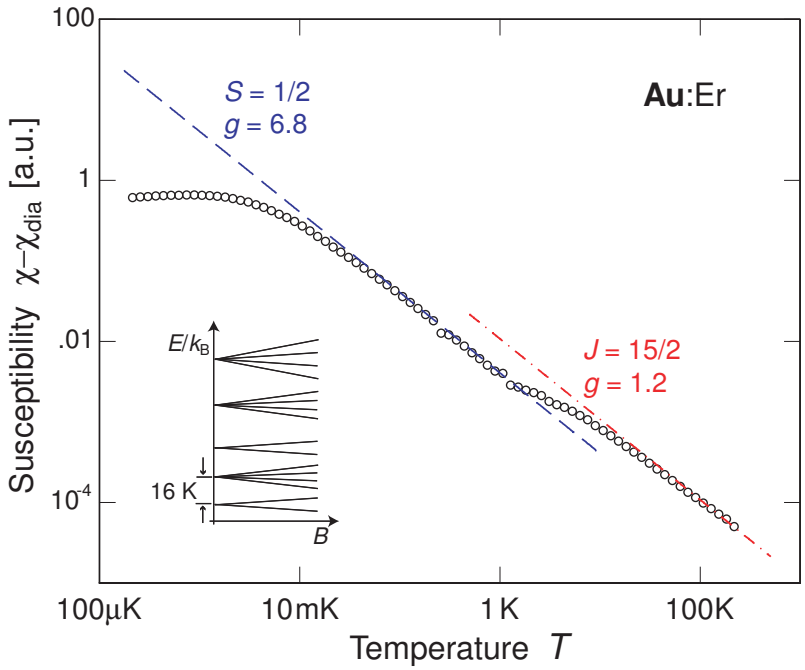

Figure A.2 Paramagnetic contribution to the magnetic susceptibility of Au containing 600 ppm Er as a function of temperature. The *two straight lines* represent the Curie susceptibility assuming Er^{+3} ions in the Γ_7-groundstate doublet and Er^{+3} ions without crystal field splitting. After [Fle03b]

suitable thermodynamic potential, like the free energy with its's full differential

$$\mathrm{d}F = -S\,\mathrm{d}T - VM\mathrm{d}B - \underbrace{p\,\mathrm{d}V}_{=0} \ , \tag{A.3}$$

with the volume change $\mathrm{d}V$ being negligibly small. The free energy F in statistical physics can be found to be

$$F = -Nk_\mathrm{B}T\ln z \ , \tag{A.4}$$

being a function of the number of magnetic moments N, the Boltzmann constant $k_\mathrm{B} = 1.381 \cdot 10^{-23}\,{}^\mathrm{J}/_\mathrm{K}$ and the canonical partition function:

$$z = \sum_i \mathrm{e}^{-\frac{E_i}{k_\mathrm{B}T}} \ , \tag{A.5}$$

with E_i being the energy eigenstates available to one magnetic moment. This preparatory work (eq. A.3-A.5) can now be used to calculate the properties necessary to estimate the performance as a thermometer from our system, namely the heat capacity C, the magnetization M and it's change with temperature ${}^{\partial M}/_{\partial T}$:

$$C = \frac{N}{k_\mathrm{B}T^2}\Big\{\big\langle E^2\big\rangle - \big\langle E\big\rangle^2\Big\} \ , \tag{A.6}$$

$$M = -\frac{N}{V}\left\langle\frac{\partial E}{\partial B}\right\rangle \ , \tag{A.7}$$

$$\frac{\partial M}{\partial T} = \frac{N}{Vk_\mathrm{B}T^2}\left\{\left\langle E\,\frac{\partial E}{\partial B}\right\rangle - \big\langle E\big\rangle\left\langle\frac{\partial E}{\partial B}\right\rangle\right\} \ . \tag{A.8}$$

This general theory on magnetic moments will now be applied to the case of $^{3+}$Er ions in gold. In the previous section A.1 it was shown that at low temperatures only two alignments are possible for the magnetic moments of the ions in an external magnetic field B. The matching energy eigenvalues are

$$E_{m_{\tilde{\mathrm{S}}}} = m_{\tilde{\mathrm{S}}}\tilde{g}\mu_\mathrm{B}B \ , \tag{A.9}$$

with $m_{\tilde{\mathrm{S}}} = \pm{}^1\!/_2$ being the z-component of the quasi spin, $\tilde{g} = 6.8$ the effective isotropic Landé factor of the Γ_7 Kramers doublet, $\mu_\mathrm{B} = 9.274 \cdot 10^{-24}\,\mathrm{Am}^2$ the Bohr magneton and B the absolute value of the magnetic field. Now the properties from eq. A.6–A.8 can be calculated, leading to the well established Schottky anomaly

$$C_\mathrm{Z} = Nk_\mathrm{B}\left(\frac{E}{k_\mathrm{B}T}\right)^2\frac{\mathrm{e}^{E/k_\mathrm{B}T}}{(\mathrm{e}^{E/k_\mathrm{B}T}+1)^2} \tag{A.10}$$

for the heat capacity that is depicted in fig. A.3 and shows a characteristic maximum if the thermal energy $k_\mathrm{B}T$ is about half the energy splitting $\Delta E = g_{\tilde{S}}\mu_\mathrm{B}B$.

Calculating the magnetization of the Au:Er alloy in a similar fashion results in

$$M = \frac{N}{V}\tilde{S}\tilde{g}\mu_\mathrm{B}\mathcal{B}_{\tilde{S}}(h) \tag{A.11}$$

with the Billouin function

$$\mathcal{B}_{\tilde{S}} = \frac{2\tilde{S}+1}{2\tilde{S}}\coth\left[\frac{(2\tilde{S}+1)h}{2\tilde{S}}\right] - \frac{1}{2\tilde{S}}\coth\left[\frac{h}{2\tilde{S}}\right] \tag{A.12}$$

and it's argument

$$h = \frac{\tilde{S}\tilde{g}\mu_\mathrm{B}B}{k_\mathrm{B}T} \ . \tag{A.13}$$

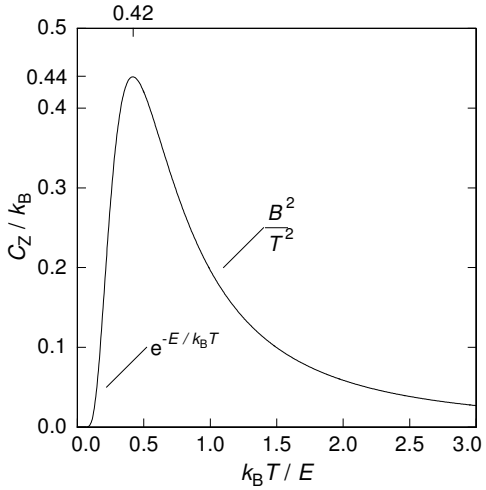

Figure A.3 Heat capacity C of a two-level system with an energy splitting of $\Delta E = \tilde{g}\mu_B B$ as a function of the reduced temperature ${}^{k_BT}/_{\Delta E}$. The approximations for $T \ll {}^{E}/_{k_B}$ and $T \gg {}^{E}/_{k_B}$ are also shown.

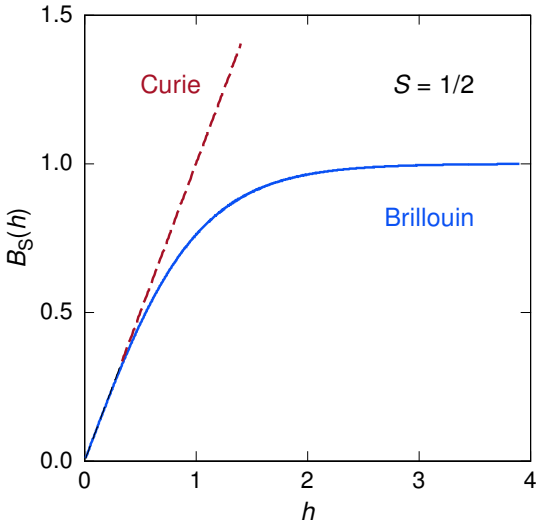

Figure A.4 Brillouin function $\mathcal{B}_{1/2}(h)$ with the Curie approximation for $h \ll 1$. It shows the qualitative progression of the magnetization in a $\tilde{S} = {}^{1}/_{2}$ system in the approximation of non-interacting magnetic moments.

Fig. A.4 depicts the Billouin function in the appropriate case of $\tilde{S} = {}^{1}/_{2}$ that shows the qualitative shape of the magnetization. The maximum value is defined by the density of magnetic ions ${}^{N}/_{V}$ and the maximum z component of the magnetic moment $\tilde{S}\tilde{g}\mu_B$. The field and temperature dependence enters through the argument of the Brillouin function in the ratio ${}^{B}/_{T}$. At low temperatures respectively high fields ($h \gg 1$) the magnetization saturates because all magnetic moments are aligned with the external field, while in the opposite case ($h \ll 1$) the magnetization enters a quasi linear regime known as Curie's law.

A.3 Thermodynamic characterization of interacting magnetic moments

While the assumption of non-interacting spins is sufficient for a qualitative description of the magnetic behavior of Au:Er, it is inadequate for a quantitative analysis. To calculate the magnetic response of Au:Er both the magnetic dipole-dipole interaction and the indirect exchange interacting between the spins must be taken into account.

A.3.1 Dipole-dipole interaction

The interaction of two paramagnetic ions at the positions $\boldsymbol{r}_i$ and $\boldsymbol{r}_j$ through their respective magnetic moment $\boldsymbol{\mu}_{i/j}$ enters the system's Hamiltonian through the following additional term:

$$H_{ij}^{\text{dipole}} = \frac{\mu_0}{4\pi}\frac{1}{r_{ij}^3}\left\{\boldsymbol{\mu}_i \cdot \boldsymbol{\mu}_j - 3(\boldsymbol{\mu}_i \cdot \hat{\boldsymbol{r}}_{ij})(\boldsymbol{\mu}_j \cdot \hat{\boldsymbol{r}}_{ij})\right\} \quad . \tag{A.14}$$

The quantity $\hat{\boldsymbol{r}}_{ij}$ represents the unit vector in the direction $\boldsymbol{r}_i - \boldsymbol{r}_j$ and r_{ij} the distance between the magnetic moments.

Because of the isotropy of the Γ_7 ground state doublet, the dipole-dipole interaction can be expressed in terms of the effective spins $\widetilde{\boldsymbol{S}}_i$ and $\widetilde{\boldsymbol{S}}_j$

$$H_{ij}^{\text{dipole}} = \Gamma_{\text{dipole}}\frac{1}{(2k_{\text{F}}r_{ij})^3}\left\{\widetilde{\boldsymbol{S}}_i \cdot \widetilde{\boldsymbol{S}}_j - 3\left(\widetilde{\boldsymbol{S}}_i \cdot \hat{\boldsymbol{r}}_{ij}\right)\left(\widetilde{\boldsymbol{S}}_j \cdot \hat{\boldsymbol{r}}_{ij}\right)\right\} \tag{A.15}$$

with prefactor $\Gamma_{\text{dipole}} = ({}^{\mu_0}/_{4\pi})\left(\tilde{g}\mu_{\text{B}}\right)^2(2k_{\text{F}})^3$ and $k_{\text{F}} = 1.2 \cdot 10^{10}\,\text{m}^{-1}$ being the Fermi wave vector of the gold conduction electrons.[1]

A.3.2 RKKY interaction

The exchange interaction of the localized $4f$ electrons of the erbium ions with the gold conduction electrons gives rise to an additional interaction between the erbium ions, the indirect exchange or Ruderman-Kittel-Kasuya-Yosida (RKKY) interaction. Expressed in terms of the effective spin, the RKKY interaction between two erbium

[1] The Fermi wave vector has been introduced artificially here to simplify the quantitative comparison with the indirect exchange interaction discussed later.

spins can be written as

$$H_{ij}^{\mathrm{RKKY}} = \Gamma_{\mathrm{RKKY}} \, (\widetilde{\boldsymbol{S}}_i \cdot \widetilde{\boldsymbol{S}}_j) \, F(2k_{\mathrm{F}} r_{ij}) \tag{A.16}$$

with the function $F(2k_{\mathrm{F}} r_{ij})$ being

$$F(2k_{\mathrm{F}} r_{ij}) = \frac{1}{(2k_{\mathrm{F}} r_{ij})^3} \left[\cos(2k_{\mathrm{F}} r_{ij}) - \frac{1}{2k_{\mathrm{F}} r_{ij}} \sin(2k_{\mathrm{F}} r_{ij}) \right] \tag{A.17}$$

and prefactor Γ_{RKKY} given by

$$\Gamma_{\mathrm{RKKY}} = \mathcal{J}^2 \, \frac{4 V_0^2 m_{\mathrm{e}}^* k_{\mathrm{F}}^4}{\hbar^2 (2\pi)^3} \, \frac{\widetilde{g}^2 (g_J - 1)^2}{g_J^2} \ . \tag{A.18}$$

Here $\mathcal{J}$ denotes the coupling energy between the localized spins and the conduction electrons, V_0 is the volume of the elementary cell and m_{e}^* is the effective mass of the conduction electrons. The expression for the RKKY interaction given above is derived under the assumption that the mean free path of the electrons is larger than the mean distance between the localized erbium ions. In principle, it is possible that the RKKY interaction is reduced due to a finite coherence length λ of the spin polarization of the conduction electrons. In this case an additional factor $\mathrm{e}^{-r/\lambda}$ would appear in (A.16). However, for Au:Er with suitable erbium concentrations for its main application in low temperature metallic magnetic calorimeters (MMCs), the mean free path of the conduction electrons is always much larger than the mean separation of the erbium ions.[2]

The fact that both the dipole-dipole interaction and the RKKY interaction are proportional to $1/r_{ij}^3$ allows us to compare their relative strength by a dimensionless parameter which is defined as the ratio of the two pre-factors

$$\alpha = \frac{\Gamma_{\mathrm{RKKY}}}{\Gamma_{\mathrm{dipole}}} \ . \tag{A.19}$$

Using this parameter α the coupling energy $\mathcal{J}$ can be expressed as[3]

$$\mathcal{J} \simeq \sqrt{\alpha} \, 0.145 \text{ eV} \ . \tag{A.20}$$

[2] In measurements of the residual resistivity of dilute $\mathrm{Au}_{1-x}\mathrm{Er}_x$ alloys $\varrho = x \, 6.7 \times 10^{-6} \, \Omega \, \mathrm{m}$ was found [Ara66, Edw68], and one can conclude that the mean free path of the conduction electrons is about 4000 Å for an erbium concentration of $x = 300$ ppm.

[3] The value of $\mathcal{J}$ given by (A.20) refers to the definition of the exchange energy between a localized spin $\boldsymbol{S}$ and a free electron $\boldsymbol{s}$ being $H = \mathcal{J} \boldsymbol{s} \cdot \boldsymbol{S}$. The definition $H = 2\mathcal{J} \boldsymbol{s} \cdot \boldsymbol{S}$ is often found in literature, leading to values of the parameter $\mathcal{J}$ being smaller by a factor of two.

A.4 Numerical calculation of the thermodynamical properties

A determination of the heat capacity and magnetization of a system of randomly distributed, interacting erbium spins requires a numerical calculation. There is a number of ways to perform this kind of calculation in the framework of a mean-field approximation. The method that requires the least amount of CPU time assumes the specific form of the mean field distribution that has been derived by Walker and Walstedt [Wal77, Wal80] for magnetic moments randomly distributed in a continuous medium. These authors showed that this analytic representation of the mean field distribution agrees well with numerically calculated mean field distributions.

An alternative approach is to write down the Hamiltonian for a cluster of interacting, randomly distributed spins on the Au lattice and obtain the eigenvalues of the cluster. This process is repeated for a large number of configurations of randomly positioned spins with the heat capacity and magnetization obtained by averaging. Since this process delivers the more accurate results and is currently used to determine the Au:Er behavior theoretically it will be explained in more detail in the following.

The basis for this approach is a cubic lattice segment of the gold fcc-lattice, typically with an edge length of ten to twenty lattice constants, depending on the simulated spin concentration. Additionally quasi-periodic boundary conditions are assumed, repeating the cube four times in every direction in space. On this lattice segment $n = \text{const.}$ spins are randomly distributed. For each configuration the Hamiltonian matrix is constructed. It includes the interaction of the magnetic moments with the external magnetic field (Zeeman interaction) and the dipole-dipole and RKKY interaction in between spin pairs.

In the basis $\mid S_1, S_2, \ldots, S_{n_{\max}}\rangle$ with the spin eigenvalues $S_i \in \{|\uparrow\rangle, |\downarrow\rangle\}$ and $\boldsymbol{B} = (0, 0, B_z)$ the Hamiltonian of two spins $\boldsymbol{S}_1$ und $\boldsymbol{S}_2$ at positions $\boldsymbol{r}_1$ und $\boldsymbol{r}_2$ takes the following form:

$$\mathcal{H} = \mathcal{H}^{\text{Zeeman}} + \mathcal{H}^{\text{dipole}} + \mathcal{H}^{\text{RKKY}}, \text{ with} \tag{A.21}$$

$$\mathcal{H}^{\text{Zeeman}} = -\tilde{g}\mu_{\text{B}}(S_{z\,1} + S_{z\,2})B_z \ , \tag{A.22}$$

$$\mathcal{H}^{\text{dipole}} = \frac{\mu_0}{4\pi}\frac{(\tilde{g}\mu_{\text{B}})^2}{r^3}\Big(\begin{array}{lll} -(3\,\cos^2\theta - 1) & (\ S_{z\,1}S_{z\,2} & \ ) \\ +1/4\,(3\cos^2\theta - 1) & (\ S_{+\,1}S_{-\,2} + S_{-\,1}S_{+\,2} & \ ) \\ -3/2\,\sin\theta\cos\theta & (\ S_{z\,1}S_{+\,2} + S_{z\,2}S_{+\,1} & \ ) \\ -3/2\,\sin\theta\cos\theta & (\ S_{z\,1}S_{-\,2} + S_{z\,2}S_{-\,1} & \ ) \\ -3/4\,\sin^2\theta & (\ S_{+\,1}S_{+\,2} & \ ) \\ -3/4\,\sin^2\theta & (\ S_{-\,1}S_{-\,2} & \ ) \end{array}\Big) \ , \tag{A.23}$$

$$\mathcal{H}^{\text{RKKY}} = \alpha\,\frac{\mu_0}{4\pi}(\tilde{g}\mu_{\text{B}})^2\,(2k_F)^3\Big(S_{z\,1}S_{z\,2} + \frac{1}{2}(S_{+\,1}S_{-\,2} + S_{-\,1}S_{+\,2})\Big)\,F(\rho) \tag{A.24}$$

and

$$F(\rho) = \rho^{-3}\left(\cos(\rho) - \frac{\sin(\rho)}{\rho}\right) \ , \ \rho = 2k_{\text{F}}r \ . \tag{A.25}$$

In this context θ is the angle between $\mathbf{B}$ and $\hat{\mathbf{r}} = \frac{\mathbf{r}_2 - \mathbf{r}_1}{|\mathbf{r}_2 - \mathbf{r}_1|}$. S_+ and S_- are the usual raising and lowering operators. The Hamiltonian matrix has the rank 2^n and therefore 2^{2n} elements. For reasons of clarity and comprehension the shown Hamiltonian is limited to two interacting magnetic moments:

$$\mathcal{H} = \begin{array}{c} \begin{array}{cccc} |\uparrow\uparrow\rangle & |\uparrow\downarrow\rangle & |\downarrow\uparrow\rangle & |\downarrow\downarrow\rangle \end{array} \\ \begin{pmatrix} -D_2 + \frac{1}{4}R + 2Z & -D_1 & -D_1 & -D_3 \\ -D_1 & +D_2 - \frac{1}{4}R & +D_2 + \frac{1}{2}R & +D_1 \\ -D_1 & +D_2 + \frac{1}{2}R & +D_2 - \frac{1}{4}R & +D_1 \\ -D_3 & +D_1 & +D_1 & -D_2 + \frac{1}{4}R - 2Z \end{pmatrix} \end{array}, \tag{A.26}$$

with the variables $\underbrace{Z = -\frac{1}{2}\tilde{g}\mu_{\text{B}}B_{\text{z}}}_{\text{Zeeman}}$, $\underbrace{R = \alpha\,\frac{\mu_0}{4\pi}(\tilde{g}\mu_{\text{B}})^2(2k_{\text{F}})^3\,\text{F}(\rho)}_{\text{RKKY}}$ and

$$\underbrace{D_1 = \frac{3}{4}\frac{\mu_0}{4\pi}\frac{\tilde{g}\mu_{\text{B}}}{r^3}\cos\theta\sin\theta \ , \ D_2 = \frac{1}{4}\frac{\mu_0}{4\pi}\frac{\tilde{g}\mu_{\text{B}}}{r^3}(3\cos^2\theta - 1) \ , \ D_3 = \frac{3}{4}\frac{\mu_0}{4\pi}\frac{\tilde{g}\mu_{\text{B}}}{r^3}\sin^2\theta}_{\text{dipole}-\text{dipole}} \ .$$

The parameters of the Monte-Carlo style simulation are chosen in the following way: $n = 6$ was chosen based on the minor improvement in accuracy for $n > 6$ and the available computation time. The lattice size was adjusted between 10 and 40

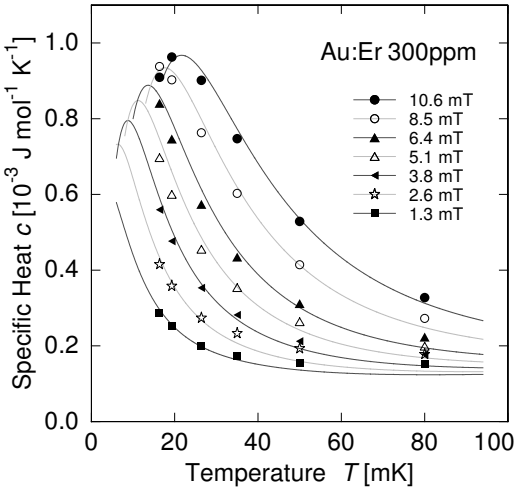

Figure A.5 Specific heat of Au:Er with 300 ppm enriched ^{166}Er as a function of temperature at different applied magnetic fields. The *solid lines* are calculated numerically with a interaction parameter $\alpha = 5$ [Ens00]

lattice constants to cover the usually used concentrations below 5000 ppm. These n spins are then randomly distributed across the lattice. Since the sensor material is normally available in a polycrystalline form also the orientation of the magnetic field is not previously defined and is chosen randomly and the angle θ is calculated accordingly for each pair of spins.

Based on this randomly chosen configuration the Hamiltonian matrix is constructed for different values of the external magnetic field and the energy eigenvalues are calculated by numerically diagonalizing the matrix. With the energy eigenvalues the thermodynamic properties C, M, and $^{\partial M}/_{\partial T}$ can be calculated at any given temperature according to eq. A.6–A.8.

These calculation is repeated a large number of times and the results then averaged to get the final predictions for the thermodynamic properties. For the extreme cases, namely temperatures below 20 mK and concentrations above 1000 ppm the number of repetitions needs to be at least 10^4 to get stable results.

As an example we show in Fig. A.5 the specific heat of an Au:Er sample having a concentration of 300 ppm of 97.8% enriched ^{166}Er. The temperature of the maximum in the specific heat depends on the magnitude of the external magnetic field as expected for a Schottky anomaly. However, the maximum is about twice as wide as for a non-interacting spin system. Calculations based on averaging over spin clusters provide a quantitative agreement assuming an interaction parameter α of 5. Although the calculated curves depend rather strongly on the choice of α, the value of $\alpha = 5$ should be viewed as an upper bound for the following two reasons. Firstly, the presence of ^{167}Er in the enriched sample leads to a slight additional broadening of the curve because of the hyperfine contribution of this isotope. Secondly, additional broadening results from a variation of the applied magnetic field, of about 10 to 15%, over the sample due to the geometry of the field coil.

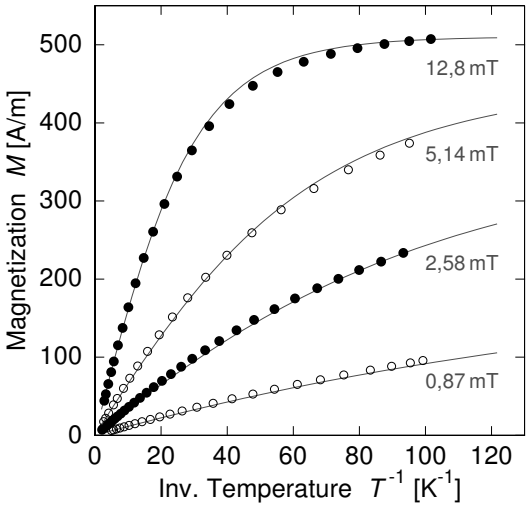

Figure A.6 Magnetization of Au:Er with 300 ppm enriched ^{166}Er as a function of $^1/_T$ at different applied magnetic fields. The *solid lines* are calculated numerically with a interaction parameter $\alpha = 5$ [Ens00]

The magnetization is plotted as a function of $^1/_T$ in Fig. A.6 at several different magnetic fields for the 300 ppm sample. As in the case of the specific heat, the magnetization deviates for the behavior of isolated spins. The deviation is primarily due to the interaction between the magnetic moments, but a small contribution is also present due to the two reasons discussed above for the heat capacity. Again the data can be described satisfactorily by assuming an interaction parameter of $\alpha = 5$.

The magnetic properties of a weakly interacting spin system is perhaps most easily characterized in terms of the temperature dependence of the susceptibility given by the Curie-Weiss law, $\chi = {}^{\lambda}/_{(T+\theta)}$. The Curie constant λ is proportional to the concentration of the spins, as is the Weiss constant θ, which is a measure of strength of the interactions. For the Au:Er system, $\lambda = x\,5.3\,\mathrm{K}$ and $\theta = \alpha\,x\,1.1\,\mathrm{K}$, where x is the concentration of erbium ions.

A.5 Response Time

Au:Er can be used as temperature sensor in several ways, one of which is the use in low temperature detectors as proposed by Bandler et al. [Ban93]. For this application not only the resolving power in temperature is important, but also the response time since it directly influences the count rate of the detector.

The rise time is influenced by two factors. Firstly the heat needs to get to the temperature sensor and secondly the heat needs to influence the spins and create the magnetic signal.

In a usual setup for soft X-ray detection the temperature sensor is connected to a particle absorber made of electroplated pure gold with dimensions of 250 µm ×

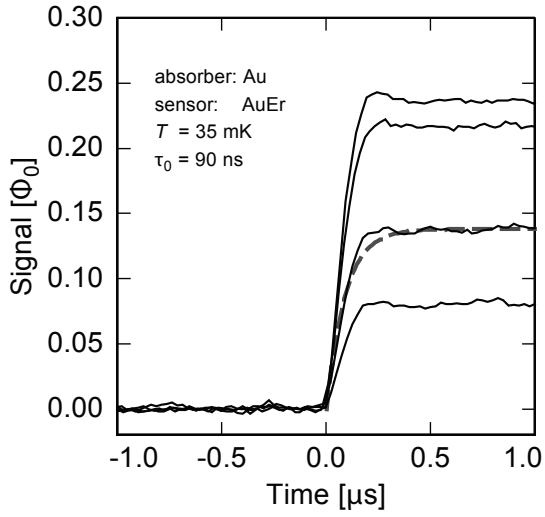

Figure A.7 Detector signals in units of magnetic flux in the SQUID during the first microsecond after the absorption of X-rays of different energy in an MMC designed for soft X-ray spectroscopy [Fle09]. The observed rise time of $\tau = 90\,\mathrm{ns}$ is in agreement predictions from the Korringa relation described in the text.

$250\,\mu\mathrm{m} \times 5\,\mu\mathrm{m}$ with a residual resistivity ratio of ${}^{R_{300\,\mathrm{K}}}/_{R_{4\,\mathrm{K}}} \approx 15$. In such an absorber the thermalization process is governed by the thermal diffusion within the absorber since the down conversion to thermal energies is completed on the order of $\sim 0.5\,\mathrm{ns}$ within a volume of a few cubic micrometers [Ens00, Koz12]. The time scale for the diffusion process is mainly determined by the geometry of the absorber and the presence of defects such as grain boundaries and dislocations. If we assume the before mentioned geometry, the thermalization time, using the Wiedemann–Franz law, can be estimated to be on the order of 10 ns.

The time for the heat to flow from the absorber into the sensor is more difficult to estimate since this depends very much on the nature of the thermal connection between the two components. For sputter deposited or electroplated gold absorbers, as used in micro-fabricated detectors, the thermal contact is sufficiently strong that no degradation of the response time of the magnetic calorimeters due to the presence of the interface is observable.

Finally, the energy is shared with the magnetic moments in the sensor material giving rise of the signal. The response time of the spins is determined by the electron-spin relaxation time τ, which is described by the Korringa relation $\tau = {}^{\kappa}/_{T}$, where κ denotes the Korringa constant. For Au:Er the Korringa constant has been determined in ESR measurements at 1 K to be $\kappa = 7 \times 10^{-9}\,\mathrm{Ks}$ [Sjø75]. This value of κ yields a spin-electron relaxation time of the order of 100 ns at the usual operation temperatures below 100 mK.

Therefore the electron-spin relaxation is the dominating factor in the response time of metallic magnetic calorimeters based on the sensor material Au:Er. This has successfully been shown in [Fle09] where rise times as low as $\tau = 90\,\mathrm{ns}$ have been observed and is shown in fig. A.7 reproduced from the same source.

While this balance between heat diffusion and electron-spin relaxation works out well for small detectors for soft X-ray spectroscopy this balance is off in case of larger detectors for hard X-ray or γ-ray spectroscopy. For detectors like maXs-200, described in [Pie12b, Pie12a], with absorber dimensions of $2000\,\mu m \times 500\,\mu m \times 200\,\mu m$ the heat diffusion within the absorber is the governing factor in the response time. Depending on the interaction site in the absorber the heat can reach the sensor with different time patterns and create different detector responses [Pie12a]. These different pulse shapes will complicate the analysis and degrade the detector resolution. Therefore it is helpful to weaken the link between absorber and Au:Er sensor to allow the absorber to thermalize internally before allowing the heat to flow to the sensor creating consistent pulse shapes independent of the interaction site within the absorber.

Influence of Nuclear Spins

In the design of a magnetic calorimeter the possible influence of nuclear spins has to be considered. In the case of Au:Er there are two ways in which nuclei can affect the performance of the calorimeter. Firstly, the isotope ^{167}Er with nuclear spin $I = {}^7/_2$ influences the magnetization and the heat capacity due to its hyperfine interaction with the $4f$ electrons. Secondly, and more subtle, the 100% abundant ^{198}Au nuclei with small magnetic moment but large quadrupole moment may contribute to the specific heat if the nuclei reside at positions where the electric field gradient is of non-cubic symmetry.

The hyperfine contribution of the erbium isotope ^{167}Er, if used in its natural abundance of 23 %, significantly reduces the magnetization signal and increases the specific heat of the sensor material. But since presently all metallic magnetic calorimeters use Au:Er that is depleted in ^{167}Er, it has no visible effect on the thermodynamic properties of the sensor material. The influence of ^{167}Er has nonetheless been investigated in [Sjø75] and its effect on metallic magnetic calorimeters has been summarized in e.g. [Fle05].

Nuclei of the host metal can also influence the performance of an MMC. The ^{198}Au nuclei have spin $I = {}^3/_2$, a quadrupole moment of 0.547 barn and a magnetic moment sufficiently small to be neglected. In pure gold no contribution of the nuclear spins to the specific heat is expected at low fields, since the electric field of cubic symmetry does not lift the degeneracy of the nuclear levels. However, for Au nuclei in the vicinity of an Er^{3+} ion the electric field gradient can be substantial and can split the nuclear levels. This results in an additional heat capacity. Fig. A.8 shows the measured heat capacity of the Au nuclei as a function of temperatures for samples with different erbium concentrations. The data below 10 mK for the sample with

600 ppm is the total specific heat since at such low temperatures the contribution of the Au nuclei is substantially larger than that of all other degrees of freedom. The figure also shows a theoretical curve calculated assuming a quadrupole splitting of 70 MHz for Au nuclei in the immediate vicinity of erbium ions, the splitting decreasing for nuclei at larger distances in a manner similar to that measured in other dilute alloys such as Cu:Pt [Kon96], Cu:Pd [Min80], and Gd:Au [Per76].

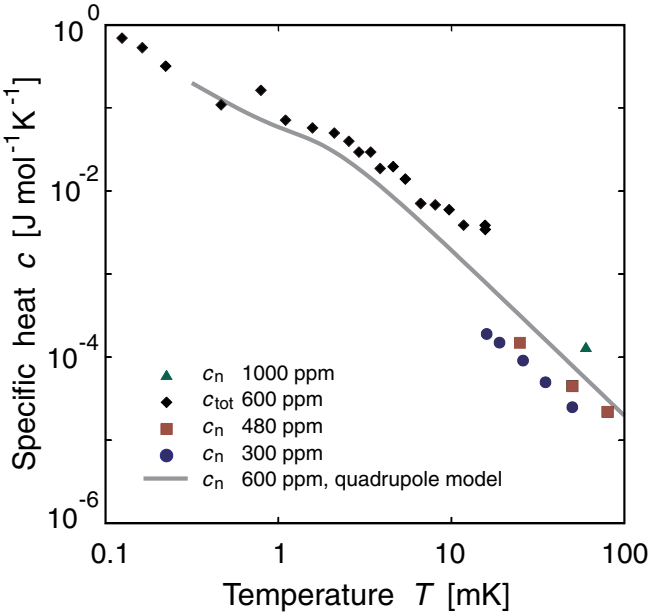

Figure A.8 Contribution of the Au nuclei to the specific heat of Au:Er samples with different concentrations. The *solid line* represents a theoretical curve assuming a quadrupole splitting of 70 MHz for Au nuclei, which are nearest neighbors of Er. Here c_{tot} denotes the total specific heat and c_{n} the contribution of just the Au nuclei to the specific heat. After [Ens00]

This unwanted contribution to the specific heat can only be eliminated by using a host material which has a nuclear spin $I \leq {}^1/_2$. At first glance it would appear desirable to use silver as a host material rather than gold since the two isotopes of silver (^{107}Ag and ^{109}Ag) both have nuclear spin $I = {}^1/_2$. However, the exchange energy $\mathcal{J}$ is 1.6 larger in silver than in gold as determined by ESR measurements[Tao71]. Since the interaction parameter α is quadratic in the exchange energy $\alpha \propto \mathcal{J}^2$, as shown in [Bur08] where $\alpha = 15$ was found, silver is not as attractive as a host material for a magnetic sensor. Just recently the interest in Ag:Er as sensor material has increased regardless, since MMCs have been used at even lower temperatures on the order of $T = 10$ mK where the additional specific heat in Au:Er might outweigh the stronger RKKY-interaction in Ag:Er.

A.5.1 Excess $^1/_f$-noise and AC-susceptibility

While investigating the noise behavior of metallic magnetic calorimeters with Au:Er as sensor material an excess noise contribution has been observed. The contribution was empirically found to be independent of temperature between 4.2 K and 20 mK and its noise power is proportional to the concentration of erbium ions in the sensor. It can be described by attributing a fluctuating magnetic moment with a spectral noise density of $S_m \simeq 0.1\,{}^{\mu_\mathrm{B}^2}/_{f^\eta}$ to each erbium ion, where μ_B is the Bohr magneton, f is the frequency and the exponent η takes values between 0.8 and 1 [Dan05, Fle09]. The same behavior was also found in detectors based on the sensor material Ag:Er [Bur08].

Similar behavior was found in several spin glasses (e.g. [Rei86, Sve89]) and agreed with the fluctuation-dissipation theorem [Joh28, Nyq28] by comparing ac-susceptibility measurements with equilibrium magnetic noise of the same sample. But the amplitude of the $^1/_f$-noise decreased quickly for $T > T_\mathrm{c}$, where T_c is the transition temperature to the spin glass state, until not distinguishable from the background noise.

Au:Er also undergoes a transition to a spin glass but up to two orders of magnitude below the temperatures metallic magnetic calorimeters are usually operated at (see sec. A.1). Therefore the $^1/_f$-noise should not be observable if explained by the same underlying cause. Recent investigations [Hof12, Wiß13] nonetheless found that the $^1/_f$-noise found in metallic magnetic calorimeters is in fact caused by the fluctuation-dissipation theorem, also by comparing the ac-susceptibility with equilibrium magnetic noise in a temperature range between 20 mK and 1 K for two $\mathrm{Au{:}Er}_{255\,\mathrm{ppm}}$ and $\mathrm{Au{:}Er}_{845\,\mathrm{ppm}}$ samples.

Bibliography

[Aar13] M. G. Aartsen, R. Abbasi, Y. Abdou *et al.* (IceCube Collaboration): *Measurement of Atmospheric Neutrino Oscillations with IceCube*, Phys. Rev. Lett. **111**, 081801 (2013), DOI: 10.1103/PhysRevLett.111.081801

[Aba11] K. Abazajian, E. Calabrese, A. Cooray *et al.*: *Cosmological and astrophysical neutrino mass measurements*, Astroparticle Physics **35**(4), 177 – 184 (2011), DOI: 10.1016/j.astropartphys.2011.07.002

[Abd09] J. N. Abdurashitov, V. N. Gavrin, V. V. Gorbachev *et al.* (SAGE Collaboration): *Measurement of the solar neutrino capture rate with gallium metal. III. Results for the 2002–2007 data-taking period*, Phys. Rev. C **80**, 015807 (2009), DOI: 10.1103/PhysRevC.80.015807

[Abe11] K. Abe, Y. Hayato, T. Iida *et al.* (Super-Kamiokande Collaboration): *Solar neutrino results in Super-Kamiokande-III*, Phys. Rev. D **83**, 052010 (2011), DOI: 10.1103/PhysRevD.83.052010

[Abe12] Y. Abe, C. Aberle, J. C. dos Anjos *et al.* (Double Chooz Collaboration): *Reactor $\overline{\nu}_e$ disappearance in the Double Chooz experiment*, Phys. Rev. D **86**, 052008 (2012), DOI: 10.1103/PhysRevD.86.052008

[Acq09] R. Acquafredda, T. Adam, N. Agafonova *et al.*: *The OPERA experiment in the CERN to Gran Sasso neutrino beam*, Journal of Instrumentation **4**(04), P04018 (2009), DOI: 10.1088/1748-0221/4/04/P04018

[Ada12a] T. Adam, N. Agafonova, A. Aleksandrov *et al.*: *Measurement of the neutrino velocity with the OPERA detector in the CNGS beam*, Journal of High Energy Physics **2012**(10), 1–37 (2012), DOI: 10.1007/JHEP10(2012)093

[Ada12b] P. Adamson, N. Ashby, R. Bumgarner *et al.*: *Measurement of the Velocity of the Neutrino with MINOS*, 44th Annual Precise Time and Time Interval (PTTI) Systems and Applications Meeting (2012), URL http://lss.fnal.gov/archive/preprint/fermilab-conf-12-666-ad.shtml

[Ade13] P. A. R. Ade, N. Aghanim, C. Armitage-Caplan *et al.* (Planck Collaboration): *Planck 2013 results. XVI. Cosmological parameters*, arXiv:1303.5076 [astro-ph.CO] (2013), http://arxiv.org/abs/1303.5076

[Ago13] M. Agostini, M. Allardt, E. Andreotti *et al.* (GERDA Collaboration): *Results on Neutrinoless Double-β Decay of ^{76}Ge from Phase I of the GERDA Experiment*, Phys. Rev. Lett. **111**, 122503 (2013), DOI: 10.1103/PhysRevLett.111.122503

[Aha13] B. Aharmim, S. N. Ahmed, A. E. Anthony *et al.* (SNO Collaboration): *Combined analysis of all three phases of solar neutrino data from the Sudbury Neutrino Observatory*, Phys. Rev. C **88**, 025501 (2013), DOI: 10.1103/PhysRevC.88.025501

[Ahm01] Q. R. Ahmad, R. C. Allen, T. C. Andersen *et al.* ((SNO Collaboration)): *Measurement of the Rate of $\nu_e + d \rightarrow p + p + e^-$ Interactions Produced by ^8B Solar Neutrinos at the Sudbury Neutrino Observatory*, Phys. Rev. Lett. **87**, 071301 (2001), DOI: 10.1103/PhysRevLett.87.071301

[Ahm02] Q. R. Ahmad, R. C. Allen, T. C. Andersen *et al.*: *Direct Evidence for Neutrino Flavor Transformation from Neutral-Current Interactions in the Sudbury Neutrino Observatory*, Phys. Rev. Lett. **89**, 011301 (2002), DOI: 10.1103/PhysRevLett.89.011301

[Alb14] J. Albert, D. Auty, P. Barbeau *et al.* (The EXO-200 Collaboration): *Search for Majorana neutrinos with the first two years of EXO-200 data*, Nature **advance online publication** (2014), DOI: 10.1038/nature13432

[Alt05] M. Altmann, M. Balata, P. Belli *et al.*: *Complete results for five years of GNO solar neutrino observations*, Physics Letters B **616**(3-4), 174–190 (2005), DOI: 10.1016/j.physletb.2005.04.068

[Alv49] L. W. Alvarez: *A Proposed Experimental Test of the Neutrino Theory*, University of California Radiation Laboratory Report **UCRL-328** (1949), DOI: 10.2172/929771

[And82] J. Andersen, G. Beyer, G. Charpak *et al.*: *A limit on the mass of the electron neutrino: The case of 163Ho*, Physics Letters B **113**(1), 72 – 76 (1982), DOI: 10.1016/0370-2693(82)90112-5

[And12] L. Anderson, E. Aubourg, S. Bailey *et al.*: *The clustering of galaxies in the SDSS-III Baryon Oscillation Spectroscopic Survey: baryon acoustic oscillations in the Data Release 9 spectroscopic galaxy sample*, Monthly Notices of the Royal Astronomical Society **427**(4), 3435–3467 (2012), DOI: 10.1111/j.1365-2966.2012.22066.x

[Ang05] J. Angrik, T. Armbrust, A. Beglarian *et al.*: *KATRIN Design Report 2004*, Tech. Rep. FZKA 7090; NPI ASCR Řež EXP-01/2005;

MS-KP-0501, Forschungszentrum Karlsruhe GmbH (2005), URL http://bibliothek.fzk.de/zb/berichte/FZKA7090.pdf

[Ang12] G. Angloher, M. Bauer, I. Bavykina *et al.*: *Results from 730 kgâĂĽdays of the CRESST-II Dark Matter search*, The European Physical Journal C **72**(4), 1–22 (2012), DOI: 10.1140/epjc/s10052-012-1971-8

[Ant04] P. Antonioli, R. T. Fienberg, F. Fleurot *et al.*: *SNEWS: the SuperNova Early Warning System*, New Journal of Physics **6**(1), 114 (2004), DOI: 10.1088/1367-2630/6/1/114

[Ara66] S. Arajs and G. Dunmyre: *A search for low-temperature anomalies in the electrical resistivity of dilute gold-erbium alloys*, Journal of the Less Common Metals **10**(3), 220 – 224 (1966), DOI: 10.1016/0022-5088(66)90113-5

[Ase11] V. N. Aseev, A. I. Belesev, A. I. Berlev *et al.*: *Upper limit on the electron antineutrino mass from the Troitsk experiment*, Phys. Rev. D **84**, 112003 (2011), DOI: 10.1103/PhysRevD.84.112003

[Aug12] M. Auger, D. J. Auty, P. S. Barbeau *et al.* (EXO Collaboration): *Search for Neutrinoless Double-Beta Decay in* ^{136}Xe *with EXO-200*, Phys. Rev. Lett. **109**, 032505 (2012), DOI: 10.1103/PhysRevLett.109.032505

[Bah04] J. N. Bahcall and M. H. Pinsonneault: *What Do We (Not) Know Theoretically about Solar Neutrino Fluxes?*, Phys. Rev. Lett. **92**, 121301 (2004), DOI: 10.1103/PhysRevLett.92.121301

[Bai83] P. A. Baisden, D. H. Sisson, S. Niemeyer *et al.*: *Measurement of the half-life of* ^{163}Ho, Phys. Rev. C **28**, 337–341 (1983), DOI: 10.1103/PhysRevC.28.337

[Bam77] W. Bambynek, H. Behrens, M. H. Chen *et al.*: *Orbital electron capture by the nucleus*, Rev. Mod. Phys. **49**, 77–221 (1977), DOI: 10.1103/RevModPhys.49.77

[Ban86] I. Band and M. Trzhaskovskaya: *Electron-wave-function expansion amplitudes near the origin calculated in the Dirac-Fock-Slater and Dirac-Fock potentials*, Atomic Data and Nuclear Data Tables **35**(1), 1 – 13 (1986), DOI: 10.1016/0092-640X(86)90027-6

[Ban93] S. Bandler, C. Enss, R. Lanou *et al.*: *Metallic magnetic bolometers for particle detection*, Journal of Low Temperature Physics **93**(3-4), 709–714 (1993), DOI: 10.1007/BF00693500

[Bar10] A. S. Barabash: *Precise half-life values for two-neutrino double-β decay*, Phys. Rev. C **81**, 035501 (2010), DOI: 10.1103/PhysRevC.81.035501

[Ben81] C. Bennett, A. Hallin, R. Naumann *et al.*: *The X-ray spectrum following ^{163}Ho M electron capture*, Physics Letters B **107**(1–2), 19 – 22 (1981), DOI: 10.1016/0370-2693(81)91137-0

[Ben03] C. L. Bennett, M. Bay, M. Halpern *et al.*: *The Microwave Anisotropy Probe Mission*, The Astrophysical Journal **583**(1), 1 (2003), DOI: 10.1086/345346

[Ber12] J. Beringer, J. F. Arguin, R. M. Barnett *et al.* (Particle Data Group): *Review of Particle Physics*, Phys. Rev. D **86**, 010001 (2012), DOI: 10.1103/PhysRevD.86.010001, including the 2013 partial update for the 2014 edition

[Beu11] F. Beutler, C. Blake, M. Colless *et al.*: *The 6dF Galaxy Survey: baryon acoustic oscillations and the local Hubble constant*, Monthly Notices of the Royal Astronomical Society **416**(4), 3017–3032 (2011), DOI: 10.1111/j.1365-2966.2011.19250.x

[Bla85] A. Blasi, G. Gallinaro, B. Osculati *et al.*: *Una nuova determinazione di limiti di massa per l'antineutrino, 1*, Tech. Rep. INFN/BE-85/2, INFN (1985)

[Bla06] K. Blaum: *High-accuracy mass spectrometry with stored ions*, Physics Reports **425**(1), 1 – 78 (2006), DOI: 10.1016/j.physrep.2005.10.011

[Bla11] C. Blake, E. A. Kazin, F. Beutler *et al.*: *The WiggleZ Dark Energy Survey: mapping the distance–redshift relation with baryon acoustic oscillations*, Monthly Notices of the Royal Astronomical Society **418**(3), 1707–1724 (2011), DOI: 10.1111/j.1365-2966.2011.19592.x

[Blo07] M. Block, D. Ackermann, K. Blaum *et al.*: *Towards direct mass measurements of nobelium at SHIPTRAP*, The European Physical Journal D **45**(1), 39–45 (2007), DOI: 10.1140/epjd/e2007-00189-2

[Bog92] N. W. Boggess, J. C. Mather, R. Weiss *et al.*: *The COBE mission - Its design and performance two years after launch*, Astrophysical Journal, Part 1 **397**(2), 420–429 (1992), DOI: 10.1086/171797

[Bur08] A. Burck: *Entwicklung großflächiger mikrostrukturierter magnetischer Kalorimeter mit Au:Er- und Ag:Er-Sensoren für den energieaufgelösten Nachweis von Röntgenquanten und hochenergetischen Teilchen*, Ph.D. thesis, Heidelberg University (2008), URN: urn:nbn:de:bsz:16-opus-88322

[Cam01] J. Campbell and T. Papp: *WIDTHS OF THE ATOMIC K–N7 LEVELS*, Atomic Data and Nuclear Data Tables **77**(1), 1 – 56 (2001), DOI: 10.1006/adnd.2000.0848

[Cap14] F. Capozzi, G. Fogli, E. Lisi *et al.*: *Status of three-neutrino oscillation parameters, circa 2013*, arXiv:1312.2878 [hep-ph] (2014), http://arxiv.org/abs/1312.2878

[Cha14] J. Chadwick: *Intensitätsverteilung im magnetischen Spektrum der β-Strahlen von Radium B+C.*, Verhandlungen der Deutschen Physikalischen Gesellschaft **16**, 383–391 (1914)

[Chu99] S. Chu, L. Ekström and R. Firestone: *WWW Table of Radioactive Isotopes* (1999), database version 1999-02-28, URL http://nucleardata.nuclear.lu.se/nucleardata/toi/

[Cla06] J. Clarke and A. I. Braginski, eds.: *The SQUID Handbook*, Wiley-VCH Verlag GmbH & Co. KGaA, Weinheim, Germany (2006)

[Cle98] B. T. Cleveland, T. Daily, J. Raymond Davis *et al.*: *Measurement of the Solar Electron Neutrino Flux with the Homestake Chlorine Detector*, The Astrophysical Journal **496**(1), 505 (1998), DOI: 10.1086/305343

[Coh72] R. L. Cohen, G. K. Wertheim, A. Rosencwaig and H. J. Guggenheim: *Multiplet Splitting of the 4s and 5s Electrons of the Rare Earths*, Phys. Rev. B **5**, 1037–1039 (1972), DOI: 10.1103/PhysRevB.5.1037

[Cos93] E. Cosulich, F. Gatti and S. Vitale: *Further results on μ-calorimeters with superconducting absorber-calorimeters with superconducting absorber*, Journal of Low Temperature Physics **93**(3-4), 263–268 (1993), DOI: 10.1007/BF00693430

[Cow56] C. L. Cowan, F. Reines, F. B. Harrison, H. W. Kruse and A. D. McGuire: *Detection of the Free Neutrino: a Confirmation*, Science **124**(3212), 103–104 (1956), DOI: 10.1126/science.124.3212.103

[Cro13] M. Croce, E. Bond, A. Hoover *et al.*: *Integration of Radioactive Material with Microcalorimeter Detectors*, Journal of Low Temperature Physics 1–6 (2013), DOI: 10.1007/s10909-013-1045-9

[Cur49] S. Curran, J. Angus and A. Cockroft: *III. Investigation of soft radiations—II. The beta spectrum of tritium*, Philosophical Magazine Series 7 **40**(300), 53–60 (1949), DOI: 10.1080/14786444908561210

[Dan05] T. Daniyarov: *Metallische magnetische Kalorimeter zum hochauflösenden Nachweis von Röntgenquanten und hochenergetischen Molekülen*, Ph.D. thesis, Heidelberg University (2005), URN: urn:nbn:de:bsz:16-opus-52319

[Dav73] D. Davidov, C. Rettori, A. Dixon *et al.*: *Crystalline-Field Effects in the Electron-Spin Resonance of Rare Earths in the Noble Metals*, Physical Review B **8**, 3563–3568 (1973), DOI: 10.1103/PhysRevB.8.3563

[Day03] P. K. Day, H. G. LeDuc, B. A. Mazin, A. Vayonakis and J. Zmuidzinas: *A broadband superconducting detector suitable for use in large arrays*, Nature **425**(6960), 817–821 (2003), DOI: 10.1038/nature02037

[Des03] R. D. Deslattes, E. G. Kessler, P. Indelicato *et al.*: *X-ray transition energies: new approach to a comprehensive evaluation*, Rev. Mod. Phys. **75**, 35–99 (2003), DOI: 10.1103/RevModPhys.75.35, URL http://physics.nist.gov/XrayTrans

[Dic65] R. H. Dicke, P. J. E. Peebles, P. G. Roll and D. T. Wilkinson: *Cosmic Black-Body Radiation*, Astrophysical Journal **142**, 414–419 (1965), DOI: 10.1086/148306

[DR81] A. De Rújula: *A new way to measure neutrino masses*, Nuclear Physics B **188**(3), 414 – 458 (1981), DOI: 10.1016/0550-3213(81)90002-X

[DR82] A. De Rújula and M. Lusignoli: *Calorimetric measurements of ^{163}Holmium decay as tools to determine the electron neutrino mass*, Physics Letters B **118**(4-6), 429–434 (1982), DOI: 10.1016/0370-2693(82)90218-0

[DR13] A. De Rújula: *Two old ways to measure the electron-neutrino mass*, arXiv:1305.4857 [hep-ph] (2013), http://arxiv.org/abs/1305.4857

[Dre13] G. Drexlin, V. Hannen, S. Mertens and C. Weinheimer: *Current Direct Neutrino Mass Experiments*, Advances in High Energy Physics **2013**(293986), 39 (2013), DOI: 10.1155/2013/293986

[Dru07] D. Drung, C. Assmann, J. Beyer *et al.*: *Highly Sensitive and Easy-to-Use SQUID Sensors*, Applied Superconductivity, IEEE Transactions on **17**(2), 699–704 (2007), DOI: 10.1109/TASC.2007.897403

[Dru11] D. Drung, J. Beyer, J.-H. Storm, M. Peters and T. Schurig: *Investigation of Low-Frequency Excess Flux Noise in DC SQUIDs at mK Temperatures*, Applied Superconductivity, IEEE Transactions on **21**(3), 340–344 (2011), DOI: 10.1109/TASC.2010.2084054

[Dvo11] R. Dvornický, K. Muto, F. Šimkovic and A. Faessler: *Absolute mass of neutrinos and the first unique forbidden β decay of ^{187}Re*, Phys. Rev. C **83**, 045502 (2011), DOI: 10.1103/PhysRevC.83.045502

[Edw68] L. R. Edwards and S. Legvold: *Electrical Resistivity of Some Dilute Gold-Rare-Earth Alloys*, Journal of Applied Physics **39**(7), 3250–3252 (1968), DOI: 10.1063/1.1656764

[Eli14] S. E. S. Eliseev, K. Blaum, M. Block *et al.*: *Penning-Trap Mass Spectrometry for Neutrino Physics*, Invited talk at the "Massive Neutrinos" conference in Bad Honnef, Germany (2014), URL https://www.uni-muenster.de/Physik.KP/AGWeinheimer/en/heraeus/index.html

[Eng13] J. W. Engle, E. R. Birnbaum, H. R. Trellue *et al.*: ^{163}Ho *for Micro-Calorimetric Electron Capture Spectroscopy to Measure the Mass of the Neutrino*, in *The Future of Neutrino Mass Measurements: Terrestrial, Astrophysical, and Cosmological Measurements in the Next Decade: Highlights of the νMass 2013 Workshop*, 54–57 (2013), http://arxiv.org/abs/1309.7810

[Ens00] C. Enss, A. Fleischmann, K. Horst *et al.*: *Metallic Magnetic Calorimeters for Particle Detection*, Journal of Low Temperature Physics **121**(3-4), 137–176 (2000), DOI: 10.1023/A:1004863823166

[Fer34] E. Fermi: *Versuch einer Theorie der β-Strahlen.*, Zeitschrift für Physik **88**(3-4), 161–177 (1934), DOI: 10.1007/BF01351864

[Fer12] E. Ferri, C. Arnaboldi, G. Ceruti *et al.*: *MARE-1 in Milan: Status and Perspectives*, Journal of Low Temperature Physics **167**(5-6), 1035–1040 (2012), DOI: 10.1007/s10909-011-0421-6

[Fer14] E. Ferri, D. Bagliani, M. Biassotti *et al.*: *Preliminary Results of the MARE Experiment*, Journal of Low Temperature Physics 1–6 (2014), DOI: 10.1007/s10909-013-1026-z

[Fie92] A. Fiege eds.: *Tritium*, Tech. rep., Kernforschungszentrum Karlsruhe (1992), URL http://bibliothek.fzk.de/zb/kfk-berichte/KFK5055.pdf

[Fle03a] A. Fleischmann: *Magnetische Mikrokalorimeter: Hochauflösende Röntgenspektroskopie mit energiedispersiven Detektoren*, Ph.D. thesis, Heidelberg University (2003), URN: urn:nbn:de:bsz:16-opus-128771

[Fle03b] A. Fleischmann: *Magnetische Mikrokalorimeter: Hochauflösende Röntgenspektroskopie mit energiedispersiven Detektoren*, Ph.D. thesis, Heidelberg University (2003), URN: urn:nbn:de:bsz:16-opus-128771

[Fle05] A. Fleischmann, C. Enss and G. M. Seidel: *Metallic Magnetic Calorimeters*, in C. Enss, ed., *Cryogenic particle detection*, no. 99 in Topics in Applied Physics, chap. 4, 151–216, Springer-Verlag Berlin, Heidelberg (2005)

[Fle09] A. Fleischmann, L. Gastaldo, S. Kempf *et al.*: *Metallic magnetic calorimeters*, AIP Conference Proceedings **1185**(1), 571–578 (2009), DOI: 10.1063/1.3292407

[For13] J. A. Formaggio (Project 8 Collaboration): *The Project 8 Neutrino Mass Experiment*, in *The Future of Neutrino Mass Measurements: Terrestrial, Astrophysical, and Cosmological Measurements in the Next Decade: Highlights of the νMass 2013 Workshop*, 32–34 (2013), http://arxiv.org/abs/1309.7810

[Fow13] J. Fowler, B. K. Alpert, W. B. Doriese and J. N. Ullom: *Microcalorimeter Pulse Analysis at Very High Count Rates* (2013), presentation at the 15th Workshop on Low Temperature Detectors, URL http://conference.ipac.caltech.edu/ltd-15/

[Fuk98] Y. Fukuda, T. Hayakawa, E. Ichihara *et al.* ((Super-Kamiokande Collaboration)): *Evidence for Oscillation of Atmospheric Neutrinos*, Phys. Rev. Lett. **81**, 1562–1567 (1998), DOI: 10.1103/PhysRevLett.81.1562

[Fur39] W. H. Furry: *On Transition Probabilities in Double Beta-Disintegration*, Phys. Rev. **56**, 1184–1193 (1939), DOI: 10.1103/PhysRev.56.1184

[FW00] D. Forkel-Wirth and G. Bollen eds.: *ISOLDE – a laboratory portrait*, Hyperfine Interactions **129**(1-4), 1–553 (2000), DOI: 10.1023/A:1012690327194

[Gal12] M. Galeazzi, F. Gatti, M. Lusignoli *et al.*: *The Electron Capture Decay of 163-Ho to Measure the Electron Neutrino Mass with sub-eV Accuracy (and Beyond)*, arXiv:1202.4763 [physics.ins-det] (2012), http://arxiv.org/abs/1202.4763

[Gan13] A. Gando, Y. Gando, H. Hanakago *et al.* (KamLAND-Zen Collaboration): *Limit on Neutrinoless ββ Decay of* ^{136}Xe *from the First Phase of KamLAND-Zen and Comparison with the Positive Claim in* ^{76}Ge, Phys. Rev. Lett. **110**, 062502 (2013), DOI: 10.1103/PhysRevLett.110.062502

[Gas14] L. Gastaldo, K. Blaum, A. Doerr *et al.*: *The Electron Capture ^{163}Ho Experiment ECHo*, Journal of Low Temperature Physics 1–9 (2014), DOI: 10.1007/s10909-014-1187-4

[Gat97] F. Gatti, P. Meunier, C. Salvo and S. Vitale: *Calorimetric measurement of the 163Ho spectrum by means of a cryogenic detector*, Physics Letters B **398**(3-4), 415 – 419 (1997), DOI: 10.1016/S0370-2693(97)00239-6

[Gat01] F. Gatti: *Microcalorimeter measurements*, Nuclear Physics B - Proceedings Supplements **91**(1–3), 293 – 296 (2001), DOI: 10.1016/S0920-5632(00)00954-3, Neutrino 2000

[GG12] M. Gonzalez-Garcia, M. Maltoni, J. Salvado and T. Schwetz: *Global fit to three neutrino mixing: critical look at present precision*, Journal of High Energy Physics **2012**(12), 1–24 (2012), DOI: 10.1007/JHEP12(2012)123, URL http://www.nu-fit.org

[Giu10] C. Giunti and M. Laveder: *Short-baseline electron neutrino disappearance, tritium beta decay, and neutrinoless double-beta decay*, Phys. Rev. D **82**, 053005 (2010), DOI: 10.1103/PhysRevD.82.053005

[Gom13] M. Gomes, F. Gatti, A. Nucciotti *et al.*: *Status of the MARE Experiment*, Applied Superconductivity, IEEE Transactions on **23**(3), 2101204–2101204 (2013), DOI: 10.1109/TASC.2013.2249180

[Hah92] W. Hahn, M. Loewenhaupt and B. Frick: *Crystal field excitations in dilute rare earth noble metal alloys*, Physica B: Condensed Matter **180–181, Part 1**, 176 – 178 (1992), DOI: 10.1016/0921-4526(92)90698-R

[Ham99] W. Hampel, J. Handt, G. Heusser *et al.*: *GALLEX solar neutrino observations: results for GALLEX IV*, Physics Letters B **447**(1-2), 127–133 (1999), DOI: 10.1016/S0370-2693(98)01579-2

[Ham08] J. Hamann, S. Hannestad, A. Melchiorri and Y. Y. Y. Wong: *Non-linear corrections to the cosmological matter power spectrum and scale-dependent galaxy bias: implications for parameter estimation*, Journal of Cosmology and Astroparticle Physics **2008**(07), 017 (2008), DOI: 10.1088/1475-7516/2008/07/017

[Ham10] J. Hamann, S. Hannestad, J. Lesgourgues, C. Rampf and Y. Y. Wong: *Cosmological parameters from large scale structure - geometric versus shape information*, Journal of Cosmology and Astroparticle Physics **2010**(07), 022 (2010), DOI: 10.1088/1475-7516/2010/07/022

[Har85] F. X. Hartmann and R. A. Naumann: *Observation of N and M orbital-electron capture in the decay of* ^{163}Ho, Phys. Rev. C **31**, 1594–1596 (1985), DOI: 10.1103/PhysRevC.31.1594

[Har90] H. Harari: *Neutrino Masses, Neutrino Oscillations and Dark Matter*, in G. Berthomieu and M. Cribier, eds., *Inside the Sun*, vol. 159 of *Astrophysics and Space Science Library*, 213–230, Springer Netherlands (1990), DOI: 10.1007/978-94-009-0541-2_20

[Har92] F. Hartmann and R. Naumann: *High temperature gas proportional detector techniques and application to the neutrino mass limit using* ^{163}*Ho*, Nuclear Instruments and Methods in Physics Research Section A: Accelerators, Spectrometers, Detectors and Associated Equipment **313**(1–2), 237 – 260 (1992), DOI: 10.1016/0168-9002(92)90102-A

[Hen12] D. Hengstler: *Untersuchung der Eigenschaften von supraleitenden Re-, Zn- und Zn:Mn-Absorbern für magnetische Mikrokalorimeter*, Diploma thesis, Heidelberg University (2012)

[Her00] T. Herrmannsdörfer, R. König and C. Enss: *Properties of Er-doped Au at ultralow temperatures*, Physica B: Condensed Matter **284–288, Part 2**, 1698 – 1699 (2000), DOI: 10.1016/S0921-4526(99)02942-7

[Hof12] V. Hoffmann: *Messung der AC-Suszeptibilität von paramagnetischem Au:Er bei Temperaturen oberhalb des Spinglas-Übergangs*, Bachelor thesis, Heidelberg University (2012)

[Höl97] G. Hölzer, M. Fritsch, M. Deutsch, J. Härtwig and E. Förster: $K\alpha_{1,2}$ *and* $K\beta_{1,3}$ *x-ray emission lines of the* 3*d transition metals*, Phys. Rev. A **56**, 4554–4568 (1997), DOI: 10.1103/PhysRevA.56.4554

[Hub04] J. Hubbell and S. Seltzer: *Tables of X-Ray Mass Attenuation Coefficients and Mass Energy-Absorption Coefficients (version 1.4)* (2004), National Institute of Standards and Technology, Gaithersburg, MD, URL http://physics.nist.gov/xaamdi

[Hub11] P. Huber: *Determination of antineutrino spectra from nuclear reactors*, Phys. Rev. C **84**, 024617 (2011), DOI: 10.1103/PhysRevC.84.024617

[Hub12] P. Huber: *On the determination of anti-neutrino spectra from nuclear reactors*, arXiv:1106.0687 [hep-ph] (2012), http://arxiv.org/abs/arXiv:1106.0687

[Irw05] K. D. Irwin and G. C. Hilton: *Transition-Edge Sensors*, in C. Enss, ed., *Cryogenic particle detection*, no. 99 in Topics in Applied Physics, chap. 3, 63–149, Springer Berlin Heidelberg (2005)

[Joh28] J. B. Johnson: *Thermal Agitation of Electricity in Conductors*, Physical Review **32**, 97–109 (1928), DOI: 10.1103/PhysRev.32.97

[Jos62] B. Josephson: *Possible new effects in superconductive tunnelling*, Physics Letters **1**(7), 251 – 253 (1962), DOI: 10.1016/0031-9163(62)91369-0

[Kaw88] O. Kawakami, A. Masuda, M. Fujioka, T. Omori and S. Yasumi: *Half-life of ^{163}Ho*, Phys. Rev. C **38**, 1857–1860 (1988), DOI: 10.1103/PhysRevC.38.1857

[Kem12] S. Kempf: *Entwicklung eines Mikrowellen-SQUID-Multiplexers auf der Grundlage nicht-hysteretischer rf-SQUIDs zur Auslesung metallischer magnetischer Kalorimeter*, Ph.D. thesis, Heidelberg University (2012), URN: urn:nbn:de:bsz:16-heidok-136201

[Kem13] S. Kempf, M. Wegner, L. Gastaldo, A. Fleischmann and C. Enss: *Multiplexed Readout of MMC Detector Arrays Using Non-hysteretic rf-SQUIDs*, Journal of Low Temperature Physics 1–7 (2013), DOI: 10.1007/s10909-013-1041-0

[Kem14] S. Kempf, L. Gastaldo, A. Fleischmann and C. Enss: *Microwave SQUID Multiplexer for the Readout of Metallic Magnetic Calorimeters*, Journal of Low Temperature Physics **175**(5-6), 850–860 (2014), DOI: 10.1007/s10909-014-1153-1

[Ket08] J. Ketelaer, J. Krämer, D. Beck *et al.*: *TRIGA-SPEC: A setup for mass spectrometry and laser spectroscopy at the research reactor {TRIGA} Mainz*, Nuclear Instruments and Methods in Physics Research Section A: Accelerators, Spectrometers, Detectors and Associated Equipment **594**(2), 162 – 177 (2008), DOI: 10.1016/j.nima.2008.06.023

[KK04] H. Klapdor-Kleingrothaus, I. Krivosheina, A. Dietz and O. Chkvorets: *Search for neutrinoless double beta decay with enriched ^{76}Ge in Gran Sasso 1990–2003*, Physics Letters B **586**(3-4), 198 – 212 (2004), DOI: 10.1016/j.physletb.2004.02.025

[KK06] H. V. KLAPDOR-KLEINGROTHAUS and I. V. KRIVOSHEINA: *THE EVIDENCE FOR THE OBSERVATION OF $0\nu\beta\beta$ DECAY: THE IDENTIFICATION OF $0\nu\beta\beta$ EVENTS FROM THE FULL SPECTRA*, Modern Physics Letters A **21**(20), 1547–1566 (2006), DOI: 10.1142/S0217732306020937

[Kon96] K. Konzelmann, G. Majer and A. Seeger: *Solid Effect Between Quadrupolar Transitions in Dilute Cu-Pd Alloys*, Zeitschrift für Naturforschung A **51**(5/6), 506–514 (1996)

[Koz12] A. Kozorezov: *Energy Down-Conversion and Thermalization in Metal Absorbers*, Journal of Low Temperature Physics **167**(3-4), 473–484 (2012), DOI: 10.1007/s10909-011-0426-1

[Kra05] C. Kraus, B. Bornschein, L. Bornschein *et al.*: *Final results from phase II of the Mainz neutrino mass search in tritium β decay*, The European Physical Journal C - Particles and Fields **40**(4), 447–468 (2005), DOI: 10.1140/epjc/s2005-02139-7

[Kra13] M. Krantz: *Entwicklung, Mikrofabrikation und Charakterisierung von metallischen magnetischen Kalorimetern für die hochauflösende Röntgenspektroskopie hochgeladener Ionen.*, Master's thesis, Heidelberg University (2013)

[Kru83] P. Kruit and F. H. Read: *Magnetic field paralleliser for 2π electron-spectrometer and electron-image magnifier*, Journal of Physics E: Scientific Instruments **16**(4), 313 (1983), DOI: 10.1088/0022-3735/16/4/016

[Lae84] E. Laegsgaard, J. U. Andersen, G. J. Beyer *et al.*: *The capture ratio N/M in the EC beta decay of ^{163}Ho*, in O. Klepper, ed., *Proceedings of the 7th International Conference on Atomic Masses and Fundamental Constants AMCO-7*, no. 26 in THD Schriftenreihe Wissenschaft und Technik, 652–658, Darmstadt-Seeheim (1984)

[Lah13] S. Lahiri, M. Maiti, Z. Szucs and S. Takacs: *Alternative production routes and new separation methods for no-carrier-added ^{163}Ho* (2013), presentation at the νMass 2013 conference, URL http://artico.mib.infn.it/numass2013/

[Lin07] M. Linck: *Entwicklung eines metallischen magnetischen Kalorimeters für die hochauflösende Röntgenspektroskopie*, Ph.D. thesis, Heidelberg University (2007), URN: urn:nbn:de:bsz:16-heidok-73562

[Lon87] M. J. Longo: *Tests of relativity from SN1987A*, Phys. Rev. D **36**, 3276–3277 (1987), DOI: 10.1103/PhysRevD.36.3276

[Lor02] T. J. Loredo and D. Q. Lamb: *Bayesian analysis of neutrinos observed from supernova SN 1987A*, Phys. Rev. D **65**, 063002 (2002), DOI: 10.1103/PhysRevD.65.063002

[Luk06] S. Lukić, F. Gevaert, A. Kelić *et al.*: *Systematic comparison of ISOLDE-SC yields with calculated in-target production rates*, Nuclear Instruments and Methods in Physics Research Section A: Accelerators, Spectrometers, Detectors and Associated Equipment **565**(2), 784 – 800 (2006), DOI: 10.1016/j.nima.2006.04.082

[Maj37] E. Majorana: *Teoria simmetrica dell'elettrone e del positrone*, Il Nuovo Cimento **14**(4), 171–184 (1937), DOI: 10.1007/BF02961314

[Mat08] J. A. B. Mates, G. C. Hilton, K. D. Irwin, L. R. Vale and K. W. Lehnert: *Demonstration of a multiplexer of dissipationless superconducting quantum interference devices*, Applied Physics Letters **92**(2), 023514 (2008), DOI: 10.1063/1.2803852

[Mat11] J. A. B. Mates: *The Microwave SQUID Multiplexer*, Ph.D. thesis, University of Colorado (2011), URL http://search.proquest.com/docview/868186018?accountid=11359

[Mat12] J. Mates, K. Irwin, L. Vale *et al.*: *Flux-Ramp Modulation for SQUID Multiplexing*, Journal of Low Temperature Physics **167**(5-6), 707–712 (2012), DOI: 10.1007/s10909-012-0518-6

[Maz06] B. A. Mazin, P. K. Day, K. D. Irwin, C. D. Reintsema and J. Zmuidzinas: *Digital readouts for large microwave low-temperature detector arrays*, Nuclear Instruments and Methods in Physics Research Section A: Accelerators, Spectrometers, Detectors and Associated Equipment **559**(2), 799 – 801 (2006), DOI: 10.1016/j.nima.2005.12.208, proceedings of the 11th International Workshop on Low Temperature Detectors LTD-11 11th International Workshop on Low Temperature Detectors

[McC84] D. McCammon, M. Juda, D. D. Reeder *et al.*: *A New Technique for Neutrino Mass Measurement*, in V. Barger and D. Cline, eds., *Neutrino Mass and Low Energy Weak Interactions*, 329–343, World Scientific (1984)

[McC05a] D. McCammon: *Semiconductor Thermistors*, in C. Enss, ed., *Cryogenic particle detection*, no. 99 in Topics in Applied Physics, chap. 2, 35–61, Springer Berlin Heidelberg (2005)

[McC05b] D. McCammon: *Thermal Equilibrium Calorimeters - An Introduction*, in C. Enss, ed., *Cryogenic particle detection*, no. 99 in Topics in Applied Physics, chap. 1, 1–34, Springer-Verlag Berlin, Heidelberg (2005)

[McH12] S. McHugh, B. A. Mazin, B. Serfass *et al.*: *A readout for large arrays of microwave kinetic inductance detectors*, Review of Scientific Instruments **83**(4), 044702 (2012), DOI: 10.1063/1.3700812

[Men11] G. Mention, M. Fechner, T. Lasserre *et al.*: *Reactor antineutrino anomaly*, Phys. Rev. D **83**, 073006 (2011), DOI: 10.1103/PhysRevD.83.073006

[Mik86] S. Mikheyev and A. Smirnov: *Resonant amplification of ν oscillations in matter and solar-neutrino spectroscopy*, Il Nuovo Cimento C **9**(1), 17–26 (1986), DOI: 10.1007/BF02508049

[Min80] M. Minier and C. Minier: *Screening charge density around several $\Delta Z = -1$ impurities in copper: Nickel, palladium, platinum, and vacancy*, Physical Review B **22**, 21–27 (1980), DOI: 10.1103/PhysRevB.22.21

[Mon09] B. Monreal and J. A. Formaggio: *Relativistic cyclotron radiation detection of tritium decay electrons as a new technique for measuring the neutrino mass*, Phys. Rev. D **80**, 051301 (2009), DOI: 10.1103/PhysRevD.80.051301

[Mou09] B. J. Mount, M. Redshaw and E. G. Myers: *Q Value of* $^{115}\mathrm{In} \rightarrow ^{115}\mathrm{Sn}(3/2^+)$*: The Lowest Known Energy β Decay*, Phys. Rev. Lett. **103**, 122502 (2009), DOI: 10.1103/PhysRevLett.103.122502

[Muk87] T. Mukoyama: *Exchange and Overlap Correction for Electron-Capture Decay of Ho*, Bull. Inst. Chem. Res. **65**(1), 17–22 (1987), URL http://hdl.handle.net/2433/77181

[Nor12] O. Noroozian, P. Day, B. H. Eom, H. LeDuc and J. Zmuidzinas: *Crosstalk Reduction for Superconducting Microwave Resonator Arrays*, Microwave Theory and Techniques, IEEE Transactions on **60**(5), 1235–1243 (2012), DOI: 10.1109/TMTT.2012.2187538

[Nuc08] A. Nucciotti: *The MARE Project*, Journal of Low Temperature Physics **151**(3-4), 597–602 (2008), DOI: 10.1007/s10909-008-9718-5

[Nuc10] A. Nucciotti, E. Ferri and O. Cremonesi: *Expectations for a new calorimetric neutrino mass experiment*, Astroparticle Physics **34**(2), 80 – 89 (2010), DOI: 10.1016/j.astropartphys.2010.05.004

[Nuc13] A. Nucciotti and F. Terranova, eds.: *The Future of Neutrino Mass Measurements: Terrestrial, Astrophysical, and Cosmological Measurements in the Next Decade; Highlights of the νMass 2013 Workshop* (2013), http://arxiv.org/abs/1309.7810

[Nuc14] A. Nucciotti: *Statistical sensitivity of ^{163}Ho electron capture neutrino mass experiments*, arXiv:1405.5060 [physics.ins-det] (2014), URL http://arxiv.org/abs/1405.5060

[Nyq28] H. Nyquist: *Thermal Agitation of Electric Charge in Conductors*, Physical Review **32**, 110–113 (1928), DOI: 10.1103/PhysRev.32.110

[Pab08] A. Pabinger: *Entwicklung eines vollständig mikrostrukturierten magnetischen Kalorimeters für die hochauflösende Röntgenspektroskopie*, Diploma thesis, Heidelberg University (2008)

[Pad12] N. Padmanabhan, X. Xu, D. J. Eisenstein *et al.*: *A 2 per cent distance to z = 0.35 by reconstructing baryon acoustic oscillations – I. Methods and application to the Sloan Digital Sky Survey*, Monthly Notices of the Royal Astronomical Society **427**(3), 2132–2145 (2012), DOI: 10.1111/j.1365-2966.2012.21888.x

[Pas13] S. Pascoli and T. Schwetz: *Prospects for Neutrino Oscillation Physics*, Advances in High Energy Physics **2013**, 29 (2013), DOI: 10.1155/2013/503401

[Pau77] W. Pauli: *Fünf Arbeiten zum Ausschließungsprinzip und zum Neutrino*, no. 27 in Texte zur Forschung, Wissenschaftliche Buchgesellschaft Darmstadt (1977), URL http://neutrino.uni-hamburg.de/...pauli.pdf

[Pen65] A. A. Penzias and R. W. Wilson: *A Measurement of Excess Antenna Temperature at 4080 Mc/s*, Astrophysical Journal **142**, 419–421 (1965), DOI: 10.1086/148307

[Per76] B. Perscheid, H. Büchsler and M. Forker: *Mössbauer study of the hyperfine interaction of ^{197}Au in gadolinium*, Physical Review B **14**, 4803–4807 (1976), DOI: 10.1103/PhysRevB.14.4803

[Per10] W. J. Percival, B. A. Reid, D. J. Eisenstein *et al.*: *Baryon acoustic oscillations in the Sloan Digital Sky Survey Data Release 7 galaxy sample*, Monthly Notices of the Royal Astronomical Society **401**(4), 2148–2168 (2010), DOI: 10.1111/j.1365-2966.2009.15812.x

[Pic92] A. Picard, H. Backe, H. Barth *et al.*: *A solenoid retarding spectrometer with high resolution and transmission for keV electrons*, Nuclear Instruments and Methods in Physics Research Section B: Beam Interactions with Materials and Atoms **63**(3), 345 – 358 (1992), DOI: 10.1016/0168-583X(92)95119-C

[Pie08] C. Pies: *Entwicklung eines Detektor-Arrays basierend auf magnetischen Kalorimetern für die hochaufgelöste Röntgenspektroskopie an hochgeladenen Ionen*, Diploma thesis, Heidelberg University (2008)

[Pie12a] C. Pies: *maXs-200: Entwicklung und Charakterisierung eines Röntgendetektors basierend auf magnetischen Kalorimetern für die hochauflösende Spektroskopie hochgeladener Ionen*, Ph.D. thesis, Heidelberg University (2012), URN: urn:nbn:de:bsz:16-heidok-141828

[Pie12b] C. Pies, S. Schäfer, S. Heuser *et al.*: *maXs: Microcalorimeter Arrays for High-Resolution X-Ray Spectroscopy at GSI/FAIR*, Journal of Low Temperature Physics **167**(3-4), 269–279 (2012), DOI: 10.1007/s10909-012-0557-z

[Pon46] B. Pontecorvo: *Inverse β Process*, Chalk River Laboratory Report **PD-205** (1946), URL http://pontecorvo.jinr.ru/work/ibp.html

[Pon57] B. Pontecorvo: *Mesonium and antimesonium*, Sov. Phys. JETP **6**, 429–431 (1957)

[Pon58] B. Pontecorvo: *Inverse beta processes and nonconservation of lepton charge*, Sov. Phys. JETP **7**, 172–173 (1958)

[Por11] J.-P. Porst: *High-Resolution Metallic Magnetic Calorimeters for β-Spectroscopy on ^{187}Rhenium and Position Resolved X-Ray Spectroscopy*, Ph.D. thesis, Heidelberg University (2011), URN: urn:nbn:de:bsz:16-opus-116035

[Raf10] G. G. Raffelt: *Physics opportunities with supernova neutrinos*, Progress in Particle and Nuclear Physics **64**(2), 393 – 399 (2010), DOI: 10.1016/j.ppnp.2009.12.057, neutrinos in Cosmology, in Astro, Particle and Nuclear Physics International Workshop on Nuclear Physics, 31st course

[Rai04] S. Rainville, J. K. Thompson and D. E. Pritchard: *An Ion Balance for Ultra-High-Precision Atomic Mass Measurements*, Science **303**(5656), 334–338 (2004), DOI: 10.1126/science.1092320

[Ran09] P. C.-O. Ranitzsch: *Low Temperature Calorimeters with Superconducting Particle Absorbers*, Diploma thesis, Heidelberg University (2009)

[Ran12] P.-O. Ranitzsch, J.-P. Porst, S. Kempf *et al.*: *Development of Metallic Magnetic Calorimeters for High Precision Measurements of Calorimetric ^{187}Re and ^{163}Ho Spectra*, Journal of Low Temperature Physics **167**(5-6), 1004–1014 (2012), DOI: 10.1007/s10909-012-0556-0

[Rei60] F. Reines, C. L. Cowan, F. B. Harrison, A. D. McGuire and H. W. Kruse: *Detection of the Free Antineutrino*, Phys. Rev. **117**, 159–173 (1960), DOI: 10.1103/PhysRev.117.159

[Rei86] W. Reim, R. H. Koch, A. P. Malozemoff, M. B. Ketchen and H. Maletta: *Magnetic Equilibrium Noise in Spin-Glasses: $Eu_{0.4}Sr_{0.6}S$*, Physical Review Letters **57**, 905–908 (1986), DOI: 10.1103/PhysRevLett.57.905

[Rep12] J. Repp, C. Böhm, J. Crespo López-Urrutia *et al.*: *PENTATRAP: a novel cryogenic multi-Penning-trap experiment for high-precision mass measurements on highly charged ions*, Applied Physics B **107**(4), 983–996 (2012), DOI: 10.1007/s00340-011-4823-6

[Rid65] P. Rider, K. Geschneider, Jr. and O. McMaster: *Gold-rich rare-earth-gold solid solutions*, Transactions of the Metallurgical Society of AIME **233**, 1488–1496 (1965)

[Rob88] R. G. H. Robertson and D. A. Knapp: *Direct Measurements of Neutrino Mass*, Annual Review of Nuclear and Particle Science **38**(1), 185–215 (1988), DOI: 10.1146/annurev.ns.38.120188.001153

[Sch00] J. Schönefeld: *Entwicklung eines mikrostrukturierten magnetischen Tieftemperatur-Kalorimeters zum hochauflösenden Nachweis von einzelnen Röntgenquanten*, Ph.D. thesis, Heidelberg University (2000)

[Sch12] S. Schäfer: *Entwicklung einer Detektorzeile aus metallischen magnetischen Kalorimetern zur hochauflösenden Röntgenspektroskopie an hochgeladenen Ionen*, Ph.D. thesis, Heidelberg University (2012), URN: urn:nbn:de:bsz:16-heidok-133487

[Sch13] B. Schwingenheuer: *Status and prospects of searches for neutrinoless double beta decay*, Annalen der Physik **525**(4), 269–280 (2013), DOI: 10.1002/andp.201200222

[Sis04] M. Sisti, C. Arnaboldi, C. Brofferio *et al.*: *New limits from the Milano neutrino mass experiment with thermal microcalorimeters*, Nuclear Instruments and Methods in Physics Research Section A: Accelerators, Spectrometers, Detectors and Associated Equipment **520**(1–3), 125 – 131 (2004), DOI: 10.1016/j.nima.2003.11.273, proceedings of the 10th International Workshop on Low Temperature Detectors

[Sjø75] M. E. Sjøstrand and G. Seidel: *Hyperfine resonance properties of Er^{3+} in Au*, Physical Review B **11**, 3292–3297 (1975), DOI: 10.1103/PhysRevB.11.3292

[Spr85] P. T. Springer, C. L. Bennett and P. A. Baisden: *Enhanced interaction energy shifts in the x-ray spectrum of ^{163}Ho*, Phys. Rev. A **31**, 1965–1967 (1985), DOI: 10.1103/PhysRevA.31.1965

[Spr87] P. T. Springer, C. L. Bennett and P. A. Baisden: *Measurement of the neutrino mass using the inner bremsstrahlung emitted in the electron-capture decay of ^{163}Ho*, Phys. Rev. A **35**, 679–689 (1987), DOI: 10.1103/PhysRevA.35.679

[Sve89] P. Svedlindh, K. Gunnarsson, P. Nordblad *et al.*: *Equilibrium magnetic fluctuations of a short-range Ising spin glass*, Physical Review B **40**, 7162–7166 (1989), DOI: 10.1103/PhysRevB.40.7162

[Tao71] L. J. Tao, D. Davidov, R. Orbach and E. P. Chock: *Hyperfine Splitting of Er and Yb Resonances in Au: A Separation between the Atomic and Covalent Contributions to the Exchange Integral*, Physical Review B **4**, 5–9 (1971), DOI: 10.1103/PhysRevB.4.5

[Tau10] Tauber, J. A., Mandolesi, N., Puget, J.-L. *et al.*: *Planck pre-launch status: The Planck mission*, Astronomy and Astrophysics **520**, A1 (2010), DOI: 10.1051/0004-6361/200912983

[TC11] S. Turck-Chièze and S. Couvidat: *Solar neutrinos, helioseismology and the solar internal dynamics*, Reports on Progress in Physics **74**(8), 086901 (2011), DOI: 10.1088/0034-4885/74/8/086901

[Tho09] A. Thompson *et al.*: *X-Ray Data Booklet* (2009), URL http://xdb.lbl.gov/

[Tul89] J. Tuli: *Nuclear data sheets for A = 144*, Nuclear Data Sheets **56**(4), 607 – 707 (1989), DOI: 10.1016/S0090-3752(89)80050-X

[Uso12] I. Usoltsev, R. Eichler, R. Dressler *et al.*: *Preparation of Pd-based intermetallic targets for high intensity irradiations*, Nuclear Instruments and Methods in Physics Research Section A: Accelerators, Spectrometers, Detectors and Associated Equipment **691**(0), 5 – 9 (2012), DOI: 10.1016/j.nima.2012.06.060

[vS09] F. von Seggern: *Development of a Metallic Magnetic Calorimeter towards a Neutrino Mass Measurement*, Master's thesis, Heidelberg University (2009)

[Wal77] L. R. Walker and R. E. Walstedt: *Computer Model of Metallic Spin-Glasses*, Physical Review Letters **38**, 514–518 (1977), DOI: 10.1103/PhysRevLett.38.514

[Wal80] L. R. Walker and R. E. Walstedt: *Computer model of metallic spin-glasses*, Physical Review B **22**, 3816–3842 (1980), DOI: 10.1103/PhysRevB.22.3816

[Wan12] M. Wang, G. Audi, A. Wapstra *et al.*: *The Ame2012 atomic mass evaluation*, Chinese Physics C **36**(12), 1603 (2012), DOI: 10.1088/1674-1137/36/12/003

[Weg13] M. Wegner: *Entwicklung eines 64-Pixel-Detektor-Arrays basierend auf mikrostrukturierten metallischen magnetischen Kalorimetern mit integriertem Mikrowellen-SQUID-Multiplexer*, Master's thesis, Heidelberg University (2013)

[Wel08] R. Weldle: *Untersuchung des Effekts magnetischer Verunreinigungen auf das Thermalisierungsverhalten von supraleitenden Teilchenabsorbern*, Diploma thesis, Heidelberg University (2008)

[Wen10] R. Wendell, C. Ishihara, K. Abe *et al.* (The Super-Kamiokande Collaboration): *Atmospheric neutrino oscillation analysis with subleading effects in Super-Kamiokande I, II, and III*, Phys. Rev. D **81**, 092004 (2010), DOI: 10.1103/PhysRevD.81.092004

[Whi96] J. Whitlock: *Canadian Nuclear FAQ* (1996), URL http://www.nuclearfaq.ca

[Wie09] J. S. E. Wieslander, J. Suhonen, T. Eronen *et al.*: *Smallest Known Q Value of Any Nuclear Decay: The Rare β^- Decay of ^{115}In$(9/2^+) \rightarrow^{115}$ Sn$(3/2^+)$*, Phys. Rev. Lett. **103**, 122501 (2009), DOI: 10.1103/PhysRevLett.103.122501

[Wil68] F. L. Wilson: *Fermi's Theory of Beta Decay*, American Journal of Physics **36**(12), 1150–1160 (1968), DOI: 10.1119/1.1974382

[Wil69] G. Williams and L. L. Hirst: *Crystal-Field Effects in Solid Solutions of Rare Earths in Noble Metals*, Physical Review **185**, 407–415 (1969), DOI: 10.1103/PhysRev.185.407

[Wiß13] V. Wissdorf: *Magnetisches 1/f-Rauschen und Imaginärteil der magnetischen Suszeptibilität von Erbium dotiertem Gold bei Millikelvin Temperaturen*, Bachelor thesis, Heidelberg University (2013)

[Wol78] L. Wolfenstein: *Neutrino oscillations in matter*, Phys. Rev. D **17**, 2369–2374 (1978), DOI: 10.1103/PhysRevD.17.2369

[Won11] Y. Y. Wong: *Neutrino Mass in Cosmology: Status and Prospects*, Annual Review of Nuclear and Particle Science **61**(1), 69–98 (2011), DOI: 10.1146/annurev-nucl-102010-130252

[Yas94] S. Yasumi, H. Maezawa, K. Shima *et al.*: *The mass of the electron neutrino from electron capture in 163Ho*, Physics Letters B **334**(1–2), 229 – 233 (1994), DOI: 10.1016/0370-2693(94)90616-5

Acknowledgment – Danksagung

„Ich erkläre hiermit, dass ich die vorgelegte Dissertation selbständig verfasst und dabei keine anderen als die angegebenen Quellen und Hilfsmittel verwendet habe.“ – So heißt es so schön in der häufig verwendeten Erklärung am Ende einer wissenschaftlichen Arbeit. Aber natürlich gibt es einige Leute, die nicht unwesentlich zum Gelingen dieser Arbeit beigetragen haben und denen hier noch einmal explizit gedankt werden soll.

Als erstes sei hier Professor Christian Enss genannt, der mir einen so problemlosen Wechsel von Hamburg nach Heidelberg und fast sechs Jahre Forschung auf verschiedenen Gebieten der Tieftemperaturdetektoren ermöglicht hat.

Auch Professor Heinz Horner sei für die Begutachtung meiner Arbeit und die entspannten Besprechungen im Vorfeld zu der Verteidigung gedankt, die mir einige Bedenken vor dieser genommen haben. Auch Hans-Christian Schultz-Coulon und Reiner Dahint sei für ihre Beteiligung an meiner Doktorprüfung gedankt.

Der größte Dank soll aber Loredana Gastaldo ausgesprochen werden. Ihrer Entschlossenheit und Überzeugung für das von mir verfolgte Projekt haben dieses erst ermöglicht und die Tatsache, dass sie immer schon einen Schritt weiter gedacht hat, hat entscheidend zum Erfolg dieser Arbeit beigetragen. Und nicht zuletzt möchte ich ihr für die gründliche Korrektur dieser Arbeit danken, was sicherlich nicht immer eine einfache Aufgabe war.

Als nächstes sei Andreas Fleischmann gedankt, der es schafft zu allen Fragestellungen weitere Denkanstöße zu liefern und durch seine langjährige Erfahrung und gute Intuition immer eine gute Antwort parat hat und in die richtige Richtung lenkt.

Sebastian Kempf möchte ich für seine langjährige Unterstützung und Kompetenz danken und dafür, dass ich „seinen“ Kryostaten für so lange Zeit belegen konnte. Auch ihm sei für die Korrektur von Teilen dieser Arbeit und den abschließenden Druck gedankt.

Mathias Wegner und Clemens Hassel sei für die amüsante Zeit im gemeinsamen Büro und auf Tagungen und die Unterstützung bei den zwei Hauptmessphasen

gedankt, ohne deren Hilfe diese niemals so hätten durchgeführt werden können. Während Clemens noch einen wunderbaren „Leidensgenossen“ bei der Fertigstellung dieser Arbeit dargestellt hat sei Mathias noch für die anteilige Korrektur dieser Arbeit gedankt.

Nun seien noch die „alten“ Bolos erwähnt, die mich von Anfang an begleitet haben und somit sicherlich einige blöde Fragen von mir beantworten mussten. Vielen Dank also Jan-Patrick Porst, Sönke Schäfer und Christian Pies. Vielen Dank auch den „neuen“ Bolos oder denen, die zumindest nach mir in der Arbeitsgruppe begonnen haben, und hier eine kurze oder längere Zeit gemeinsam mit mir verbracht haben. Dies sind (mit keinem Anspruch auf Vollständigkeit) Alexandra Kampkötter, Sarah Vick, Sebastian Heuser, Daniel Hengstler, Emil Pavlov, Nadine Foerster, Giulio Pizzigoni, Anna Ferring, Valentin Hoffmann, Simon Uhl, Christian Schötz, Jeshua Geist, Victoria Vißdorf, Matthäus Krantz, Steffen Allgeier, Michael Keller, Jan Bug, David Leibold, Sebastian Hähnle und Dennis Schulz. Einen besonderen Dank möchte ich noch Lisa Gamer aussprechen, ohne deren Hilfe beim Drucken und Abgeben dieser Arbeit es sicher mehr Komplikationen gegeben hätte.

Nicht so sehr an den eigentlichen Experimenten beteiligt, so konnte ich doch viel Freude und das ein oder andere Leid des Laboralltags mit den „Gläsern“ teilen. Sei es beim gemeinsamen Frühstück, den Kaffeepausen, bei Tagungen oder Feierlichkeiten habe ich die Zeit sehr genossen. Dies sind (wieder ohne Anspruch auf Vollständigkeit) Manfred von Schickfus, Gernot Kasper, Angela Halfar, Gudrun Ruyters, Daniel Rothfuß, Marius Hempel, Masoomeh Bazrafshan, Martin Schwarze, Paul Faßl, Annina Luck, Andreas Reifenberger, David Vogel, Alex Archer, David Uhrig, Andreas Schaller, Felix Ahrens, Benedikt Frey, Marcel Schrodin, Nils Hauff und Max Wolter.

Auch eher bei den „Gläsern“ heimisch möchte ich auch Andreas Reiser danken, der mit seinem hervorragenden technischen Verständnis immer ein guter Ansprechpartner war und in Zusammenarbeit mit Rudi Eitel immer für das nötige flüssige Helium gesorgt hat.

Für die Unterstützung im Sekretariat möchte ich mich herzlich bei Beatrice Schwöbel und Jessica Bender bedanken, die in den Fragen der Verwaltung und abseits der Physik mir immer kompetent und schnell zur Seite standen.

Nach den Heidelberger Kollegen möchte ich auch den internationalen Kollegen danken, nämlich den Mitglieder der ECHo Kollaboration, die sich wie ich von dem Thema der Neutrinomassenbestimmung am Elektroneneinfangprozess von ^{163}Ho haben begeistern lassen und so Bereiche untersuchen, deren Notwendigkeit mir am Anfang nicht einmal klar war.

Als weitere Kollegen oder vielleicht auch eher „Leidensgenossen“ seien noch meine Mit-(Post)Doktoranden aus Deutschland erwähnt, die ich auf unterschiedlichen

Tagungen immer wieder treffen und das Leid aber auch das Faszination der Neutrinophysik teilen konnte.

Auf der persönlichen Seite möchte ich als erstes meine Heidelberger WG hervorheben, die in unterschiedlicher Konstellation immer ein „zu Hause“ für mich dargestellt hat. Dabei sei Miriam Grüninger, Fenja Steermann, Steffen Guth, Nikolai Strähle, Anna-Maria Losardo, David Allendorf und Carina Meyer besonders gedankt.

Am Ende möchte ich noch meiner Familie danken, die mich so wunderbar in dieser Zeit begleitet hat. Angefangen bei meinem Vater Karl Heinz Ranitzsch, der immer ein Ansprechpartner für alle Themen ist, auch die Physik, und sich hier auch durch das Korrekturlesen dieser Arbeit hervorgetan hat. Nun ist er wohl nicht mehr der einzige „Dr. Ranitzsch“. Weiter geht es mit meiner Mutter Ok-Su Ranitzsch, die auch in schwierigen Zeiten es immer schafft mich an die anderen Dinge im Leben zu erinnern. Meinem Bruder Frederick Ranitzsch ist es wohl zu verdanken, dass es mich überhaupt nach Heidelberg verschlagen hat, der aber auch viele Leidenschaften mit mir teilt so dass jede Begegnung eine Freude ist. Meine Schwägerin Jessica Ranitzsch, die mich mit ihrer erfrischend pragmatischen Art, die sie mit meinem Bruder teilt, immer wieder überrascht und meine Blickweise mal wieder erweitert. Und als jüngste Vertreter der Familie Ranitzsch seien noch meine Nichten Frida und Carla erwähnt, die einfach Freude ausstrahlen und mich an andere Zeiten denken lassen.